MAGNETIC ACTIVITY
OF
PLANET-HOSTING STARS

Dissertation
zur Erlangung des Doktorgrades
des Departments Physik
der Universität Hamburg

vorgelegt von

Katja Poppenhäger

aus Kassel

Hamburg
2011

Gutachter der Dissertation:	Prof. Dr. J. H. M. M. Schmitt JProf. Dr. A. Reiners
Gutachter der Disputation:	Prof. Dr. P. H. Hauschildt Prof. Dr. D. Horns
Datum der Disputation:	06. Mai 2011
Vorsitzender des Prüfungsausschusses:	Dr. R. Baade
Vorsitzender des Promotionsausschusses:	Prof. Dr. J. Bartels
Dekan der MIN Fakultät:	Prof. Dr. H. Graener

Abstract

Magnetic activity in cool stars is a widely observed phenomenon, however it is still far from being understood. How fundamental stellar parameters like mass and rotational period quantitatively cause a stellar magnetic field which manifests itself in features such as spots, flares and high-energy coronal emission is a lively area of research in solar and stellar astrophysics. Especially for planet-hosting stars, stellar activity profiles are very interesting as exoplanets are affected by high-energy radiation, both at the time of planet formation as well as during the further lifetime of a star-planet system. In extreme cases, the atmosphere of a planet very close to its host star can be strongly heated by the stellar X-ray and EUV emission and finally escape the planet's gravitational attraction, so that the atmosphere of the planet evaporates over time.

Theoretically, planets can also affect their host star's magnetic activity. In analogy to processes in binary stars which lead to enhanced - both overall and periodically varying - activity levels, also giant planets might influence the stellar activity by tidal or magnetic interaction processes, however on a weaker level than in binaries. Some indications for such interactions exist from chromospheric measurements in stars with Hot Jupiters. In this thesis I investigate the magnetic activity of planet-hosting stars and especially possible effects from star-planet interactions with an emphasis on stellar coronae in X-rays.

I tested a complete sample of all known planet-hosting stars within 30 pc distance from the Sun for correlations of stellar X-ray properties with planetary parameters. A significant correlation exists between the stellar X-ray luminosity and the product of planetary mass and inverse semimajor axis. However, this could be traced back to a selection effect introduced by planetary detection methods. For stars in the solar neighborhood, planets are mainly detected by radial velocity shifts in the stellar spectra. This detection method introduces several trends in samples of planet-hosting stars which are investigated in detail in this thesis. On top of these selection effects, no significant other correlations which could be interpreted as manifestations of star-planet interactions were present in the sample.

I also monitored the chromospheric and coronal activity of a promising individual star-planet system over several months. This system consists of υ Andromedae, a cool main-sequence star, a Hot Jupiter and three more planets in wider orbits. Contrary to earlier findings by other authors, the star did not show planet-induced activity variations, but displayed variability with the stellar rotation period instead.

The star 51 Pegasi also hosts a Hot Jupiter; actually, it is the first exoplanet which was ever detected. In a detailed analysis of this star's coronal emission, I show that the star is in a Maunder minimum state, characterized by a very low coronal temperature of less than one million degrees and a persistent low activity level in coronal and chromospheric emission over sixteen years. The Hot Jupiter apparently does not enhance stellar activity in this system. I also present an analysis of the planet-hosting star τ Bootis, for which indications for a very short activity cycle of only one year duration have been published recently. The star rotates quickly compared to other stars of the same age, which might be due to a "spin-up" caused by its giant planet. My X-ray data that is available up to now suggests that a possible activity cycle is longer than thought so far; however, more data will be collected in 2011 and 2012 to allow a more detailed insight into this star's activity.

Zusammenfassung

Die magnetische Aktivität kühler Sterne ist ein wohlbekanntes, aber dennoch im Detail unverstandenes Phänomen. Wie genau fundamentale stellare Eigenschaften wie Masse und Rotationsperiode das stellare Magnetfeld beeinflussen, das sich z. B. durch Flecken, Eruptionen und hochenergetische Strahlung äußert, ist Gegenstand aktueller Forschung. Gerade bei planetentragenden Sternen ist die stellare Aktivität besonders interessant, da Planeten sowohl während ihrer Entstehung als auch während der weiteren Entwicklung des Stern-Planeten-Systems von der stellaren Röntgen- und EUV-Strahlug beeinflusst werden. Bei Planeten in extrem engen Umlaufbahnen kann die Planetenatmosphäre sogar so stark aufgeheizt werden, dass sie der Gravitation des Planeten entflieht und mit der Zeit verdampft.

Theoretisch können auch Planeten die Aktivität ihres Zentralsterns beeinflussen. Ähnlich wie bei Binärsternen, die starke Aktivität - sowohl insgesamt wie auch periodisch veränderlich - zeigen, könnten massive Planeten durch magnetische oder Gezeiten-Interaktion die stellare Aktivität steigern, allerdings in vergleichsweise geringerem Ausmaß. Einige Hinweise auf solche Interaktionen wurden in der chromosphärischen Emission von Sternen mit "Hot Jupiters" gefunden. In dieser Arbeit untersuche ich die magnetische Aktivität von planetentragenden Sternen und insbesondere mögliche Auswirkungen von Stern-Planeten-Interaktionen, mit Hauptaugenmerk auf die koronale Röntgenemission der Zentralsterne.

Dazu habe ich ein vollständiges Sample aller bekannten planetentragenden Sterne innerhalb von 30 pc Distanz von der Sonne auf Korrelationen zwischen den stellaren Röntgeneigenschaften und Planetenparametern untersucht. Dabei zeigte sich eine signifikante Korrelation der Röntgenleuchtkraft mit dem Produkt aus Planetenmasse und inverser großer Halbachse. Diese Korrelation konnte jedoch auf Auswahleffekte zurückgeführt werden, die von der Planetendetektion herrühren. Bei Sternen in der solaren Nachbarschaft werden Planeten hauptsächlich durch Radialgeschwindigkeitsschwankungen in den stellaren Spektren detektiert. Dieses Verfahren verursacht verschiedene Trends in den Samples von planetentragenden Sternen, die in dieser Arbeit im Detail untersucht werden. Zusätzlich zu diesen Auswahleffekten konnten keine anderen signifikanten Korrelationen nachgewiesen werden, die sich auf Stern-Planeten-Interaktionen hätten zurückführen lassen.

Zusätzlich habe ich die koronale und chromosphärische Aktivität eines besonders vielversprechenden einzelnen Stern-Planeten-Systems über mehrere Monate analysiert. Das entsprechende System besteht aus dem kühlen Hauptreihenstern υ Andromedae, einem Hot Jupiter sowie drei weiteren Planeten in größeren Umlaufbahnen. Im Gegensatz zu früheren Studien anderer Autoren zeigte der Stern keine planeteninduzierten Aktivitätsschwankungen, sondern Variabilität mit der stellaren Rotationsperiode.

Der Stern 51 Pegasi wird vom ersten jemals entdeckten Planeten, ebenfalls ein Hot Jupiter, umkreist. Durch eine umfassende Analyse der koronalen Emission dieses Sterns konnte ich nachweisen, dass der Stern sich in einem Maunder-Minimum-Zustand befindet, der sich durch eine sehr geringe koronale Temperatur von weniger als einer Million Grad und langfristig durch eine extrem niedrige chromosphärische und koronale Aktivität auszeichnet. Der Planet verstärkt die stellare Aktivität in diesem System offenbar nicht. Zusätzlich zeige ich die Ergebnisse einer Untersuchung des planetentragenden Sterns τ Bootis, für den von anderen Autoren Hinweise auf einen sehr kurzen Aktivitätszyklus von nur einem Jahr Dauer gefunden wurden. Dieser Stern rotiert schnell im Vergleich zu anderen Sternen gleichen Alters; es könnte in dem System ein "Spin-up" durch den massiven Planeten stattgefunden haben. Meine bisher aufgenommenen Daten weisen jedoch darauf hin, dass ein möglicher Aktivitätszyklus länger ist als bisher angenommen. Weitere Beobachtungen sind für 2011 und 2012 geplant, die genauere Einblicke in die Aktivität dieses Sterns liefern werden.

Contents

1 Introduction **1**
1.1 The birth of a star . . . 1
1.2 The main sequence . . . 2
1.3 The death of a star . . . 3

2 Stellar activity **5**
2.1 Historical records of solar activity . . . 5
2.2 The magnetic cycle . . . 6
2.3 Observing magnetic activity in stars . . . 8
2.3.1 Chromospheric activity . . . 8
2.3.2 Photospheric measurements . . . 9
2.3.3 Coronal activity . . . 9
2.3.4 X-ray instrumentation . . . 10
2.3.5 X-ray properties of cool stars . . . 11
2.4 Open questions . . . 12
2.4.1 Maunder minima . . . 13
2.4.2 Stellar activity cycles . . . 13

3 Exoplanets and their host stars **15**
3.1 Detection of exoplanets . . . 15
3.2 Interactions between stars and planets . . . 16
3.2.1 Tidal interaction . . . 17
3.2.2 Magnetic interaction . . . 17
3.2.3 Observing SPI signatures . . . 18
3.3 Open questions . . . 19
3.3.1 Evidence for chromospheric SPI . . . 19
3.3.2 Evidence for coronal SPI . . . 19
3.3.3 Selection effects in samples of planet-hosting stars . . . 19

4 51 Peg - a planet-bearing Maunder minimum candidate **21**

5 Coronal properties of planet-bearing stars **29**

6 A search for SPI in the upsilon Andromedae system **43**

7 Host star activity and planet mass **53**

8 A short activity cycle of τ Bootis? 61
8.1 Introduction . . . 61
8.2 Observations and data analysis . . . 62
8.3 Preliminary results . . . 63
8.3.1 X-ray lightcurves . . . 63
8.3.2 Activity levels . . . 63
8.3.3 Spectral properties . . . 64
8.4 Discussion of preliminary results . . . 67
8.5 Future observations . . . 67

9 Summary and future work 69
9.1 Summary of scientific results . . . 69
9.2 Future work . . . 70

10 Acknowledgment - Danksagung 73

11 Bibliography 75

Chapter 1

Introduction

Compared to the lifespan of a person, the beginning of modern astronomy starting with the invention of the telescope around 1600 seems long ago. Yet, it is just a blink of an eye in the history of the universe. Two million years ago, the first human beings evolved; 500 million years ago, the first animals on land came into existence. Four billion years ago, the first single-cell life forms on earth developed by mechanisms still unknown. Not much earlier, around 4.6 billion years ago, the Sun and its planets formed from a cloud of gas and dust. The zero-point of the cosmic timescale is 13.7 billion years ago, when the universe itself is thought to have come into existence from a space-time singularity known as the Big Bang.

In this grand perspective, my thesis focuses on the interplay of stars and their planets, so we will start by having a closer look at how stars and planets form, and then at how they develop over time.

1.1 The birth of a star

The space between stars is not empty, but filled with interstellar material consisting mostly of cool dust and gas. In such a cloud, the kinetic pressure of the particles from thermal motion and the gravitational attraction work against each other. If the mass of the cloud is high enough, gravity will overcome the kinetic pressure and the cloud will collapse. For a homogeneous cloud with density ρ and temperature T, this happens at the Jeans mass $M_J \propto \sqrt{\frac{T^3}{\rho}}$. The gravitational collapse can also be triggered by events that cause density fluctuations, such as clouds colliding or a nearby supernova explosion, so that the collapse may start at much lower masses than the Jeans mass.

A central core forms in the collapsing cloud; the released gravitational energy is radiated away, and finally, the core contraction stops when the core becomes optically thick to its infrared radiation. The outer layers of the cloud keep falling onto the star, producing most of the protostar's luminosity. However, a random cloud starting to collapse will most likely not be exactly spherically symmetric; together with some motion present before the start of the collapse, the cloud will have a net angular momentum.

For clouds with large angular momentum, no central core forms, but the material concentrates in a toroidal shape, leading to the formation of a multiple star system. In clouds with lower angular momentum which form central cores, the surrounding matter that keeps falling onto the central part of the object has to conserve angular momentum. It cannot fall directly towards the center, but forms a disk rotating around the core. The disk dissolves with time as the material in the disk forms planets, accretes onto the protostar or is blown out of the system by radiation pressure and stellar winds.

The formation of planets in the disk starts with the coagulation of dust particles. However, it is still a major unsolved question how exactly these planetary seeds can avoid fragmentation again at the so-called "meter barrier" to become larger planetesimals; this is the size range where coagulation becomes too weak to make larger grains stick together when they collide. After - by some not entirely clear process - larger planetesimals are formed,

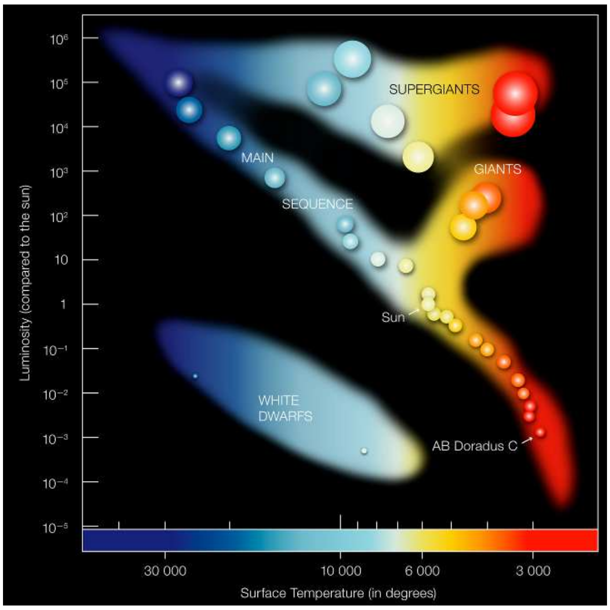

Figure 1.1: The Hertzsprung-Russel diagram, depicting the diagonal main sequence as well as the later stages in a stellar life, giants, supergiants and white dwarfs. (picture credit: ESO)

they grow further by gravitationally attracting smaller rocks in their vicinity. According to the core-accretion model, they will collect surrounding gas and become gas giants if their rocky cores are heavy enough. Planetary migration in the disk and ejection of larger objects by gravitational interactions will occur until a stable configuration is reached, such as we observe in our solar system nowadays.

In the solar system today, more than 99% of the angular momentum is contained within the orbital motions of Jupiter and Saturn, while the mass of the system is almost exclusively concentrated in the Sun. This is largely due to the spin-down of the Sun (see also section 2.3.5), but even when the Sun was rotating much faster, already a non-negligible part of the angular momentum was stored in the orbital motions of the massive planets.

1.2 The main sequence

When the circumstellar disk has dissolved, the star enters a stage called the main sequence. In this phase, the emission of the star is powered by nuclear fusion of hydrogen and not gravitational contraction any more. More massive stars are hotter and therefore have a bluish color in the optical, while the low-mass stars have lower surface temperature and therefore a redder spectrum. In the Hertzsprung-Russel diagram (HRD), where the absolute stellar luminosity is plotted as a function of color (or temperature, or mass), the main sequence forms a diagonal line from the upper left where the bright and hot stars are located to the lower right, where the Sun and stars of even lower mass reside (Fig. 1.1).

The nuclear process by which hydrogen is transformed to helium differs for low- and high-mass stars. Stars with masses below $1.5M_\odot$ burn hydrogen mainly through the proton-proton chain, a process which can start at temperatures of about four million Kelvin in the stellar core. For stars with higher masses the core temperatures are higher, so that the more efficient CNO cycle will take place in which carbon, nitrogen and oxygen act as "catalysts" for the hydrogen burning.

The type of the fusion mechanism also affects the inner structure of hot and cool stars. For both regimes, the core is the hottest part of the star and the photosphere (the visible outer layer) the coolest. Whenever steep temperature gradients are present, energy will be transferred by convection. If the temperature gradient is flatter, a rising bubble of hot plasma can exchange heat with the surroundings quick enough to cool down and not rise any further. In hot stars, the CNO cycle causes a steep temperature gradient in the stellar core, so that a convective zone forms that is surrounded by an outer radiative zone, where radiative transfer is sufficient to transport energy to the photosphere. In cool stars, however, the energy produced by the proton-proton chain can still be efficiently transported away by radiative transfer. Convection then only occurs in the outer layers of the star. In very low-mass stars, no inner radiative core is present at all, so that these stars with masses below $0.3M_\odot$ are fully convective.

The two regimes of stars with inner convective zones as opposed to stars with outer convection zones are also called hot and cool stars or early-type and late-type stars. The latter naming convention is actually a historical misunderstanding: in the nineteenth century, stars were thought to start as hot and therefore "early" stars and then to evolve into cooler "late" stars (Helmholtz 1856; Thomson 'Lord Kelvin' 1862).

Hot and cool stars also differ in their ability to produce magnetic fields. The Sun as a cool star displays many features like sunspots and an activity cycle which are connected to a special process of magnetic field generation which transfers kinetic into magnetic energy, the so-called magnetic dynamo. Although this mechanism is not entirely understood, it seems that a solar-like dynamo requires an outer convection zone and differential rotation (see section 2.2). Related dynamo mechanisms may be at work in fully convective stars. Hot stars with an outer radiative zone cannot support this kind of a dynamo process. However, strong magnetic fields have been detected for a special group of A and B stars which are strongly enriched in certain elements; these Ap/Bp stars can display "abundance patches" on their surface. How these stars obtain their magnetic field is under debate; conserved fossil fields which stem from the interstellar medium are a possibility, but also some dynamo processes in the convective core are discussed.

As high-mass stars are brighter, they use up their hydrogen "fuel" faster than low-mass stars. The Sun, for example, will spend 10 Gyr on the main sequence, while O type stars, which are brighter than the Sun by a factor of > 30000, will leave the main sequence after only 10 Myr of hydrogen burning. This fact can be used to estimate the age of stellar clusters, as in old clusters, the upper part of the main sequence will be depopulated already (Fig. 1.2).

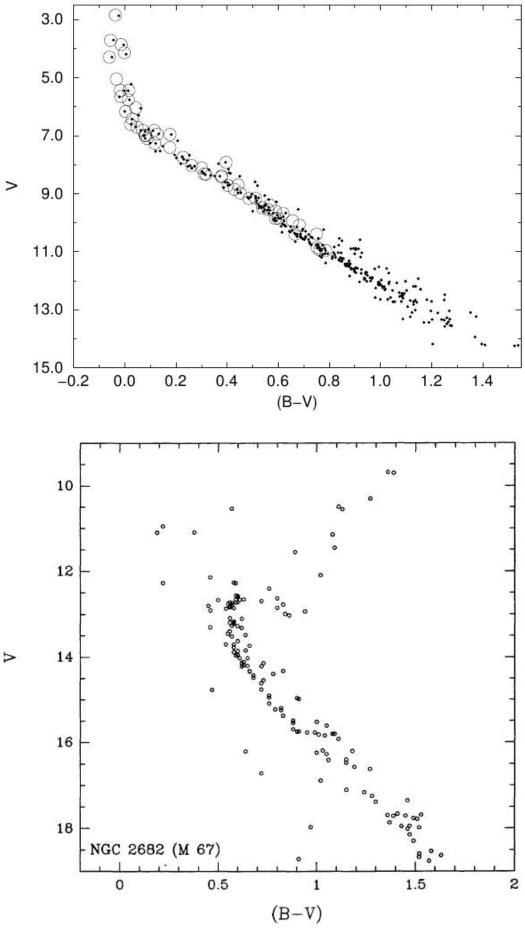

Figure 1.2: Hertzsprung-Russel diagram for the Pleiades, a young cluster (top), and M 67, an old cluster (bottom). The massive stars in M 67 have evolved away from the main sequence (Hansen-Ruiz & van Leeuwen 1997; Carraro et al. 1994).

1.3 The death of a star

As stars age and use up their hydrogen, they will start burning heavier elements, starting with helium. As a consequence, the color-luminosity relation changes and the stars evolve away from the main sequence. The final stage of a star again depends on its initial mass: stars with less than $0.5 M_\odot$ will not be able to start nuclear burning of helium, and just slowly go dim and collapse.

Stars of a medium mass range between 0.5 and 2.5 solar masses will first shrink as the hydrogen runs low until the core temprature becomes high enough to start burning helium. In this initial "helium flash", the star moves up in the HRD to the giant branch, as it now produces an inflated outer layer around its core. After a phase of stable helium burning in the core and hydrogen burning in a shell surrounding it, oxygen and carbon will accumulate in the core as the products of helium burning. These elements will never ignite in such stars as the temperature does not become high enough, instead the hydrogen- and helium burning shells expand outwards; this stage is called the asymptotic giant branch. The helium-shell burning does not happen in a smooth process, but rather in "fits and starts", causing the star to undergo pulsations. In one final pulse, the star will eject its outer layers as a planetary nebula, while the inner part collapses until the electron degeneracy pressure, a consequence of the Pauli exclusion principle, halts the shrinkage. This final state is called a white dwarf, a hot and dense object which cools slowly and makes its way to the lower left area of the HRD.

Stars with larger mass evolve differently, because the inner core consisting of oxygen and carbon which could not be ignited in lower-mass stars will here undergo nuclear fusion and form heavier elements, producing neon, silicon and finally iron. This way, an onion-like inner structure of burning shells will develop, with the heaviest elements at the center. However, the fusion of iron does not produce energy any more, it consumes it instead. This is critical for the star: when the silicon which forms the iron is depleted, there is not enough energy produced any more to support the star against its own gravity, and the star will rapidly collapse onto itself, expelling parts of its matter in an explosion. This process, which can be observed in form of a supernova, is so violent that protons and electrons in the collapsing core form neutrons, and only the neutron degeneracy pressure stops the contraction. The central remainder of such a supernova is a neutron star, or, if the mass of the collapsing core is even larger, a black hole. The plasma ejected in a supernova enriches the interstellar medium with heavy elements and in turn feeds the formation of new stars again.

Chapter 2

Stellar activity

What is stellar activity? Basically all phenomena that do not fit into the picture of a star as a ”quietly” burning ball of plasma. Naively, one would expect a star to have a hot core where the nuclear reactions take place, and outer layers which become subsequently cooler. However, observations of the Sun show that above its optical "surface", the photosphere with a typical temperature of $\sim$ 6000 K, further layers exist. The chromosphere, named for its reddish color visible in solar eclipses, extends to a height of ca. 2000 km above the photosphere and reaches temperatures up to 20000 K. At larger heights, the transition region and finally the corona follow, where temperatures of several million K are present. In the solar atmosphere, violent energetic processes take place (see Fig. 2.1). Phenemenologically, one observes features such as sun spots, plagues, prominences and coronal mass ejections.

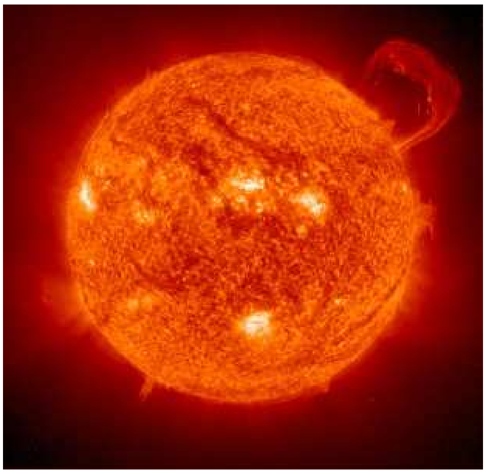

Figure 2.1: View of the Sun in the extreme ultraviolet, showing hot spots and a large prominence (picture credit: *SOHO*, ESA/NASA).

This kind of activity is specific for cool stars which have an outer convection zone and are therefore able to host some sort of magnetic dynamo. Magnetic fields in hot Ap/Bp stars differ fundamentally from this as they are mostly constant large-scale fields. In contrast, it is exactly the spatial fine structure and variability that produces the variety of atmospheric phenomena we observe in solar-like stars which are at the focus of my thesis.

In a historical perspective, today’s understanding of the relevance of stellar magnetic fields and the ubiquity of magnetic phenomena in late-type stars was preluded by a long series of insights starting more than two thousand years ago.

2.1 Historical records of solar activity

The first written record of observed sunspots dates back into the fourth century BC, by the chinese astronomer Gan De; other early sunspot detections of which we have records today were performed not only in China, but also by Arabic and European observers (see Temple (1988)). The advent of the telescope in the sixteenth century made more detailed studies possible, foremost of all the discovery of Jupiter’s moons by Galilei in 1610, heralding the end of the geocentric view of the universe. Solar activity as observed in sunspot numbers was recognized as a cyclic phenomenon 150 years ago (Schwabe 1844; Wolf 1856). A few years later Spörer (1865) found that not only the num-

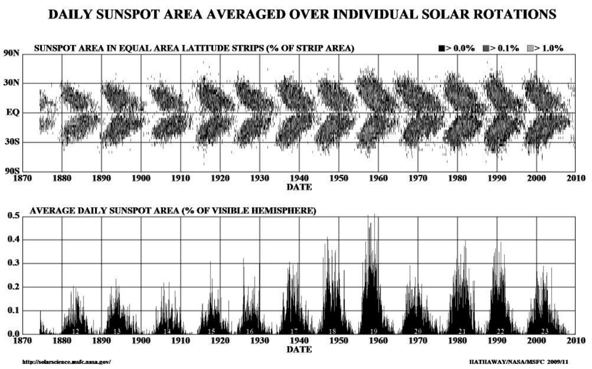

Figure 2.2: Butterfly diagram, first introduced by Maunder, showing the number (lower panel) and latitude (upper panel) of sunspots during several solar activity cycles (picture credit: NASA).

ber, but also the latitude of sunspots follows an eleven-year cycle. The mean latitude at which solar sunspots appear decreases from the start of an activity cycle to its end, which is depicted in the famous butterfly diagram (see Fig. 2.2).

In 1908, the magnetic field of sunspots was discovered by Hale, who observed Zeeman splitting of photospheric spectral lines in sunspot spectra (Hale 1908). This led to the formulation of the polarity rule, which describes the reversal of the solar magnetic field polarity from one activity cycle to the next. This is observed in the (switching) magnetic polarities of sunspot pairs on the northern and southern solar hemisphere. Later on, also the *global* magnetic field of the Sun was recognized to undergo polarity reversals (Babcock 1959). Thus the insight emerged that the true cycle of the Sun is a 22-year magnetic cycle, of which the 11-year activity cycle is just an easily observable manifestation.

2.2 The magnetic cycle

How does the Sun produce a magnetic field with switching polarity? We know from photospheric magnetograms that during sunspot minimum the magnetic field is in a mainly poloidal (nearly axisymmetric) configuration, which becomes mainly toroidal during sunspot

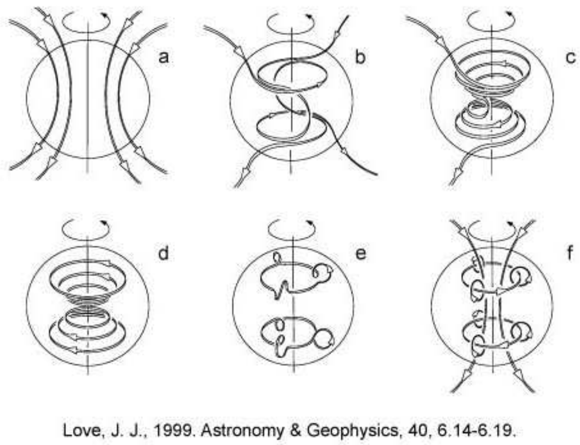

Figure 2.3: A schematical view of the $\alpha\Omega$ dynamo (Love 1999), depicting the Ω effect in pictures a-c and the α effect in pictures d-f.

maximum, and then turns into a poloidal configuration again, but with opposite polarity. So, a successful model needs to include two mechanisms: how a poloidal field can be transformed into a toroidal one, and a toroidal field into a poloidal.

It turns out that the first part of the problem can be solved in quite a forward way. The Sun displays differential rotation with regard to latitude on the surface as well as to radial distance from its center. For the differential rotation at the surface, rotational periods of $\approx$ 25.3 d at the equator and $\approx$ 31.3 d at a latitude of 60° have been measured (see for example Snodgrass (1984); Pierce & Lopresto (1984); Komm et al. (1993)). Assuming that a poloidal field is present, the differential rotation will cause the magnetic field lines to wind up around the rotational axis (see Fig. 2.3 a-c). Overall, the wound-up field lines then yield a large-scale toroidal field; this is called the Ω effect.

The second part, transferring this toroidal field back into a poloidal configuration, is more difficult. The classical model by Parker (1955) explains this by plasma "blobs" rising in the solar convection zone. They expand as they reach layers of lower density and start to rotate due to the Coriolis force. The magnetic field lines contained within them become twisted as they rise to the surface, so that small magnetic loops perpendicular to the previous configuration are produced, which will yield a poloidal field configuration on a global scale again (see Fig. 2.3 d-f). This is called the α effect, giving the name $\alpha\Omega$ dynamo to this model. There are several modifications of this idea; the Babcock-Leighton model (Babcock 1961; Leighton 1969) forms the poloidal field by transforming a small percentage of the magnetic field of large sunspot pairs into a net dipole moment. Other models include the Sun's meridional flow which transports plasma slowly from the equator to the poles at the surface and back to the equator at deeper layers. In modern models (Durney 1995; Dikpati & Gilman 2001; Browning et al. 2006), the toroidal flux system is not located in the convection zone itself, but at the tachocline (the layer between the approximately uniformly rotating radiative core and the differentially rotating convection zone).

Another type of dynamo mechanisms which can also be applied to fully convective stars are turbulent dynamos. In these kinds of models, the relevant quantities such as the magnetic and electric field, the velocity and the current density are split into a mean field component and a fluctuating component which is zero on average (Krause & Raedler 1980). In doing this, one removes the dependency on small-scale structures in the magnetic field and is able to calculate properties of the large-scale field. This formalism yields a detailed derivation of the α effect, which is driven by turbulent motions in the stellar plasma; the α effect had been derived before by Parker (1955), but that explanation was restricted to heuristic arguments. The mean field model allows dynamos which do not necessarily rely on a combination of the α and Ω effect, but can also transform toroidal and poloidal fields into each other purely by α effects. Such mechanisms are called α^2 dynamos.

However, there is no quantitative closed model yet which reliably describes the solar cycle with respect to the main observable effects such as sunspot appearance, the butterfly diagram, cycle duration and strength of individual upcoming cycles.

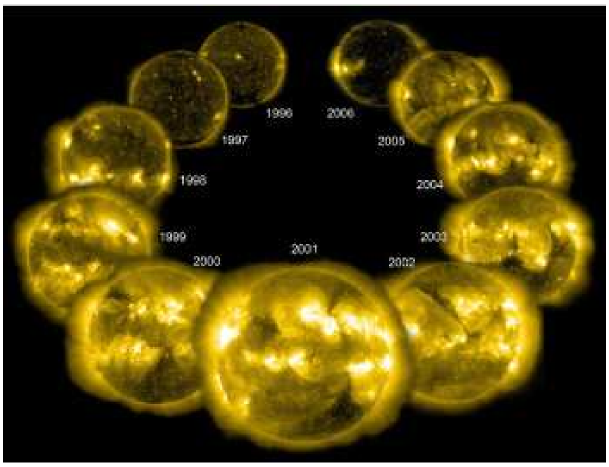

Figure 2.4: The solar corona as seen with SOHO in the extreme ultraviolet over one complete activity cycle (picture credit: ESA/NASA).

A successful model would also have to explain apparent "hiatus" phases of the solar cycle. The most prominent of these phases was the Maunder Minimum lasting from 1645 to 1700, when the Sun showed extremely few sunspots. Eddy (1976) showed that this was a true quantitative effect and not the result of some historical selection effect. Other such minima were less extreme, for example the Spörer minimum from 1460-1550, as inferred from carbon-14 analysis in tree rings, and the Dalton minimum from 1790-1830.

Even very recently, debates arose whether the very pronounced activity minimum of the solar cycle persisting in 2008 and 2009, when sunspot numbers dropped to a hundred-year low, might be the beginning of a new long-term minimum state. In 2010, however, the solar activity level rose again, and in February 2011, the first very powerful solar flare (categorized as an X class flare) of the new cycle occurred. This vividly shows that the current understanding of solar, let alone stellar, activity is still limited.

2.3 Observing magnetic activity in stars

Typical activity features of the Sun such as sunspots and flares are linked to its magnetic field. Sunspots appear when loops of magnetic field lines pierce the solar surface, preventing patches of the photosphere from convecting downwards and fresh material from floating upwards, so that these patches cool and become darker than their surroundings. Flares are thought to happen when these magnetic loops tangle up from photospheric motions of their footpoints (the sunspots) and finally reconnect in order to transit to a state of lower energy. Electrons are accelerated downwards along the magnetic field lines and collide into the deeper atmospheric layers, causing them to heat up and to evaporate partly into the corona.

One of the very basic consequences of the solar magnetic field is the existence of a chromosphere and a corona itself, as these outer thin layers of the stellar atmospheres need to be heated to the observed temperatures of $\lesssim$ 20000 K for the chromosphere and several 10^6 K for the corona. For a long time it was debated if this heating process is of predominantly acoustic or magnetic nature. By now, the scientific consensus is that the chromosphere is heated by a combination of "basal" acoustic heating in the lower layers and dominant magnetic heating in the middle and upper layers (Priest 1982). The corona actually has no constant "quiescent" base level of X-ray emission. How the corona is heated exactly is still one of the outstanding problems in solar and stellar astrophysics; in any case, magnetic fields have to play an important role in the heating process, as observations show that coronal lightcurves can be simulated as superpositions of flares of different sizes (Kopp & Poletto 1993), pointing towards a flare-related heating.

When observing stars other than the Sun, features on the stellar surface usually cannot be resolved angularly. Therefore activity is usually measured in disk-integrated quantities. The two most widely used activity indicators are chromospheric Ca II H and K line emission and coronal X-ray emission; other methods try to reconstruct spot patterns or measure the stellar magnetic field itself.

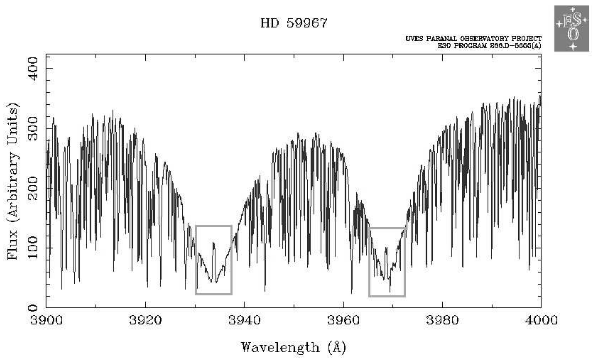

Figure 2.5: Ca II H and K line profile of a star with approximately the same mass as the Sun (HD 59967 from the *UVES* spectral atlas[1]). The emission features in the line cores, marked by grey boxes, are clearly visible.

2.3.1 Chromospheric activity

The connection of emission in the Ca II resonance lines and magnetic activity is somewhat intricate. These lines owe their extensive use to the fact that they are easily observable in the blue part of the visible part of solar spectrum, and produce remarkable absorption lines (Fig. 2.5); emission in the line cores is prominent for example in solar active regions.

The Ca II H and K lines arise from a combination of different effects. The absorption profile of Ca II H and K lines from the photosphere has a broad triangular shape. Calcium ions present in the chromosphere produce emission features again if chromospheric temperatures are sufficiently high. The source function, which is the ratio of emission to absorption per unit volume, of Ca II (or any other ionized metal) is collisionally controlled at these temperatures, while the source functions of neutral metals are in general radiatively controlled (Thomas 1957). This means that Ca II emission is a good tracer of chromospheric temperature, as the higher energy level is mainly populated by collisions with other particles. The double peak of the emission stems from self-

[1] www.sc.eso.org/santiago/uvespop/field_stars_uptonow.html

absorption in higher chromospheric layers. So, Ca II emission is a proxy for chromospheric temperature; as the chromosphere is mostly magnetically heated, it is also a proxy for magnetic activity. However, also in the absence of activity features, a small amount of emission in the line cores is present. This basal emission is probably caused by a low level of acoustic heating in the chromosphere, which makes an absolute calibration of Ca II emission and magnetic activity problematic, especially for low-activity stars.

Most other chromospheric spectral lines lie in the ultraviolet, making measurements more difficult since they cannot be observed with ground-based telescopes; exceptions are the Hα line in the optical and the Ca II infrared triplet.

2.3.2 Photospheric measurements

There are several observational methods to gather information on stellar magnetic activity from photospheric measurements.

One of them is the reconstruction of spot distributions on the stellar surface from lightcurve analysis or Doppler Imaging. In lightcurve reconstructions, one uses long-term lightcurves as they are for example routinely collected by space-based planet-search missions such as *Kepler* or *CoRoT*. Spots on the host star will cause periodic fluctuations of the stellar brightness. If the star is rotating sufficiently fast, so that the typical lifetime of a spot is much longer than the rotational period, one can model the stellar surface from the modulations of its lightcurve (theoretical groundwork by Wild (1989, 1991)). Even modulations during planetary transits can be used to "scan" the stellar surface more closely (Pont et al. 2007; Wolter et al. 2009). However, such reconstructions are not unique, and constraints such as maximum entropy criteria have to be used.

In Doppler Imaging, one uses the modulation that a spot causes in absorption lines to reconstruct the stellar surface (Vogt et al. (1987); for a review see Strassmeier (2002)). In a rotationally broadened absorption line, a dark spot causes deviations from the mean line profile in the blue or red wing, depending on its current position on the stellar hemisphere rotating towards or away from the observer. This is similar to the Rossiter-McLaughlin effect caused by planetary transits in stellar spectra. Again, the reconstruction needs additional assumptions since there are no unique solutions.

Another method uses the magnetic Zeeman splitting of photospheric spectral lines which causes spectral line broadening in unpolarized light; more detailed information can be extracted from polarized light, as the Zeeman splitting manifests itself in different line profiles depending on the polarization. This can be measured with a spectropolarimeter, which basically consists of a polarimeter which splits the beam into differently polarized components before it is fed into a normal high-resolution spectrograph. In principle, this method allows a reconstruction of the stellar magnetic field (Donati et al. 1997; Piskunov & Kochukhov 2002). However, the Zeeman signals are typically very small, and in addition to the ususally non-unique solutions one derives from such calculations, the theoretical formalism for reconstructing the magnetic field is much more complicated than for reconstructing spot patterns. Still, gaining information on the magnetic field itself and not only its proxies from spots or chromospheric and coronal emission can yield valuable insights into stellar magnetospheres that cannot be achieved otherwise.

2.3.3 Coronal activity

The observational proxy for stellar activity that is predominantly used in this thesis is coronal X-ray emission.

As we know from solar observations in the extreme UV, the solar corona is composed of magnetic loops (see Fig. 2.6). These coronal loops are filled with hot, thin plasma with temperatures of one million Kelvin and more, emitting at X-ray energies (> 100 eV). One usually extrapolates this concept to stars other than the Sun, even if we cannot resolve X-ray structures on these stars with current instrumentation. However, also in stars there are many indications that coronal loops of different sizes are the building blocks of the corona, see section 2.3.5.

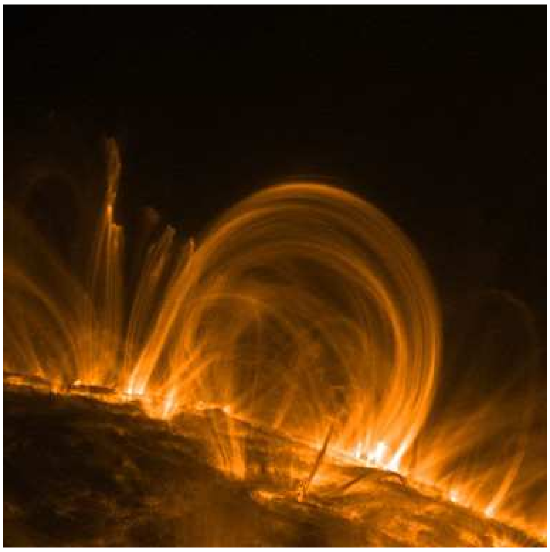

Figure 2.6: Highly structured coronal loops on the Sun, imaged in an extreme UV passband that tracks temperatures of $\approx 1-2$ MK (picture credit: *TRACE* / NASA).

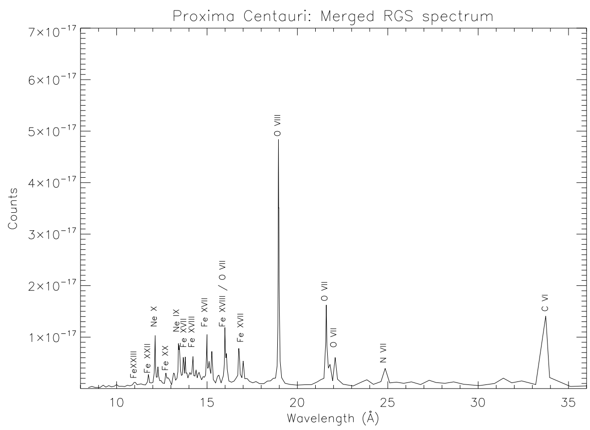

Figure 2.7: Merged X-ray spectrum of Proxima Centauri, obtained with *XMM-Newton's* RGS spectrographs. The strongest spectral lines are from oxygen, iron and neon.

A coronal spectrum differs from the usual photospheric and chromospheric spectra which are dominated by absorption lines, since the the hot plasma of the corona is optically thin. Ions are excited by collisions with electrons and de-excited by radiation, i.e. X-ray emission. At typical coronal temperatures of $1-5$ MK for stars with low to moderate activity, most of the emission is through spectral lines (see Fig. 2.7). At higher temperatures, thermal bremsstrahlung becomes relevant and forms a continuum in addition to the spectral lines present.

2.3.4 X-ray instrumentation

X-ray photons can travel through the Earth's atmosphere only for a few meters before they are absorbed. This is good for lifeforms on Earth, since they are protected from high-energy radiation from space, but difficult for X-ray astronomy: any astronomical X-ray observation has to be performed from space.

There have been several space-based missions to observe the Sun or stars in X-rays. To mention a few space observatories used for solar coronal research, there was the *Skylab* space station (1973-1979), the *Yohkoh* X-ray telescope (1991-2005), the Transition Region And Coronal Explorer *TRACE*, monitoring solar UV and extreme UV emission (1998-2010), the Solar And Heliospheric Observatory *SOHO* which operates in the extreme UV (since 1995), and operating since 2010, the Solar dynamic observatory *SDO*, which observes the Sun in the extreme UV with very high spatial and temporal resolution.

Stellar X-ray astronomy had an amazing breakthrough with the *Einstein* satellite (1978-1981), which detected hundreds of stars in X-rays, while only a handful of extremely active objects had been detected with earlier missions. The German Röntgensatellit *ROSAT* (1990-1999) yielded more than 50000 detections of stellar coronae in its all-sky survey and pointed observations. Some other X-ray missions were *BeppoSax*, *EXOSAT*, *RXTE* and *ASCA*. Today, the main workhorses for X-ray astronomy are ESA's X-ray Multi-Mirror Mission *XMM-Newton* and NASA's *Chandra* X-ray observatory, both launched in 1999. These two X-ray missions are complementary in the sense that *Chandra* (Weisskopf et al. 2000) is optimized for high angular resolution, while *XMM-Newton* (Jansen et al. 2001) has superior sensitivity in most of the accessible energy ranges.

As X-ray photons are not reflected by ordinary mirrors, the X-ray observatories use telescopes of the Wolter type. X-rays can only be reflected at grazing incident angles; therefore Wolter telescopes have a shape that reminds of a champagne glass, consisting of nested metallic paraboloidal and hyperboloidal mirrors. The neccessity of a grazing angle makes the effective area of these telescopes small compared to an optical ground-based telecope. For *XMM-Newton*, the maximum effective area for a single detector is ca. 1300 cm^2, for *Chandra* it is ca. 700 cm^2 (for comparison, the largest mirrors of the *VLT* have a size of ca. 500000 cm^2).

The detectors used on board of *XMM-Newton* and *Chandra* are largely similar to each other. Both use CCD detectors and grating spectrometers; additionally, *XMM-Newton* has an optical monitor, while *Chandra* has a micro-channel plate detector for X-rays, the HRC. The CCD detectors yield X-ray images from which X-ray spectra of moderate energy resolution ($FWHM$ typically around 80 eV) can be extracted. The novelty compared to earlier X-ray missions is that both observatories have grating spectrometers with resolutions of up to $\Delta\lambda/\lambda \approx 1000$. This allows to identify and quantify emission in individual spectral lines of stellar X-ray spectra, making detailed analyses of temperatures, emission measures and also coronal densities possible.

2.3.5 X-ray properties of cool stars

Our current understanding of stellar X-ray emission is that cool stars, meaning stars with outer convection zones, exhibit activity features that resemble the Sun's, but there are also properties that are unknown from solar behavior.

For cool stars, there is a clear correlation of stellar rotation and X-ray activity, suggesting a solar-like dynamo is at work in these stars. The X-ray activity level is usually measured by the quantity $\log L_X/L_{bol}$, which spans a range of -3 to -7 in the $0.2 - 10$ keV energy band for stars with coronae. The rotation-activity relation, more conveniently expressed as a relation of X-ray activity and Rossby number which depends on stellar rotation and the convective turnover time, (super)saturates for very fast rotators; reasons for this may be the saturation of the dynamo itself, the saturation of stellar surface filling with active regions, or effects of strong centrifugal forces on coronal loops.

The reason for this rotation-activity relationship is in fact a relationship of stellar age and activity. Young stars start out as fast rotators with rotation periods of often less than a day, but with time, they slow down by magnetic breaking. This comes from the fact that cool stars drive ionized winds. This plasma moves outwards along large-scale or open stellar magnetic field lines, causing the star to spin down as the angular momentum is conserved. This is nicely illustrated by an ice scater performing a pirouette, who will slow down when stretching out his or her arms.

There is apparently no quiescent, constant level of X-ray emission for stars (or the Sun). Typical stellar X-ray lightcurves show a considerable amount of short-, medium- and longterm variability, and it has been shown (Kopp & Poletto 1993) that typical X-ray lightcurves can be formed by a superposition of few large flares and an increasingly larger number of small flares ("nanoflares"). There seems to be a minimal surface flux for cool stars (Schmitt 1997) that coincides with the X-ray surface flux of a solar coronal hole. This indicates that very inactive stars might be covered mostly by coronal holes, with very few closed coronal loops of significant size.

Stellar X-ray flares can be much more energetic than flares observed on the Sun. Flares with emitted energies orders of magnitudes larger than solar flares have been observed, especially for young stars (Preibisch et al. 1995; Tsuboi et al. 1998). For some stellar flares, the Neupert effect which was first recognized for the Sun (Neupert 1968) has been detected. It states that flares are first detected in the radio, optical, or hard X-ray regime before a rise in soft X-ray emission is observed. The time-integrated lightcurve of these wavelengths then is proportional to the rising part of the soft X-ray lightcurve. Radio, optical and hard X-ray emission trace the accelerated electrons causing chromospheric evaporation, while the plasma evaporated into the corona increases the existing coronal emission measure and therefore the soft X-ray luminosity. However, not all flares follow this standard picture; flares without preceding radio emission or non-matching lighcurve profiles have been observed as well.

Understanding stellar flares would be much easier if stellar coronal loops could be observed directly; this is not possible because current instrumentation does not provide sufficient angular resolution. However, information on coronal loops of cool stars can be inferred from a set of sophisticated analyses. Density diagnostics during flaring and non-flaring times are possible through line intensity ratios in helium-like triplets such as the O VII and Ne IX triplet (Porquet et al. 2001). Such an analysis makes use of the fact that in a helium-like triplet, where a resonance, an intercombination and a forbidden emission line are present, the ratio of the forbidden and the intercombination line depends on the plasma density. This is because in a high-density environment ions in the excited state of the forbidden line can be excited by collision into the upper level of the intercombination line, from where the de-exite radiatively. So, in a high-density plasma the forbidden line is weaker and the intercombination line is stronger than in a low-density plasma. However, some care has to be taken for stars with strong ultraviolet radiation, as the transition from the forbidden to the intercombination state can also be triggered by UV photons.

Furthermore, positions of active regions on the stellar surface can be obtained for eclipsing binary systems (Schmitt et al. 2003). Assuming that a single loop is involved in a given flare, the loop length can be inferred from the decay time of the flare lightcurve (van den Oord & Mewe 1989; Serio et al. 1991). Deriving more detailed information on flaring loops and reheating during the flare is possible by investigating the evolution of coronal emission measure and temperature through time-resolved spectroscopy (Reale et al. 1997). So far, there is evidence for a variety of stellar coronal configurations, depending on the observed star: there are small and large coronal loops, intense coronae located at the poles or near the equator; the filling factors even for active stars seem to be rather small, but X-ray observations are most sensitive to dense regions of the corona, so regions filled with loops of low density might go undetected.

Also the chemical composition of stellar coronae has been studied, and significant progress has been made since the advent of the high-resolution spectrographs of *XMM-Newton* and *Chandra*. The abundances of chemical elements in the solar corona show a trend with the **f**irst **i**onization **p**otential, the so-called FIP effect: elements with low FIP, such as iron, calcium and silicon, are enriched with respect to hydrogen when compared to the photospheric composition, whereas the high-FIP elements (oxygen, neon, carbon, nitrogen) have photospheric abundances (Feldman 1992). In stellar coronae, this effect is activity-related. Stars of low to moderate activity, measured by the ratio of X-ray luminosity to bolometric luminosity $\log L_X/L_{bol} \lesssim -5$, show a solar-like FIP effect, while very active stars with hot coronae $T \gtrsim 10$ MK often show an inverse FIP effect, where the high-FIP elements are overabundant compared to the low-FIP elements (Audard et al. 2003). The reason for the FIP effect is not entirely clear. Some kind of fractionation process takes place in chromospheres, where low-FIP elements are already ionized and high-FIP elements are mostly neutral; they thus experience magnetic and electric fields differently (for a review, see Jordan et al. (1998)).

2.4 Open questions

Stellar activity in the corona and chromosphere still provides many unsolved problems. How stellar coronae are structured, how exactly the heating of coronae takes place, what kind of magnetic dynamos operate in stars of different masses, and what processes drive stellar flares with or without the Neupert effect being detected, are just a few of the important issues that need to be resolved in the future. Some of the questions concerning coronal and chromospheric activity are addressed in this thesis:

2.4.1 Maunder minima

We know of three phases in the life of the Sun when it displayd very low activity (the Maunder, Dalton and Spörer Minima, of which the Maunder Minimum was the most extreme), so it is natural to expect that some other stars are in corresponding Maunder minima as well. Initially, a large number of stars (30%, later corrected to $10-15\%$) was assumed to be in a Maunder minumum based on chromospheric activity measured in the Mount Wilson project (Saar & Baliunas 1992). However, it was shown by Wright (2004) that most of these stars were actually evolved stars, making their chromospheric activity indices incomparable to main sequence stars. Additionally, chromospheric activity is always influenced by a small amount of basal acoustic heating, making X-ray and EUV measurements necessary to truly assess if a star is in a Maunder minimum (Judge & Saar 2007). In chapter 4, I give a detailed investigation of the activity profile of the planet-hosting 51 Peg, deriving from X-ray and optical data that the star is most probably in a Maunder minimum state.

2.4.2 Stellar activity cycles

An activity cycle as the Sun displays has been found in chromospheric Ca II H and K lines for a multitude of stars in the Mount Wilson project (Baliunas et al. 1995). X-ray analogues of these chromospheric cycles have been found only for a few targets (Hempelmann et al. 2006; Ayres 2009), while other stars at least show some outliers in X-rays from the chromospheric behavior (Favata et al. 2008). Additionally, there are no reliable models for predicting activity cycles from fundamental stellar parameters. It is therefore crucial to gather more evidence for coronal activity cycles to be able to understand magnetic dynamos in cool stars. For the quite fast-rotating star τ Boo ($P_* = 3.3$ d), a very short activity cycle of only one year duration has been derived from magnetic maps reconstructed from spectropolarimetric Zeeman signatures (Catala et al. 2007; Donati et al. 2008; Fares et al. 2009). In chapter 8, I present an analysis of this star's coronal properties during its proposed activity cycle. During 2011 and 2012, more optical and X-ray data will be collected on this star, and a complete analysis will be published in a peer-reviewed journal then. However, the existing datasets already allow some interesting insights which are described in this thesis.

Chapter 3

Exoplanets and their host stars

The question if we as living beings are alone in the universe has been pondered on for centuries. A famous formula postulated by Drake (1961) multiplies the star formation rate, the fraction of stars hosting planets, the fraction of habitable planets in a planetary system and other quantities relating to the development of life forms to derive the number of hypothetical civilizations with whom communication might be possible. In Drake's original estimates, this results in about two hundred civilizations in our galaxy existing at a given time. After sixteen years of exoplanet detections, the astronomical community is making progress in determining the fraction of stars which actually host planets. However, a habitable planet dubbed "second earth" has not yet been found. Actually, many exoplanets detected so far differ significantly from the planets in our solar system. Many giant exoplanets orbit their host stars with very short orbital periods of less than five days, unlike Jupiter in the solar system. Probably it were our own expectations that hampered the detection of the first exoplanets in the early years, as scientists were looking for massive, wide-orbit planets. Also, exoplanets are often found in eccentric orbits or are tidally locked to their host star, with the same side of the planet facing the star all the time. Therefore the concept of the habitable zone, usually meaning the orbital range where a planet could have water in liquid form, needs to be modified for several effects in exoplanets which are negligible in the solar system (Lammer et al. 2009; Barnes et al. 2010).

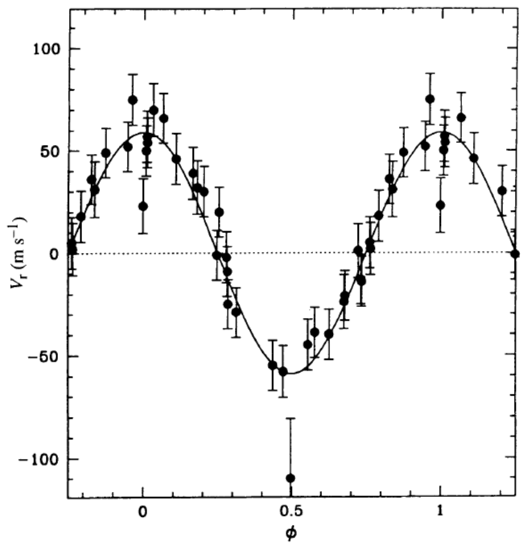

Figure 3.1: Radial velocity curve of the planet-hosting star 51 Peg. The RV amplitude is $\approx \pm 60$ m s^{-1}, yielding a planetary mass of $M_p \sin i = 0.47 \pm 0.02\, M_J$ (Mayor & Queloz 1995).

3.1 Detection of exoplanets

A variety of observational methods has been employed in the hunt for exoplanets. The most successful one so far, in terms of total detected planets, is the radial velocity (RV) method. As a star and its hypothetical companion orbit around their common center of mass, there will be a Doppler shift in the spectrum of the star as it moves towards and away from the observer during one orbit. This periodic change in radial velocity can be used to calculate the mass ratio of the companion and the star times the sine of the orbital inclination (see Fig. 3.1). When the stellar mass is derived from the spectral type of the star using suited theoretical models, the remaining free parameters are the companion's mass and the orbital inclination. Therefore the RV method alone yields only lower limits to planetary masses as long as the inclination of the system is unknown.

The second very successful detection method is the search for planetary transits. If the orbital inclination of a star-planet system is close to 90°, the planet can cross the line of sight from the observer to the star, occulting a small part of the star during this (primary) transit. From the duration, the depth and the ingress and egress profiles of the transit, the ratio of planetary to stellar radius can be determined. Practically, finding a good model for the limb darkening of the star, which affects in- and egress profiles, is one of the major complications of transit analysis. The transit method as such is not suited to derive planetary masses, it only yields radii. Therefore all transit detections have to be confirmed by RV measurements to exclude brown dwarfs or low-mass stellar companions as the cause for observed transits; since the inclination is approximately known from the occurence of the transit, the companion's mass can be determined. As of February 2011, there are 312 (released) planet candidates detected by the *Kepler* space telescope awaiting possible confirmation from RV observations.

Other detection methods such as astrometry, direct imaging, microlensing and timing analysis have been successful as well, but yielded a far lower number of planet detections than the RV or transit method.

3.2 Interactions between stars and planets

We know from our own solar system that planets are affected by their host star's activity. A prominent example are the northern lights, caused by the solar wind hitting earth's magnetosphere, which guides energetic electrons and protons into the atmosphere where they collide with atomic and molecular oxygen and nitrogen.

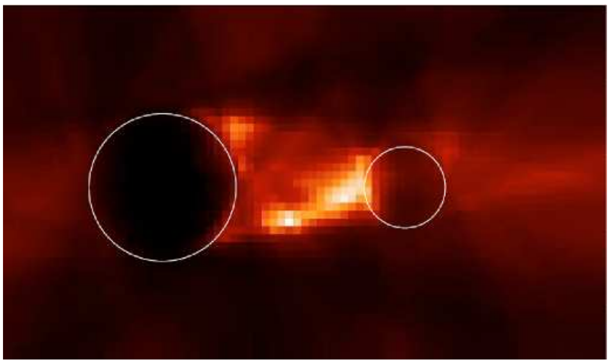

Figure 3.2: Coronal image of AR Lac, reconstructed from an *ASCA* X-ray lightcurve (Siarkowski et al. 1996).

For exoplanets which orbit their host star at very close distances, more extreme effects might take place. It has been claimed that the giant planet HD 209458 b undergoes atmospheric evaporation due to the irradiation by its host star (Vidal-Madjar et al. 2003), although this detection is somewhat debated (Ben-Jaffel 2007).

Interactions that lead to effects from the planets on the Sun have not been observed in the solar system. However, it is well known that massive companions, such as in binary stars, can have severe effects on each other. Binaries are often much more active than single stars of the same spectral class, which is caused by tidal locking and therefore faster rotation of the components of the binary. In addition, periodic flaring has been observed for young binary systems at millimeter and centimeter wavelengths, with the flares occuring during periastron (Massi et al. 2002; Salter et al. 2010); corresponding X-ray flaring has been observed as well (Getman et al. 2011). Also, reconstructions from X-ray lightcurves of the active binary AR Lacertae suggest that there may be interaction of the two stars leading to X-ray emission from the area between them (see Fig. 3.2). These observations led to the idea that stars with close-in giant planets, regarded as binaries with a very small mass ratio, might exhibit effects on stellar activity from these kinds of interaction as well.

Several theoretical models exist of how

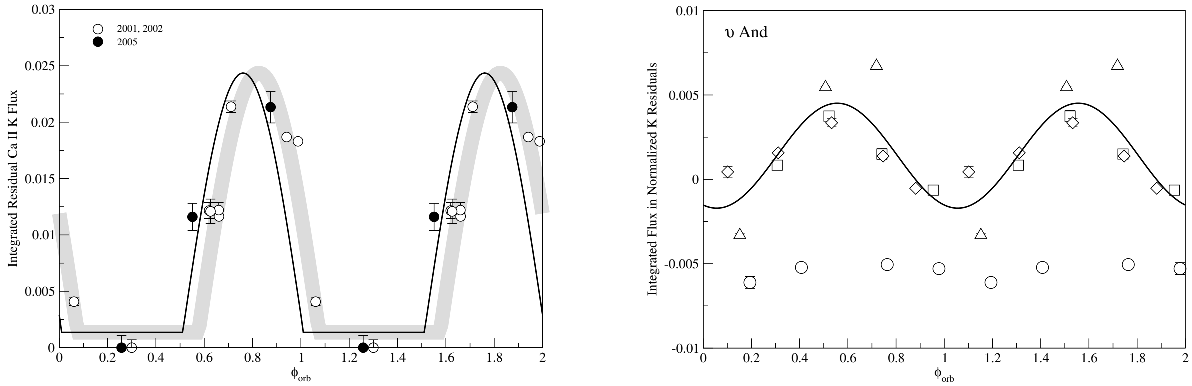

Figure 3.3: Chromospheric activity, as measured by Ca II K line emission, phase-folded with the planetary orbital period for the planet-hosting stars HD 179949 (left) and υ And (right, the different symbols represent observations in different years) (Shkolnik et al. 2005, 2008).

such star-planet interactions (SPI) could work, which can be divided into two main classes of interaction types: tidal and magnetic interaction.

3.2.1 Tidal interaction

Tidal interaction may cause tidal bulges on the star. If the planet and its host star are not tidally locked in the sense that the stellar rotation period equals the planetary orbital period, this will effectively cause bulges to rise and subside on fixed areas on the stellar surface. This may increase turbulent motions in the stellar photosphere, causing faster entanglement of coronal loops by motions of their footpoints in the photosphere. Also, waves may be excited by the compression and expansion due to the tidal bulges. Finally, even an amplification of waves in outer atmospheric layers may occur. These effects could in principle lead to increased high-energy emission of the star. Detailed quantitative calculations of such increased emission have not been performed yet; however, Cuntz et al. (2000) give estimates on the height of SPI-induced tidal bulges. They calculate the gravitational perturbation $\frac{\Delta g_*}{g_*}$ caused by the planet as

$$\frac{\Delta g_*}{g_*} = \frac{M_{pl}}{M_*}\frac{2R_*^3}{(d-R_*)^3} \tag{3.1}$$

and the height of the induced tidal bulge as

$$h_{tide} = \frac{1}{2}\frac{\Delta g_*}{g_*}R_*, \tag{3.2}$$

with R_* and M_* being the stellar radius and mass, M_{pl} the planetary mass, and d the distance between planet and star. This typically yields tidal bulge heights of $0.1-10\%$ of the respective photospheric pressure scale height, or in absolute units up to ca. 10 km, for stars with close-in ($d \lesssim 0.1$ AU) planets.

3.2.2 Magnetic interaction

The magnetic interaction scenario has several variants. Magnetic interaction could happen through reconnection of planetary and stellar magnetic field lines. A model for this kind of interaction has been presented by Lanza (2008, 2009). The dissipated power from SPI is estimated in that model to be

$$P_{diss} \propto B_a^2 R_m^2 v_{rel}, \tag{3.3}$$

with R_m being the radius of the planetary magnetosphere

$$R_m = R_{pl}\left(\frac{B_a}{B_{pl}}\right)^{-1/3}, \tag{3.4}$$

B_a being the stellar magnetic field strength at the boundary of the planetary magnetosphere, B_{pl} the planetary magnetic field strength, R_{pl} the planetary radius, and v_{rel} the relative velocity between the planet and the stellar magnetic field. For the system HD 179949, which hosts a $0.95\,M_{jup}$ planet in a 3.1 d orbit, this yields a dissipated power of only $\sim 10^{24}$ erg s^{-1}; this is smaller than the detection limit of *XMM-Newton* or *Chandra* for X-ray luminosities of nearby stars. However, much larger dissipated powers can theoretically be achieved when the stellar coronal loops tangle up by normal activity processes, and are then disturbed by the planetary magnetic field, triggering reconnection and thus flares. This is similar to the normal flaring process of a star, with the difference that flares would preferentially occur near the subplanetary point.

Another variant was presented by Cohen et al. (2009), where the mere presence of the planetary magnetosphere is thought to hinder the expansion of the stellar coronal magnetic field, such that field lines which would normally open up will stay closed. In the model, this causes locally higher coronal temperatures and larger emission measure since the plasma does not escape from the loop and thus yield a higher X-ray luminosity of the star. Enhanced soft X-ray emission of up to a factor of 14 has been modelled this way.

The magnetic interaction process could also be similar to the Jupiter-Io interaction in the solar system, where Jupiter displays auroral features caused by Io, and, somewhat weaker, by Europa and Ganymede. These auroral footprints are caused by two flux tubes which connect Io to the polar regions of Jupiter. Io displays strong volcanism that causes an ionosphere; Io itself therefore is a good conductor, and through the relative motion of the flux tubes with respect to Jupiter's magnetic field, an electric current along the flux tubes is generated in the way of a unipolar inductor (Goldreich & Lynden-Bell 1969). The particles carrying the current then produce the auroras by collisions with Jupiter's atmosphere. For this specific mechanism to be applied to stars and their planets it is necessary that the host star rotates faster than the planetary orbit (cf. Jupiter's rotation period of ≈ 10 h and Io's orbit of ≈ 1.8 d), which is not the case for most of the exoplanetary systems known today. For systems where these conditions apply, the resulting dissipated power has been calculated as (Schmitt 2009)

$$P_{diss} \propto (\frac{2\pi}{P_{orb}})^{13/3} \frac{B_*^2 R_*^6 R_{pl}^2}{(GM_*)^{5/3}} (\frac{P_{orb}}{P_*} - 1), \quad (3.5)$$

with P_{orb} being the planetary orbital period, P_* the stellar rotation period, and B_* the the magnetic field strength at the stellar surface. With realistic values for these quantities, dissipated powers of up to 10^{29} erg s^{-1} can be reached. Other models take into account the stellar wind in such systems to explain planet-induced hot spots which have a phase lag with respect to the subplanetary point (Preusse et al. 2006).

3.2.3 Observing SPI signatures

Gaining observational evidence of star-planet interactions has proven to be a subtle business. The first detection of such signatures was claimed in 2005, when two out of thirteen stars monitored for chromospheric activity showed changes that were compatible with their respective innermost planet's orbital period (see Fig. 3.3). Repeated observations in subsequent years, however, yielded activity changes which were mostly compatible with the stellar rotation period, not the planetary orbit.

As coronal X-ray emission is a prominent feature of stellar magnetic activity, there have been several attempts to identify coronal signatures of star-planet interactions. Activity features in single planet-hosting stars such as X-ray flares or elevated mean countrates that coincide with the position of the planet have been observed (Saar et al. 2008; Pillitteri et al. 2010), but attributing them unambiguously to star-planet interactions is difficult, since late-type stars usually display a considerable amount of intrinsic X-ray variability even if they do not host planets.

A convenient way to average out short-term X-ray activity changes is to analyze a large sample of planet-hosting stars in order to look for increased average activity levels which may correlate with planetary parameters. This has been done by several authors with the result that the planetary semimajor axis or, for close planets, the planetary mass correlates with the X-ray luminosity of the host star (Kashyap et al. 2008; Scharf 2010). However, there can be significant selection effects in dealing with such samples. These selection effects can be caused by not accounting for X-ray flux limits in survey data. Other possible selection effects stem from the planet detection methods which can introduce correlations of several stellar and planetary parameters.

3.3 Open questions

The young research field of star-planet interactions presents lots of fundamental unanswered questions, some of which are investigated in this thesis.

3.3.1 Evidence for chromospheric SPI

Observational hints for planet-induced chromospheric variability are available for only a small number of stars (Shkolnik et al. 2005, 2008; Lenz et al. 2010). I therefore monitored the star υ Andromedae, one of the stars claimed to exhibit such chomospheric SPI signatures (Shkolnik et al. 2005), for six months in the optical and in X-rays to characterize its chromospheric and coronal activity variations in detail. The results are presented in chapter 6.

3.3.2 Evidence for coronal SPI

Coronal emission is more strongly variable with the activity level than chromospheric emission is, as can be seen from the cyclic variations of the few stars for which activity cycles have been found both in X-rays and chromospheric emission (Hempelmann et al. 2006; Ayres 2009), and of course for the Sun itself. Thus one might see effects of SPI on the X-ray emission of a planet-hosting star. As stellar coronal emission of an individual star is highly variable also in absence of planets, it is favorable to work with stellar samples here and look for trends of X-ray properties with planetary mass and semimajor axis. I present the first X-ray analysis of a complete sample of all known planet-hosting stars within 30 pc distance from the Sun in chapter 5.

3.3.3 Selection effects in samples of planet-hosting stars

A striking correlation between planetary mass and X-ray luminosity for stars with very close planets has been published Scharf (2010), using data from the *ROSAT* All-Sky Survey (RASS). If truly SPI-related, this would be an amazing discovery. However, such a correlation is not present in the complete sample from Poppenhaeger et al. (2010), which uses X-ray data from both survey and pointed observations. Therefore I conducted a detailed analysis of possible selection effects which are present in flux-limited survey data and in the sample of known nearby planet-hosting stars themselves, as the predominant detection mechanism (radial velocity) gives rise to severe trends which can be interpreted as SPI signatures if not taken into account carefully. This is discussed in chapter 7. This chapter contains a manuscript which has been submitted to *The Astrophyical Journal* for publication. The manuscript is still being refereed at the time of writing this thesis; the comments from the referee are already included, but final acceptance has not been given yet. I expect to publish the paper without any significant changes from the version which is presented here.

Chapter 4

51 Pegasi - a planet-bearing Maunder minimum candidate

K. Poppenhäger, J. Robrade, J. H. M. M. Schmitt and J. C. Hall
Astronomy & Astrophysics, Volume 508, Issue 3, pp.1417-1421 (2009)
The original publication is available at www.aanda.org

A&A 508, 1417–1421 (2009)
DOI: 10.1051/0004-6361/200912945

Astronomy & Astrophysics

51 Pegasi – a planet-bearing Maunder minimum candidate

K. Poppenhäger[1], J. Robrade[1], J. H. M. M. Schmitt[1], and J. C. Hall[2]

[1] Hamburger Sternwarte, University Hamburg, Gojenbergsweg 112, 21029 Hamburg, Germany
e-mail: katja.poppenhaeger@hs.uni-hamburg.de
[2] Lowell Observatory, 1400 West Mars Hill Road, Flagstaff, AZ 86001, USA

Received 21 July 2009 / Accepted 7 October 2009

ABSTRACT

We observed 51 Peg, the first detected planet-bearing star, in a 55 ks *XMM-Newton* pointing and in 5 ks pointings each with *Chandra* HRC-I and ACIS-S. The star has a very low count rate in the *XMM* observation, but is clearly visible in the *Chandra* images due to the detectors' different sensitivity at low X-ray energies. This allows a temperature estimate for 51 Peg's corona of $T \lesssim 1$ MK; the detected ACIS-S photons can be plausibly explained by emission lines of a very cool plasma near 200 eV. The constantly low X-ray surface flux and the flat-activity profile seen in optical Ca II data suggest that 51 Peg is a Maunder minimum star; an activity enhancement due to a Hot Jupiter, as proposed by recent studies, seems to be absent. The star's X-ray fluxes in different instruments are consistent with the exception of the HRC Imager, which might have a larger effective area below 200 eV than given in the calibration.

Key words. stars: coronae – stars: activity – stars: individual: 51 Peg – X-rays: stars – X-rays: individuals: 51 Peg

1. Introduction

The star 51 Peg (GJ 882, HD 217014) shot to fame in 1995 when Mayor & Queloz (1995) detected an exoplanet in its orbit, the planetary parameters being quite unexpected at that time, because 51 Peg b is a giant planet, located at only 0.05 AU distance. The star itself is a G5V star 15.4 pc away from the Sun. Its properties are quite similar to the Sun's, since 51 Peg is about 4 Gyr old and its mass, radius and effective temperature are comparable to solar values with $R = 1.27\ R_\odot$ (Baines et al. 2008), $M = 1.11\ M_\odot$, $T_{\rm eff} \approx 5790$ K (Fuhrmann et al. 1997). However, 51 Peg is a metal-rich star, for which the metallicities given in the literature vary over a wide range of $+0.05 \leq$ [Fe/H] $\leq +0.24$, see for example Valenti & Fischer (2005). Enhanced metallicities are a common feature of stars with giant planets (Gonzalez 1997; Santos et al. 2001).

The activity profile of 51 Peg turned out to be unspectacular. In the Mount Wilson program (Baliunas et al. 1995), which monitors the Ca II H and K line fluxes of main sequence stars, the star shows a very low and nearly flat chromospheric activity level from 1977 until 1989 and a slight drop in 1990 and 1991. In the Lowell Observatory program (Hall et al. 2007), it also shows low activity and little variability in Ca fluxes since the beginning of the program in 1994. The star was also observed in a 12.5 ks *ROSAT* PSPC pointing in 1992 and detected as a weak X-ray source.

The coronal activity of 51 Peg is of interest not only because the star is similar to the Sun, but also with regard to recent studies (Kashyap et al. 2008), which claim stars with close-in giant planets to be more X-ray active than stars with far-out ones.

2. Observations and data analysis

We observed 51 Peg on two occasions in 2008. A 55 ks *XMM-Newton* was carried out on June 1, 2008, and with *Chandra*, we observed 51 Peg for 5 ks each using HRC-I and ACIS-S on December 6, 2008 immediately after each other. The specific observation details are listed in Table 1.

2.1. XMM-Newton data analysis

The *XMM-Newton* data were reduced using the Science Analysis System (SAS) version 8.0.0. Standard selection criteria were applied for filtering the data. In the full-time image obtained with the PN detector, the automatic source detection procedure finds a faint X-ray source with 32 excess counts at 51 Peg's nominal position when using the 0.2–1 keV energy band. This choice is motivated by 51 Peg being detected in the 1992 *ROSAT* PSPC pointing as a very soft X-ray source. Because of the weak signal, we merged both MOS detectors. In the RGS, no relevant signal was present. The PN observation is affected by proton contamination, therefore we used only time intervals (GTI) where the high-energy background averaged over the detector is below 0.8 cts/s, leading to a PN GTI of 29 ks.

Since spectral fitting results are not very reliable with this low number of counts, we conducted a study in different energy bands instead and investigated the recorded counts within the source region, a radius of 15″ around 51 Peg's nominal position for the PN and MOS instruments. The source region size of 15″ radius was chosen because of the rather broad point spread function, which contains 72% (68%) of the photons from a point-like source in the PN (MOS) detector. Background counts were extracted from source-free nearby regions, which are located on the same chip for the MOS detector; for the PN detector, two background regions were chosen, one on the same chip as the source and one on a neighboring chip. Since 51 Peg proved to be a very soft X-ray source in the previous *ROSAT* observation, we expect most X-ray photons to be produced from the O VII triplet or lines with even lower energies, such as N VII/VI and C VI/V. We therefore specified three energy bands for our analysis, concentrating on a band around the O VII triplet (≈570 eV); the detected photons are given in Table 2. Since the

Table 1. *XMM* and *Chandra* observation log of 51 Peg.

Instrument	Configuration	ObsID	Obs. time	GTI (s)
XMM MOS1	full frame/thick filter	0551020901	2008-06-01 11:57:03 2008-06-02 03:17:50	55000
XMM MOS2	full frame/thick filter	0551020901	2008-06-01 11:57:03 2008-06-02 03:17:55	55100
XMM PN	full frame/thick filter	0551020901	2008-06-01 13:09:38 2008-06-02 03:18:10	29000
Chandra ACIS-S	back-illuminated	10825	2008-12-06 11:03:26 2008-12-06 12:26:26	4980
Chandra HRC-I	imaging	10826	2008-12-06 12:44:54 2008-12-06 14:07:54	4924

Table 2. Photons of 51 Peg in *XMM* and *Chandra*; see text for details.

Energy	PN		MOS1+2		ACIS-S		HRC	
(keV)	s	b	s	b	s	b	s	b
0.15–0.2	...	...	...	...	$1^{+2.4}_{-0.4}$	0	...	...
0.2–0.45	$17^{+5.0}_{-3.0}$	9.1	$7^{+3.6}_{-1.6}$	4.9	$6^{+3.6}_{-1.6}$	0	...	...
0.45–0.65	$8^{+3.9}_{-1.9}$	3.5	$6^{+3.5}_{-1.5}$	3.2	0^{+2}_{-0}	0	...	...
0.65–2.0	$10^{+4.3}_{-1.5}$	10.4	$21^{+7.2}_{-0.8}$	23.2	0^{+2}_{-0}	0	...	...
0.15–2.0	...	...	...	....	...	...	$21^{+5.7}_{-3.7}$	0.6

EPIC detectors have energy resolutions of $FWHM \approx 100$ eV, we adopted this as minimum bandwidth.

In the source region we then count the number of photons recorded in the various energy bands and detectors, listed in column "s" in Table 2. Source counts are given with 1σ confidence limits for low count numbers according to Kraft et al. (1991); for a detailed discussion, see Ayres (2004). The scaled background counts (denoted "b") were taken from areas much larger than the source region, and thus the error on the background is dominated by statistical fluctuations.

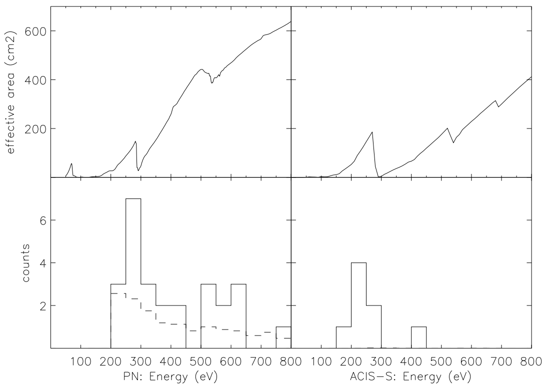

Fig. 1. *Upper panel*: effective areas of *XMM* PN and *Chandra* ACIS-S at energies below 800 eV. *Lower panel*: detect cell counts (solid histogram) of 51 Peg in PN and ACIS-S over the respective backgrounds (dashed; ACIS-S has practically no background).

2.2. Chandra data analysis

For data reduction of the *Chandra* observations we used CIAO 4.1 (Fruscione et al. 2006) and applied standard selection criteria. The analysis of the data was performed in the 0.15–1 keV energy band since the back-illuminated ACIS-S chip has nonzero effective area at X-ray energies below 300 eV. For the HRC imager no energy cuts were used since its energy resolution is low. 51 Peg is clearly detected in both instruments.

In the ACIS observation we detect eight photons in the source region, a circle with 1.5″ radius around 51 Peg's nominal position. This radius was chosen to contain 95% of the soft (≤1 keV) photons from a point-like source. From nearby source-free regions in the 150–650 eV energy band we expect only 0.03 background counts for this area, therefore we attribute all of the recorded counts to 51 Peg. The spectral resolution of ACIS-S is similar to the one of the EPIC detectors (≈100 eV).

In the HRC-I pointing 21 photons were detected in the source region over a background of 0.6 photons scaled to the same area. At any rate, also the HRC clearly detects 51 Peg.

3. Results

3.1. XMM-Newton PN and MOS

51 Peg shows a photon excess in the 0.2–0.45 keV and the O VII band (0.45–0.65 keV) in PN and a very weak excess in the same bands in the merged MOS detectors. The MOS and PN lightcurves show no obvious variability over the whole 55 ks. As shown in Fig. 1, most of PN's excess source photons have energies around 300 eV; another emission feature is present around 570 eV, the energy of the O VII triplet. Because of *XMM*'s moderate intrinsic energy resolution the nominal energies of the detected source photons cannot be regarded as exact values. From the absence of emission features at O VIII energies (≈650 eV) we can conclude that 51 Peg's corona has an average plasma temperature well below 3 MK.

3.2. Chandra ACIS-S and HRC-I

All the recorded counts have energies between 150 and 450 eV and are distributed quite evenly over the observation time, supporting a soft, basically constant X-ray source. Let us now inspect the energies of the ACIS-S photons in detail; the CIAO software assigns a nominal energy to each recorded photon (see Fig. 1). The eight source photons have energies of 170, 206, 211, 212, 256, 227, 291 and 428 eV; they are hence very soft and obviously none of these photons can be attributed to O VII or even O VIII emission. This supports our hypothesis of a very low plasma temperature evoked by the *XMM* data.

The ACIS-S detector is prone to optical contamination, so we have to check whether the extremely soft events could be induced by optical photons. The threshold for optical contamination in the ACIS-S detector is at $V \approx 7.8$ for stars with an effective temperature between 5000 and 6500 K; a star this bright would cause a bias level shift of one Analog-to-Digital-Unit (ADU) of 3.4 eV during the standard 3.2 s time frame for the central pixel of the source. 51 Peg's visual magnitude is 5.5, so we expect ca. 8 ADUs per time frame. Since the event threshold lies at 20 ADUs, optical contamination can be ruled out as explanation for the detected events.

Also in the HRC the recorded events are distributed evenly throughout the observation time. The intrinsic energy resolution of the HRC detector is low so that little information on the

Table 3. X-ray fluxes of 51 Peg with 1σ errors, calculated with WebPIMMS using a 1 MK thermal plasma model.

Instrument	Flux (0.1–1.0 keV) (erg s^{-1} cm^{-2})	$\log L_X$ (0.1–1.0 keV) (erg s^{-1})
XMM PN	$1.2^{+1.0}_{-0.5} \times 10^{-14}$	26.3–26.8
XMM MOS1+2	$1.1^{+1.4}_{-0.6} \times 10^{-14}$	26.1–26.8
Chandra ACIS-S	$1.7^{+0.9}_{-0.4} \times 10^{-14}$	26.5–26.8
Chandra HRC-I	$4.2^{+1.1}_{-0.7} \times 10^{-14}$	27.0–27.2
ROSAT PSPC	$2.1^{+0.3}_{-0.3} \times 10^{-14}$	26.7–26.8

spectral energy distribution can be derived; because the HRC-I observation was carried out immediately after the ACIS-S observation, we assume that the 21 detected HRC-I source photons have similar energies as the photons in the ACIS-S detector.

3.3. Determination of coronal temperature

To estimate the coronal temperature, we evaluate the temperature-dependent hardness ratios of several energy bands, viz. $HR_{\rm PN} = H_{\rm PN}/S_{\rm PN}$ with $H_{\rm PN}$ and $S_{\rm PN}$ covering 0.45–0.65 keV and 0.2–0.45 keV for PN; for ACIS-S, we use $HR_{\rm ACIS\,1} = H_{\rm ACIS\,1}/S_{\rm ACIS\,1}$ and $HR_{\rm ACIS\,2} = H_{\rm ACIS\,2}/S_{\rm ACIS\,2}$ with the energy bands $H_{\rm ACIS\,1}$: 0.25–0.45 keV, $S_{\rm ACIS\,1}$: 0.15–0.25 keV, $H_{\rm ACIS\,2}$: 0.45–0.65 keV and $S_{\rm ACIS\,2}$: 0.25–0.45 keV. The energy bands for ACIS-S were chosen to obtain quite an even distribution of source photons.

We derive the temperature-dependence of the hardness ratios with Xspec v12, using the instrument responses and effective areas as shown in Fig. 1 and simulating spectra for a one-temperature thermal plasma model with solar abundance in the temperature range between $\log T = 5.6$ and 6.6 (see Fig. 2). The possible plasma temperature of 51 Peg is then constrained by the observed hardness ratios for ACIS-S and PN. Assuming 1σ errors for low count numbers as defined in Table 2, we find that $HR_{\rm PN} = 0.6^{+1.1}_{-0.4}$, $HR_{\rm ACIS\,1} = 0.6^{+1.0}_{-0.4}$ and $HR_{\rm ACIS\,2} = 0^{+1}_{-0}$. The observed PN ratio yields the temperature limits $5.85 \leq \log T \leq 6.3$. The ACIS-S ratios yield a lower temperature limit from HR_2 and an upper limit from HR_3: $5.8 \leq \log T \leq 6.05$, so that the likely temperature range for 51 Peg's corona is $5.85 \leq \log T \leq 6.05$.

Since there are virtually no background photons in ACIS-S, we can use the energies of the eight recorded source photons to validate our temperature constraints by identifying the most likely emission lines of their origin. Strong emission at temperatures near 1 MK comes from the Si and S emission line complexes around 200 eV, some strong Si lines around ≈230 eV, the C V triplet around 300 eV and the N VI triplet around 426 eV. These emission lines match well with the observed photons, which can be considered as a rough plausibility check. So, both the temperature constraints from hardness ratios and the identification of possible emission line complexes point to a plasma temperature of $T \lesssim 1$ MK.

3.4. Comparison with ROSAT data

To investigate the long-term X-ray behavior of 51 Peg, we reanalyzed a 12.5 ks *ROSAT* PSPC observation from December 1992. Using the conversion factor $ecf = (5.30 \times HR_1 + 8.31) \times 10^{-12}$ erg count^{-1} cm^{-2} with HR_1 being the hardness ratio $HR_1 = (H-S)/(H+S)$ (S: 0.1–0.4 keV, H: 0.5–2.0 keV) (Schmitt 1997), the luminosity derived from the observed count rate of 7 cts/ks is $\log L_X = 26.75$ erg s^{-1}. The observation is split in two parts,

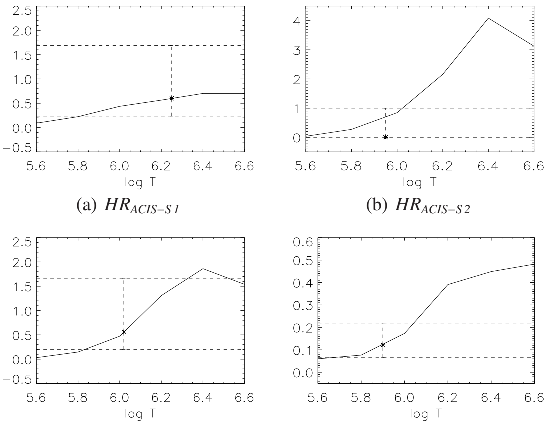

(a) $HR_{ACIS-S\,1}$ (b) $HR_{ACIS-S\,2}$ (c) HR_{PN} (d) HR_{PSPC}

Fig. 2. Hardness ratios as a function of temperature (see text for details). Observed ratios are given as crosses with 1σ error.

interrupted for ca. 70 ks. 51 Peg emits mainly soft X-ray photons below 500 eV ($HR_1 \approx -1.0$) and showed a low and constant X-ray activity level without any obvious variability.

We can constrain the coronal temperature of 51 Peg in this observation in the same way as for the *XMM* and *Chandra* pointings. We use the temperature-dependent hardness ratio $HR_{\rm PSPC} = H_{\rm PSPC}/S_{\rm PSPC}$ with the energy bands $H_{\rm PSPC}$: 0.1–0.3 keV, $S_{\rm PSPC}$: 0.3–0.65 keV. The observation yields $HR_{\rm PSPC} = 0.12^{+0.10}_{-0.06}$ from which lower and upper limits for the temperature can be derived, namely $5.65 \leq \log T \leq 6.05$ (see Fig. 2). This again leads to a temperatur estimate of $T \lesssim 1$ MK.

3.5. Consistency of measured count rates and fluxes

The observed count rates in *XMM* PN and MOS and *Chandra* ACIS-S are, considering the low photon numbers and therefore large statistical fluctuation, in reasonably good agreement. That ACIS-S detects no photons in the O VII band is no surprise given the shorter exposure in ACIS-S and its smaller effective area in that energy range (see Fig. 1). At energies below 300 eV, we find that the PN and MOS counts numbers are smaller than expected from what we see in ACIS-S. This might be explained by statistical fluctuations, errors in the effective area determination or energy redistribution effects in the CCD detectors (EPIC "low-energy shoulder"). Given these uncertainties for very low energies, we use only the O VII counts (0.45–0.65 keV) of PN and MOS for our flux calculations and then extrapolate the flux to a common energy range of 0.1–1 keV for comparison. For the other instruments, we use 0.65 keV as the upper bound of the energy range and their low-energy sensitivity limits as the lower bound (0.15 keV for ACIS-S/HRC, 0.1 keV for PSPC) and then extrapolate to the common energy range.

The fluxes normalized to the 0.1–1 keV energy band and the corresponding X-ray luminosities are consistent within 1σ errors except for the HRC-I flux, which seems to be larger (see Table 3). The count rate measured by the HRC instrument is higher by a factor of ca. 2.5 compared to the ACIS-S count rate. The nominal effective areas of the two instruments are very similar at low energies, with the HRC having somewhat larger

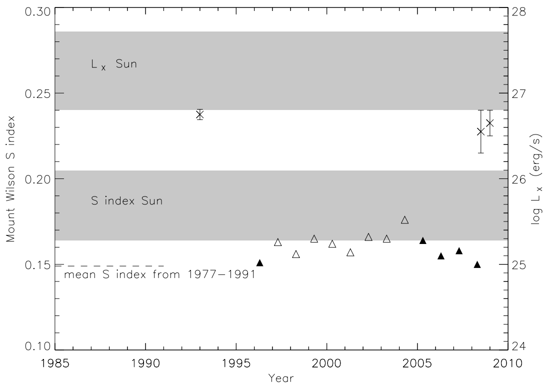

Fig. 3. X-ray luminosity (crosses) and S index seasonal mean of 51 Peg's Ca II H and K line flux; reliable Ca data given as filled triangles with typical standard deviations of $\lesssim \pm 0.005$, open triangles are less reliable values derived from only a small number of observations.

effective area below 200 eV ($\Delta A \approx 10$ cm^2 or 17% at 200 eV, 44% at 150 eV). The additional counts might arise from photons at these energies, but considering the small difference in effective areas, it does not seem likely that this is the case for all excess HRC photons. This mismatch is further validated by comparing ACIS-S and HRC count rates with WebPIMMS: assuming a thermal plasma with solar abundances and T = 1 MK, 8 counts in the 0.15–0.65 keV energy band in ACIS-S translate into 9 expected counts in the same energy band in HRC-I, which is obviously inconsistent with the 21 recorded HRC photons only 15 min after the ACIS-S observation. The photon count estimate changes by <20% if one assumes a plasma temperature of 0.8 or 1.25 MK, so a slightly different plasma temperature does not cure the substantial mismatch in the count rates.

Mismatches between HRC and *XMM* count rates have been reported before for α Cen (Robrade et al. 2005; Ayres et al. 2008). This mismatch between almost simultaneous HRC and ACIS-S count rates can be explained reasonably by two possibilities: either the effective area of the HRC at low energies is underestimated in the current calibration or the effective areas of *XMM* MOS and PN (while using the thick filter) as well as *Chandra* ACIS-S are overestimated in that energy range. A detailed cross-calibration effort, preferably with a soft coronal source, could help to resolve any systematic errors in the effective areas of the instruments.

4. Discussion

4.1. Low activity – 51 Peg a Maunder minimum candidate?

We found 51 Peg to be a rather constant, weak and soft X-ray source over the last 15 years. Another available long-term activity indicator is Ca II. In the Ca II H and K line flux monitoring programs carried out at the Mount Wilson and Lowell Observatories (Baliunas et al. 1995; Hall et al. 2007), 51 Peg was found to have a very low chromospheric activity level ($\langle R'_{\rm HK} \rangle = -5.01, S_{\rm MW} \approx 0.16$). In Fig. 3 we plot the star's Mount Wilson S index measured since 1996 together with the average of older data. Clearly, the overall chromospheric activity is low, with some variations in the older set of data which is also seen in the more recent observations. Apart from one data point which is derived from a very small number of observations, 51 Peg's S indices are at the lower end of or even below the Sun's respective data during a solar minimum (data taken from Baliunas et al. 1995). Other stellar properties like radius, mass, age and effective temperature are similar to the Sun's respective parameters.

The steady low-activity behavior of 51 Peg's Ca II H and K line fluxes is also reflected by its X-ray properties. Compared to estimates for the solar X-ray luminosity in the *ROSAT* RASS band (0.1–2.4 keV) during a solar cycle (Judge et al. 2003), 51 Peg's luminosity is also at the lower end of the Sun's values. The ratio of the star's X-ray to bolometric luminosity is also rather low with $L_{\rm X}/L_{\rm bol} = 1 \times 10^{-7}$. The X-ray surface flux of F to M stars was shown to be constrained at the lower end by the surface flux level of a solar coronal hole; $F_{\rm X\,(hole)} \approx 10^4$ erg s^{-1} cm^{-2} for the *ROSAT* and *Chandra* energy band, which translates to $\approx 10^{3.8}$ erg s^{-1} cm^{-2} for *XMM*'s 0.2–12 keV band (Schmitt 1997). 51 Peg's surface flux, calculated from the ACIS-S data, is one of the lowest so far detected with $F_{\rm X} = 10^{3.7}$ erg s^{-1} cm^{-2}; the coronal hole surface flux seems to be a good description of this star's X-ray flux, with regards to the flux level as well as the plasma temperature.

There has been some discussion on how to identify a Maunder minimum (MM) star over the last years. The original criterion of chromospheric activity levels $\langle R'_{\rm HK} \rangle < -5.1$ was derived by Henry et al. (1996), but relied on a stellar sample contaminated with evolved stars, which have significantly lower chromospheric activity levels compared to main sequence stars. Wright (2004) reanalyzed these data, excluding evolved stars with luminosities more than one magnitude larger than the *Hipparcos* average main sequence for the respective $B - V$ value, and found that most stars previously identified as MM candidates are evolved stars and therefore not comparable to the Sun's Maunder minimum state. This led Judge & Saar (2007) to the question if the minimum $\langle R'_{\rm HK} \rangle$ level for main sequence stars to qualify as an MM candidate should be higher than −5.1, and also to consider flat-activity time profiles and UV- and X-ray data to identify MM candidates. A recent study by Hall et al. (2009) suggests that minimum levels of $R'_{\rm HK}$ depend on stellar metallicity, with metal-poor stars from the examined sample having a higher minimal $R'_{\rm HK}$. In this picture, 51 Peg as a metal-rich star still has low chromospheric activity as measured by $R'_{\rm HK}$, but this alone does not necessarily qualify it to be a Maunder minimum candidate. However, as recent results show (Hall et al. 2007, 2009), the absolute magnetic excess flux $\Delta\mathcal{F}_{\rm HK}$ seems to be a more reliable indicator for stellar activity than $R'_{\rm HK}$. In terms of this quantity, 51 Peg's activity level is even lower compared to the quiescent Sun than indicated by $R'_{\rm HK}$ or the S index, supporting our interpretation of 51 Peg as being extremely inactive.

The strongest line of evidence for 51 Peg being a Maunder minimum candidate is its flat activity profile as seen over decades in the Mount Wilson program (Baliunas et al. 1995) and in observations at Lowell Observatory (Hall et al. 2007), as well as the extremely low X-ray surface fluxes, which have not changed significantly since the 1992 *ROSAT* observations. That 51 Peg is a slow rotator with $P_\star \approx 30$–40 d (Baliunas et al. 1996; Mayor & Queloz 1995) fits the picture, making 51 Peg the first MM candidate star with a close-in giant planet.

A statistical analysis of the X-ray luminosities of planet-bearing host stars has recently been conducted (Kashyap et al. 2008). Its authors claim that stars with close-in giant planets, such as 51 Peg, are on average X-ray brighter by a factor of two compared to stars with far away planets. Apparently, 51 Peg's overall activity is not enhanced by the presence of its Hot Jupiter. However, at a distance of order of 50 $R_{\rm Jup}$ only a weak interaction between an inactive star and its planet might be expected.

5. Conclusions

We have detected X-ray emission from 51 Peg in a 55 ks observation with *XMM-Newton* and 5 ks observations with *Chandra* ACIS-S and HRC-I each. The detection of 51 Peg with a low count rate in the *XMM* pointing and the clear source signal in the much shorter *Chandra* observations can be explained by the different effective response of the detectors at low energies and 51 Peg having an extremely cool corona. Our main results are summarized as follows:

1. 51 Peg shows weak emission in the O VII triplet and emission around 200 eV which can be explained most likely by cool silicon emission lines.
2. A coronal temperature of $\lesssim$1 MK is consistent with the detected hardness ratios in different energy bands in both the *XMM* and the *Chandra* pointing as well as in the *ROSAT* observation carried out 16 years earlier.
3. The *Chandra* HRC-I count rate is higher than can be explained by differences in the effective areas of HRC and ACIS-S; HRC's effective area might be larger at low energies than given in the calibration so far.
4. The constant and very low surface X-ray flux level together with a flat-activity behavior in chromospheric Ca II H and K line fluxes suggests 51 Peg to be a Hot Jupiter-bearing Maunder minimum candidate.

Acknowledgements. K.P. and J.R. acknowledge financial support from DLR grants 50OR0703 and 50QR0803. J.C.H. acknowledges support from grant ATM-0742144 from the National Science Foundation. This work is based on observations obtained with *XMM-Newton*, *Chandra* and makes use of the *ROSAT* Data Archive. We acknowledge the allocation of *Chandra* Director's Discretionary Time.

References

Ayres, T. R. 2004, ApJ, 608, 957
Ayres, T. R., Judge, P. G., Saar, S. H., & Schmitt, J. H. M. M. 2008, ApJ, 678, L121
Baines, E. K., McAlister, H. A., ten Brummelaar, T. A., et al. 2008, ApJ, 680, 728
Baliunas, S. L., Donahue, R. A., Soon, W. H., et al. 1995, ApJ, 438, 269
Baliunas, S., Sokoloff, D., & Soon, W. 1996, ApJ, 457, L99
Fruscione, A., McDowell, J. C., Allen, G. E., et al. 2006, in SPIE Conf. Ser., 6270
Fuhrmann, K., Pfeiffer, M. J., & Bernkopf, J. 1997, A&A, 326, 1081
Gonzalez, G. 1997, MNRAS, 285, 403
Hall, J. C., Lockwood, G. W., & Skiff, B. A. 2007, AJ, 133, 862
Hall, J. C., Henry, G. W., Lockwood, G. W., Skiff, B. A., & Saar, S. H. 2009, AJ, 138, 312
Henry, T. J., Soderblom, D. R., Donahue, R. A., & Baliunas, S. L. 1996, AJ, 111, 439
Judge, P. G., & Saar, S. H. 2007, ApJ, 663, 643
Judge, P. G., Solomon, S. C., & Ayres, T. R. 2003, ApJ, 593, 534
Kashyap, V. L., Drake, J. J., & Saar, S. H. 2008, ApJ, 687, 1339
Kraft, R. P., Burrows, D. N., & Nousek, J. A. 1991, ApJ, 374, 344
Mayor, M., & Queloz, D. 1995, Nature, 378, 355
Robrade, J., Schmitt, J. H. M. M., & Favata, F. 2005, A&A, 442, 315
Santos, N. C., Israelian, G., & Mayor, M. 2001, A&A, 373, 1019
Schmitt, J. H. M. M. 1997, A&A, 318, 215
Valenti, J. A., & Fischer, D. A. 2005, ApJS, 159, 141
Wright, J. T. 2004, AJ, 128, 1273

Chapter 5

Coronal properties of planet-bearing stars

K. Poppenhaeger, J. Robrade and J. H. M. M Schmitt
Astronomy & Astrophysics, Volume 515, id.A98 (2010) [1]
The original publication is available at www.aanda.org

[1] Due to some incorrectly printed data entries in two tables, a *Corrigendum* was accepted for publication by A&A and is included here.

A&A 515, A98 (2010)
DOI: 10.1051/0004-6361/201014245

Astronomy & Astrophysics

Coronal properties of planet-bearing stars

K. Poppenhaeger, J. Robrade, and J. H. M. M. Schmitt

Hamburger Sternwarte, University Hamburg, Gojenbergsweg 112, 21029 Hamburg, Germany
e-mail: katja.poppenhaeger@hs.uni-hamburg.de

Received 11 February 2010 / Accepted 20 March 2010

ABSTRACT

Context. Do extrasolar planets affect the activity of their host stars? Indications for chromospheric activity enhancement have been found for a handful of targets, but in the X-ray regime, conclusive observational evidence is still missing.

Aims. We want to establish a sound observational basis to confirm or reject major effects of Star-Planet Interactions (SPI) in stellar X-ray emissions.

Methods. We therefore conduct a statistical analysis of stellar X-ray activity of all known planet-bearing stars within 30 pc distance for dependencies on planetary parameters such as mass and semimajor axis.

Results. In our sample, there are no significant correlations of X-ray luminosity or the activity indicator L_X/L_{bol} with planetary parameters which cannot be explained by selection effects.

Conclusions. Coronal SPI seems to be a phenomenon which might only manifest itself as a strong effect for a few individual targets, but not to have a major effect on planet-bearing stars in general.

Key words. planet-star interactions – stars: activity – stars: coronae – stars: statistics – X-rays: stars

1. Introduction

The detection of extrasolar planets is one of the outstanding achievements in astronomy during the last 20 years. The first detected exoplanet revealed properties which were very surprising at that time: *51 Peg* (Mayor & Queloz 1995) hosts a Jupiter-like planet at a distance of only 0.05 AU, thus the planet orbits its host star in less than five days. Since then, more than 400 other exoplanets have been found at the time of writing (see for example the Exoplanet Database at www.exoplanet.eu), both in very close orbits and in such more familiar from our own Solar system.

With the existence of extrasolar planets established, the question arises what the environmental properties of such planets may be and if they might even allow the existence of life. The physical properties of planets, especially in close orbits, are crucially determined by the irradiation from their host stars. The evaporation rate of a planetary atmosphere depends on its exospheric temperature T_∞, i.e., the regions where particles can escape freely (Lammer et al. 2003). Thus, the host star's EUV and X-ray radiation is the key property determining a planets exospheric temperature. Evaporation of the planetary atmosphere has been observed for the transiting planet *HD 209458b* (Vidal-Madjar et al. 2003): the planet loses hydrogen which is observable in absorption spectra during the transit.

At very close distances, one might expect also planets to influence their host stars, in analogy to binary stars which show a higher activity level compared to single stars. Two different processes for Star-Planet-Interaction (SPI) have been put forward (Cuntz et al. 2000). Planets can induce tidal bulges on the star with an interaction strength depending on the planetary semimajor axis ($\propto a_{pl}^{-3}$), which might lead to enhanced coronal activity via increased turbulence in the photosphere. Planetary magnetic fields can also interact with the stellar magnetic field ($\propto a_{pl}^{-2}$) and might also induce enhanced activity via Jupiter-Io-like interaction, i.e. flux tubes which connect star and planet and heat up their footpoints on the stellar surface, or magnetic reconnection. Some observational campaigns have been conducted to investigate the existence of possible SPI: Shkolnik et al. (2005) monitored the chromospheric activity of 13 stars via Ca II H and K line fluxes and found indications for cyclic activity enhancements in phase with the planetary orbit for two of these stars. The activity enhancements appeared once per planetary orbit, suggesting magnetic instead of tidal interaction. However, measurements obtained three years later (Shkolnik et al. 2008) showed that the activity enhancements had switched to a cycle in phase with the stellar rotation period instead.

The *coronal* activity of planet-bearing stars has been investigated in a first systematic study by Kashyap et al. (2008). The authors claim an over-activity of planet-bearing stars of a factor of four compared to stars without planets, but their study had to include upper limits for a large number of stars since less than one third of the stars in their original sample were detected in X-rays at that time. A dedicated campaign to search for magnetic SPI in the case of *HD 179949*, one of the stars which Shkolnik et al. (2005) found to have cyclic activity changes in the chromosphere, was conducted by Saar et al. (2008). These authors found spectral and temporal variability phased with the planetary orbit, but some of that might also be induced by intrinsic stellar activity variations, since the stellar rotation period is poorly known ($P_* = 7–10$ d).

Up to now, the observational basis of stellar coronal activity enhancements due to close-in planets is not sound enough to establish or reject the possibility of coronal SPI. In order to adress this issue we conducted an X-ray study of all planet-hosting stars within a distance of 30 pc with XMM-Newton which have not been studied with ROSAT before. In this fashion a volume-limited complete stellar sample can be constructed.

2. Observations and data analysis

As of December 1st 2009, a total of 72 stars within 30 pc distance have been detected which are known to to harbor one or more planets. For some of these, X-ray properties are known from previous ROSAT or XMM-Newton observations, but for a large number of these stars X-ray characteristics were not or only poorly known. Therefore we observed a total of 20 planet-hosting stars with XMM-Newton between May 2008 and April 2009 to determine X-ray luminosities for stars which had not been detected before in other X-ray missions, and to derive coronal properties from spectra recorded with EPIC (both MOS and PN CCD detectors) especially for stars with close-in planets. We reduced the data with SAS version 8.0, using standard criteria for filtering the data. We extracted counts from the expected source regions with radii between 10″ and 30″, depending on the source signal, background conditions and the presence of other nearby sources. Background counts were extracted from much larger, source-free areas on the same chip for the MOS detectors and at comparable distances from the horizontal chip axis for the PN detector.

For hitherto undetected stars, which showed only a weak source signal in our observations, we used the source detection package "edetect-chain" of SAS v8.0. As stars with low X-ray luminosities in general have lower coronal temperatures and thus softer spectra, we used energy bands of 0.2–1 keV in PN and 0.15–1 keV in MOS and merged all EPIC detectors for source detection.

For the subsequent analysis of all stars we use the four energy bands 0.2–0.45 keV, 0.45–0.75 keV, 0.75–2 keV and 2–5 keV, because not all of our sample stars were detected with sufficient signal to noise ratio to allow spectral fitting. With the four energy bands, we can calculate the stellar fluxes via ECFs (energy conversion factors) for each band more accurately than by just assuming a single ECF for all counts. Above 5 keV, there is very little to no signal present in comparison to softer energies for all of our stars. We calculated these ECFs by simulating spectra in Xspec v12.5 for different coronal temperatures with the respective instrumental responses and effective areas of the detectors folded in. This yields reliable ECFs which vary about 25% for coronal temperatures above 1 MK for thin and medium filters. For the thick filter, the small effective area below 350 eV introduces larger errors in the ECFs already for temperatures below $\log T[K] = 6.2$.

For the error estimate on our derived luminosities, we use Poissonian errors on the total number of source counts, and an additional error of 30% to account for uncertainties in the ECFs and stellar variability. For stars which were not observed with XMM-Newton, we use the published X-ray luminosities from Kashyap et al. (2008) and add an extra error of 40% on top of their Poissonian errors, since Kashyap et al. (2008) used a single ECF for their flux calculations.

When comparing X-ray luminosities derived from XMM-Newton and ROSAT observations, one has to take into account the different energy bands accessible to the detectors (0.2–12 keV for XMM-Newton, 0.1–2.4 keV for ROSAT). For coronal temperatures between $\log T = 6.2$ and 7.0, the flux in the ROSAT band is larger by a factor of 1.1 compared to the XMM-Newton band. For lower coronal temperatures between $\log T = 6.0$–6.2 and $\log T = 5.8$–6.0, the flux in the ROSAT band is larger by a factor of ≈1.5 and ≈4.0, respectively, rising steeply towards even lower temperatures, since the spectrum shifts to energies which are inaccessible to XMM-Newton. With these factors, we can transform the XMM-Newton fluxes to the ROSAT band, identifying stars with coronal temperatures below $\log T = 6.2$ and 6.0 by a hardness ratio of $HR = (H - S)/(H + S) < +0.19$ and -0.34 respectively, with H and S being the source counts in the energy bands 450–750 eV and 200–450 eV, respectively.

We did not exclude flaring periods of individual stars when doing comparisons of X-ray luminosities or activity indicators, since we cannot identify flares in stars which are barely detectable and do not allow lightcurve analysis. We do, however, distinguish between flaring and quiescent phases for spectral analyses of individual stars.

When conducting intra-sample comparisons, we will use only detections for Kolmogorov-Smirnov and correlation tests, but we will include upper limits when doing linear regressions of X-ray luminosities or activity indicators over planetary properties.

3. Sample properties

Now we characterize our sample of planet-bearing stars within 30 pc with respect to X-ray detection rates and X-ray surface fluxes of ROSAT- and XMM-Newton-detected stars as well as in comparison with field stars. Tables 4 and 5 list stellar and planetary parameters as well as X-ray properties of the sample stars which have been detected with XMM-Newton and ROSAT, respectively.

3.1. X-ray detection rate

In total, 72 stars planet-bearing stars have been detected within a distance of 30 pc. 36 of these were observed with XMM-Newton over the last years, yielding 32 X-ray detections. For 24 additional stars, which have not been observed with XMM-Newton, X-ray luminosities are known from ROSAT observations. This yields 56 stars with known L_X out of the total sample of 72 stars. In our further sample analysis, we will leave three detected stars out of our analysis, namely γ Cep, Fomalhaut and β Pic; the former being a spectroscopic binary which cannot be resolved in X-rays, the two latter being A-type stars for which the production process of X-ray emission is supposedly very different from later-type stars with a corona and therefore also any planetary influence on X-ray properties should be determined by a different mechanism compared to stars of spectral type F and later.

The stars within 30 pc around which planets have been detected are mainly of spectral type G or later. Figure 1 gives the rate of X-ray detections versus spectral type, being 75% for F stars, >65% for G stars and >85% for K and M stars.

3.2. X-ray surface flux

For a subsample of our stars excluding giants, we examined the X-ray surface flux. The lowest flux level of XMM-Newton-detected stars seems to be systematically lower than for ROSAT-detected stars. This is not surprising, since both X-ray telescopes have different accessible energy bands (0.2–12.0 keV for XMM-Newton, 0.1–2.4 keV for ROSAT) and the integrated X-ray flux depends strongly on the lower energy cutoff especially for cool coronae as in our stars.

Gauged to the same energy band (as described in Sect. 2), both XMM-Newton- and ROSAT-detected stars show a limiting X-ray surface flux level near $\log F_{\rm surf}\,[{\rm erg\,s^{-1}\,cm^{-2}}] \gtrsim 4.0$ (see Fig. 2). For the calculation of $F_{\rm surf}$, we use the stellar radii given in the exoplanet.eu database. If we compare

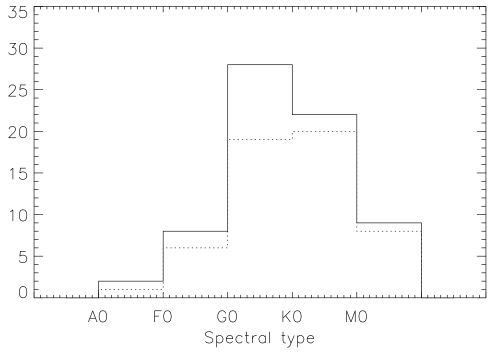

Fig. 1. Spectral types of planet-bearing stars within 30 pc (solid); X-ray detections marked as dotted lines.

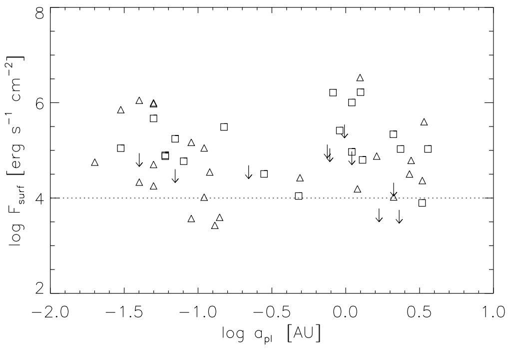

Fig. 2. X-ray surface flux of planet-bearing stars vs. planetary distance. XMM-Newton fluxes are shown as triangles, ROSAT fluxes as squares. XMM-Newton fluxes scaled to the ROSAT energy band; the flux level of a solar coronal hole ($\log F_{\rm surf} \approx 4$) is indicated by the dotted line.

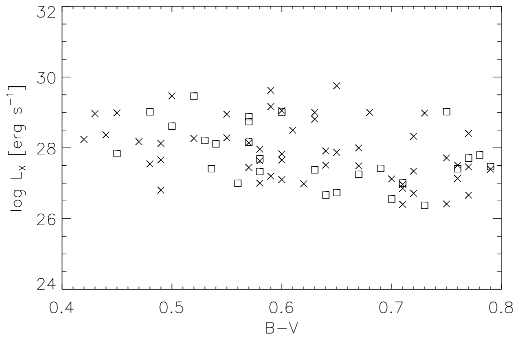

Fig. 3. X-ray luminosity of F and G type stars. Planet-bearing stars: squares, stars without planets: crosses.

Table 1. Correlation of X-ray luminosity and $L_{\rm X}/L_{\rm bol}$ with planetary parameters; X/R: XMM-Newton/ROSAT detections.

Parameters	Data set	Spearman's ρ	Probability p
$L_{\rm X}$ with $a_{\rm pl}$	X	–0.05	0.81
	X + R	–0.02	0.91
$L_{\rm X}/L_{\rm bol}$ with $a_{\rm pl}$	X	–0.12	0.54
	X + R	–0.11	0.43
$L_{\rm X}$ with $M_{\rm pl}$	X	0.11	0.55
	X + R	0.22	0.13
$L_{\rm X}/L_{\rm bol}$ with $M_{\rm pl}$	X	0.18	0.37
	X + R	–0.02	0.88
$L_{\rm X}$ with $a_{\rm pl}^{-1} \times M_{\rm pl}$	X	0.21	0.25
	X + R	0.31	0.03
$L_{\rm X}/L_{\rm bol}$ with $a_{\rm pl}^{-1} \times M_{\rm pl}$	X	0.33	0.08
	X + R	0.09	0.51

the XMM-Newton and ROSAT surface flux sample with the Kolmogorov-Smirnov test, we find that both populations are significantly different. This is due to the selection effect that we proposed planet-bearing stars which were previously undetected with ROSAT (and therefore have low X-ray luminosities) for detection pointings with XMM-Newton. This leads to a higher concentration of stars near the limiting surface flux level of $\log F_{\rm surf}$ [erg s^{-1} cm^{-2}] $\approx$ 4. For the XMM-Newton and ROSAT subsamples of stars with a surface flux above $\log F_{\rm surf}$ [erg s^{-1} cm^{-2}] $\geq$ 4.5, we find that these populations are statistically indistinguishable (probability for both samples stemming from the same distribution 71%).

3.3. Comparison with field stars

To check for systematic differences, we compare our sample of planet-bearing stars with a sample of field stars of spectral type F and G as available from Schmitt (1997) from ROSAT observations. In Fig. 3 we show the X-ray luminosities of these stars over $B-V$ of both the planet-bearing and non-planet-bearing sample. A Kolmogorov-Smirnov test yields that the probability that both samples are drawn from the same parent distribution is 74%. The values of the activity indicator $L_{\rm X}/L_{\rm bol}$ yield a probability of 23% to be from the same distribution; this can be explained by the fact that stars of low activity are generally chosen for planet search programs.

4. Star-planet interactions

Now we investigate our sample in detail for possible correlations of X-ray properties with planetary parameters.

One expects that possible effects which giant planets might have on their host stars will strongly increase with decreasing orbital distance. Also, tidal as well as magnetic intercations should increase with the exoplanet's mass, assuming that larger exoplanets are capable of producing a stronger planetary magnetic field. Note that closer-in planets may rotate more slowly since they synchronize with their orbit, weakening their ability to generate magnetic fields (Grießmeier et al. 2004); however, the details of planetary dynamos are not fully understood.

The most interesting quantity with regards to SPI in the X-ray regime is the activity indicator $L_{\rm X}/L_{\rm bol}$. The X-ray luminosity alone varies with stellar radius independently of the activity level, but $L_{\rm X}/L_{\rm bol}$ is independent of such radius-induced effects. Any planet-induced activity changes should therefore be evident in $L_{\rm X}/L_{\rm bol}$; a planet-induced variation in $L_{\rm X}$ which would leave the ratio unchanged is rather unphysical, since $L_{\rm X}/L_{\rm bol}$ has typical values of 10^{-6} for our stars. A change in $L_{\rm bol}$ would therefore need 10^6 times more energy than the X-ray variation alone.

We study both the X-ray luminosity $L_{\rm X}$ as well as the activity indicator $L_{\rm X}/L_{\rm bol}$ for correlations with the innermost planet's semimajor axis and mass. In Table 1 we give

Spearman's ρ rank correlation coefficient for various combinations. A value of 1 (−1) means a perfect correlation (anticorrelation), 0 means no correlation. The corresponding p-value gives the probability that the observed value of ρ can be obtained by statistical fluctuations.

For the correlation analysis of L_X/L_{bol}, we exclude giants from our sample (HD 27442 and HD 62509), since they have very low L_X/L_{bol} values due to their optical brightness. As well as for XMM-Newton detections alone as for XMM-Newton and ROSAT detection combined, we find no correlation of the semi-major axis with the stellar X-ray luminosity.

We find two possible correlations here: one of planetary mass with L_X and a stronger one for $a_{pl}^{-1} \times M_{pl}$ with L_X. Stars with giant and close-in planets have higher X-ray luminosities than stars with small far-out planets. For L_X/L_{bol}. there is a correlation with $a_{pl}^{-1} \times M_{pl}$ present in the sample of XMM-Newton detections, but not in the larger sample of ROSAT and XMM-Newton detections, pointing towards the possibility that this correlation might be a statistical fluctuation. The probable reason for strong correlations in L_X, but weaker or absent ones in L_X/L_{bol} is that there is also a strong (>2σ) correlation between M_{pl} and L_{bol}: stars with larger L_{bol} are more massive, and around massive stars, giant planets are detected much more easily compared to small ones. Both correlations of planetary mass with L_X and also L_{bol} seem to cancel out in L_X/L_{bol}.

Another significant correlation worth mentioning exists between the planetary mass and the spectral type of the host star: small planets are prone to be found around stars of later types. This is basically the same trend we see between M_{pl} and L_{bol}, since small planets are more easily detected around low-mass and therefore late-type stars.

To visualize these (non-)correlations, we perform linear regressions of $\log L_X$ and $\log(L_X/L_{bol})$ with either $\log a_{pl}$ or $\log(a_{pl}^{-1} \times M_{pl})$ by using the "linmix_err" routine implemented in IDL. As already seen in the correlation analysis, we obtain slopes which are compatible with zero at 1σ level for all of the pictured cases except for $\log L_X$ over $\log(a_{pl}^{-1} \times M_{pl})$ (see Fig. 5).

Independently of any linear trend, we can test if the L_X values of stars with close-in and far-out planets stem from the same distribution. Figure 4 shows the logarithmic X-ray luminosities of stars with planets within $a_{pl} \leq 0.2$ AU and stars with planets beyond $a_{pl} \geq 0.5$ AU. The means of both distributions are very similar and not distinguishable at 1σ level: $\langle \log L_{X\,\mathrm{close-in}} \rangle = 27.52 \pm 0.72$ erg s^{-1} and $\langle \log L_{X\,\mathrm{far-out}} \rangle = 27.70 \pm 0.80$ erg s^{-1}. A Kolmogorov-Smirnov test yields a probability of 84% for both samples being from the same distribution. However, the comparison of stars with *close-in, heavy* planets compared to *far-out light* ones yields that the probability for both samples to have the same parent distribution is very small with <1%; the average X-ray luminosity is higher for stars with close-in, heavy planets with $\langle \log L_{X\,\mathrm{close-in\,heavy}} \rangle = 27.91 \pm 0.76$ erg s^{-1} compared to $\langle \log L_{X\,\mathrm{far-out\,light}} \rangle = 27.41 \pm 0.73$ erg s^{-1}, but the means are compatible within 1σ errors.

5. Properties of individual targets

In the following, we give a short overview on our newly observed stars and their spectral properties. The stellar, planetary and X-ray properties of all planet-bearing stars which were observed with XMM-Newton are listed in Table 4.

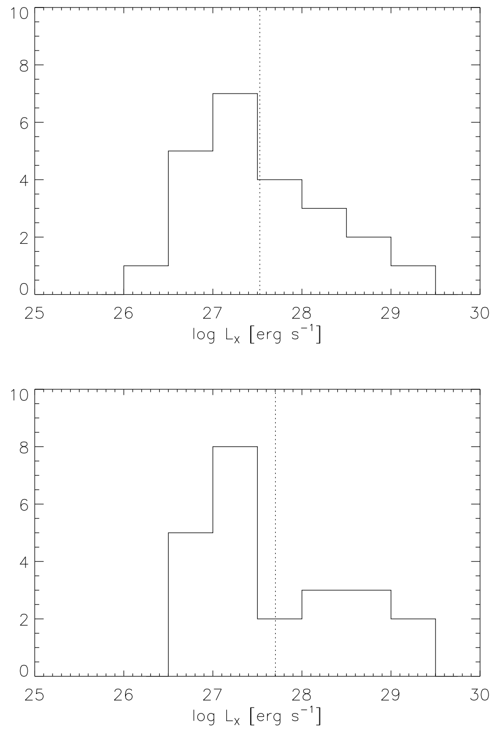

Fig. 4. Histograms of X-ray luminosities for X-ray detected stars within 30 pc with close-in ($a_{pl} \leq 0.2$ AU, *upper panel*) and far-out ($a_{pl} \geq 0.5$ AU, *lower panel*) planets. Mean $\log L_X$ values are indicated by dotted lines for both samples.

5.1. Individual targets

Between May 2008 and April 2009 we observed a total of 20 planet-bearing stars in X-rays. One of these stars, *SCR 1845*, turned out to harbor a brown dwarf and not a planet; the X-ray characteristics of *SCR 1845* are discussed in a separate publication (Robrade et al. 2010). The X-ray properties of the remaining 19 stars are described briefly now.

GJ 674, *GL 86*, *GL 876*, *HD 102195*, *GJ 317*, *55 Cnc* and *HD 99492* yielded sufficient signal-to-noise ratio for spectral fitting of the obtained EPIC spectra. They are all characterized by coronae with cool to moderate temperatures (details listed in Sect. 5.2). *GJ 674* shows one large and several smaller flares on timescales of ca. 5 ks. Also *GL 876* shows several short flares. The other stars show some variability around 15–25% level. As an example, we show the EPIC spectrum and the corresponding two-temperature fit of *GL 86* in Fig. 6.

HD 154345, *HD 160691*, *HD 4308*, *HD 52265*, *HD 93083*, *51 Peg*, *HD 27442*, *HD 114386* and *HD 114783* were detected in our exposures, but did not yield enough photons for spectral fitting. Where meaningful hardness ratios could be calculated from the numbers of counts, the stars proved to be soft X-ray sources, as one expects for nearby stars with low X-ray luminosities. Two of these targets show interesting characteristics:

HD 99492 is part of a binary system, consisting of a K2 dwarf, which is the planet-bearing star *HD 99492*, and a K0 subgiant, *HD 99491*. Previously, *HD 99492* was assigned an

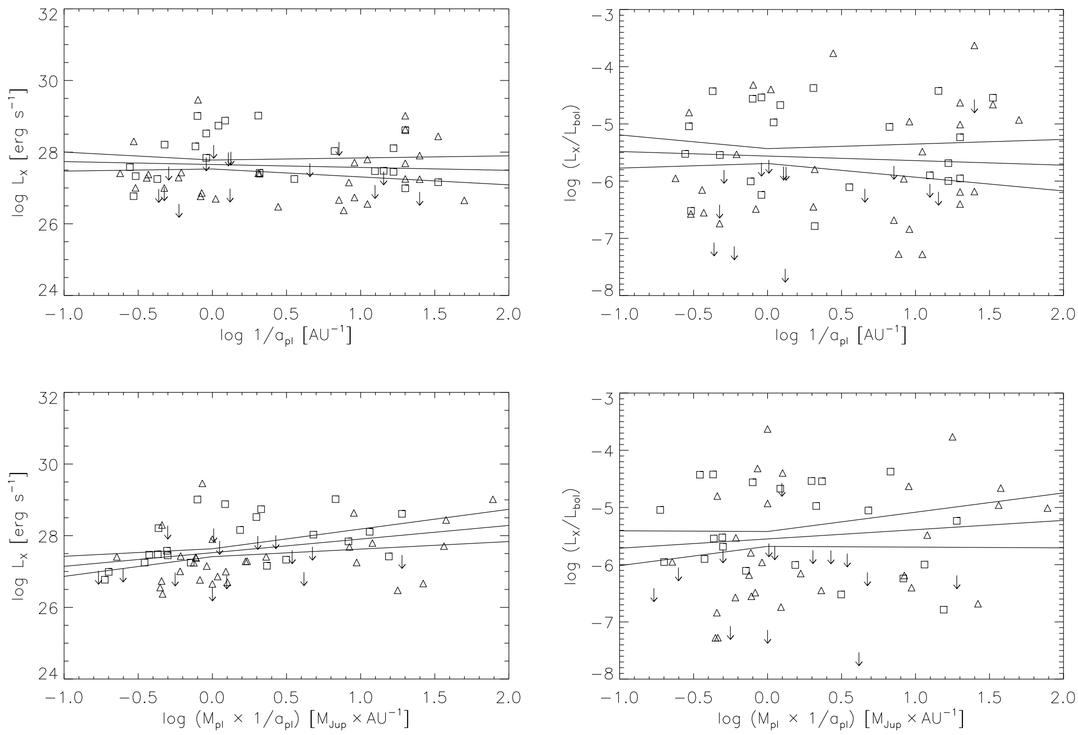

Fig. 5. X-ray luminosity and activity indicator $\log(L_X/L_{bol})$ as a function of $\log a_{pl}$ and $\log(a_{pl}^{-1} \times M_{pl})$, respectively. XMM-Newton detections: triangles, ROSAT detections: squares.

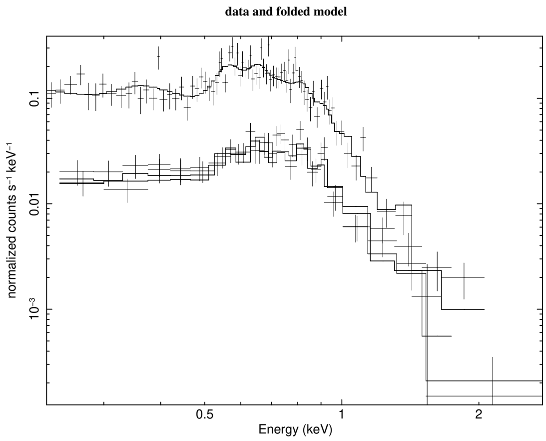

Fig. 6. Typical EPIC spectra (*upper*: PN, *lower*: MOS) of a planet-bearing star; here shown: *GL 86*.

X-ray luminosity of 27.56 erg s^{-1} (Kashyap et al. 2008), since the double system was unresolved in the corresponding ROSAT pointing. Our XMM-Newton pointing shows that *HD 99492* is actually the X-ray fainter part of the pair with an X-ray luminosity of only 26.93 erg s^{-1}.

51 Peg is, despite a moderate X-ray luminosity of 26.8 erg s^{-1} which it exhibited in a ROSAT pointing from 1992, barely detected in a deep XMM-Newton observation. The XMM-Newton source photons are extremely soft, which explains its better visibility in ROSAT and additional recent Chandra data, since these instruments have a larger effective area at very low X-ray energies. Detailed analysis (Poppenhäger et al. 2009) showed that the star is possibly in a Maunder minimum state.

The stars *16 Cyg B*, *HD 111232*, *HD 217107* and *HD 164922* could not be detected in X-rays in our exposures. The upper limits for these stars were calculated for a confidence level of 99%, following the lines of Ayres (2004) and point also towards low activity levels for these targets.

5.2. Spectral properties

Seven of the stars we observed yielded sufficient signal to noise ratio for spectral fitting of their XMM-Newton EPIC data. The spectra of six stars can be adequately described by a thermal plasma with two temperature components and solar abundances; the spectral fitting was performed with Xspec v12.5 and *apec* models. The derived spectral properties are listed in Table 2. They are mostly dominated by very cool plasma ($T \approx 1$ MK) with small contributions from hotter plasma, only *HD 102195* and *GL 86* have stronger contributions from a hotter component around 4–5 MK.

A&A 515, A98 (2010)

Table 2. Spectral modeling results derived from EPIC data; emission measure given in units of 10^{50} cm^{-3}.

Parameter	GL 86	GL 876	HD 102195	GJ 317	55 Cnc	HD 99492
T_1 (keV)	0.11	0.07	0.09	0.11	0.09	0.09
EM_1	1.63	0.42	8.54	0.19	1.39	1.02
T_2 (keV)	0.33	0.39	0.45	0.50	0.48	0.39
EM_2	1.27	0.06	8.07	0.06	0.19	0.20
$\chi^2_{\rm red}$ (d.o.f.)	1.02 (120)	1.44 (85)	0.95 (152)	0.77 (22)	1.2 (11)	0.99 (8)
$\log L_{\rm X}$ (0.2–2.0 keV)	27.6	26.4	28.3	26.5	27.1	27.0

Table 3. Spectral modeling results for *GJ 674* derived from EPIC data; emission measure given in units of 10^{50} cm^{-3}.

Parameter	GJ 674 quiescence	GJ 674 flare
T_1 (keV)	0.14	0.32
EM_1	0.71	3.57
T_2 (keV)	0.40	0.81
EM_2	2.52	1.61
O	0.41 ± 0.07	0.38 ± 0.05
Ne	0.66 ± 0.13	0.38 ± 0.18
Mg	0.34 ± 0.14	0.51 ± 0.25
Fe	0.29 ± 0.05	0.37 ± 0.12
$\chi^2_{\rm red}$ (d.o.f.)	1.12 (204)	1.00 (197)
$\log L_{\rm X}$ (0.2–2.0 keV)	27.5	27.7

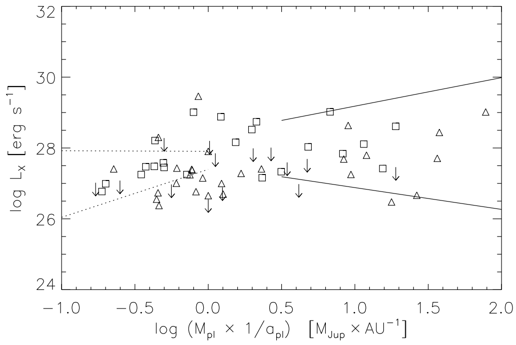

Fig. 7. Linear regression of $\log L_{\rm X}$ over $\log(a_{\rm pl}^{-1} \times M_{\rm pl})$ for close-in heavy planets (solid) and far-out light planets (dotted). Both regressions overlap at 1σ level.

The spectrum of *GJ 674* cannot be fitted satisfactorily when assuming solar abundances, therefore we fit its EPIC spectra with two-temperature *vapec* models. *GJ 674* exhibits a flare during our observation, so we conducted the spectral analysis for the time interval of the flare as well as for quiescent times. The results are given in Table 3. The temperature of both components rises considerably during the flare, as well as the total emission measure. Coronal abundances of the given elements are below solar values, consistent with the low photospherical iron abundance [Fe/H] = −0.28.

The X-ray luminosities derived from spectral modelling fit the ECF-derived results in Table 4 well, justifying our error estimate of ≈30%, which we assumed in addition to statistical errors.

6. Discussion

6.1. Interaction or selection?

In our data, we do not see any significant trend of the activity indicator $L_{\rm X}/L_{\rm bol}$ with the planetary semimajor axis, mass or a combination of both, in contrast to recent studies (Kashyap et al. 2008). The only significant trend, as shown in Sect. 4, is seen in the X-ray luminosity which is higher for stars with heavy close-in planets. Trying to explain this trend in $L_{\rm X}$ without an accompanying trend in $L_{\rm X}/L_{\rm bol}$ by SPI is problematic. The sample stars have typical $L_{\rm X}/L_{\rm bol}$ values of 10^{-6}. If planets induced higher $L_{\rm X}$ levels, but constant $L_{\rm X}/L_{\rm bol}$ ratios, the amount of energy introduced by SPI would have to be 10^6 times higher in $L_{\rm bol}$ than in $L_{\rm X}$. The $L_{\rm X}$ excess of stars with close-in heavy planets compared to stars with far-out light ones is of the order of 5×10^{27} erg s^{-1}. Thus, the energy excess in $L_{\rm bol}$ would have to be $\sim10^{33}$ erg s^{-1}. Comparing this to the typical orbital energy of a Hot Jupiter ($\sim10^{44}$ erg), this would lead to obviously unpyhsical timescales for the planet's orbital decay of only several thousand years.

However, there is also the possibility that the trend in $L_{\rm X}$ is caused by selection effects: all but three of the planets in our sample have been detected with the radial velocity (RV) method. Stellar activity can mask the RV signal. Since the RV signal is strongest for close-in, heavy planets, we have a selection effect which favors detection of such planets around active stars. The key question is, do the data show an *additional* trend of $L_{\rm X}$ with $a_{\rm pl}^{-1}$ and $M_{\rm pl}$ which is not induced by the selection effect and could be attributed to SPI?

To investigate this, we conduct two separate regression analyses on $\log L_{\rm X}$ over $\log(a_{\rm pl}^{-1} \times M_{\rm pl})$ for close-in heavy planets and far-out light planets, respectively. We define close-in heavy planets by $\log(a_{\rm pl}^{-1} \times M_{\rm pl}) > 0.5$ (corresponding to a Jupiter-like planet at a maximum orbital distance of ≈0.3 AU, for example) and far-out light planets by $\log(a_{\rm pl}^{-1} \times M_{\rm pl}) < 0$ (corresponding to a Jupiter-like planet at 1 AU or a Saturn-like planet at 0.3 AU). As shown in Fig. 7, both regressions overlap well at 1σ level, indicating that there is no additional activity enhancement effect measurable in this sample for close-in heavy planets other than the selection trend which also manifests itself in the subsample with far-out light planets.

6.2. Is there evidence for coronal SPI?

There are two different scenarios for SPI: tidal and magnetic interaction (see for example Cuntz et al. 2000). *Tidal interaction* will affect motions in the stellar convection zone as well as the flow of plasma in the outer atmospheric layers. If stellar rotation and the planetary orbital motion are not synchronous, tidal bulges should rise and subside on the star, causing additional turbulence at the footpoints of magnetic loops, leading to higher flaring rates, or causing outer layers of the star to corotate with

Table 4. Stellar and planetary parameters of planet-bearing stars within 30 pc, as observed by XMM-Newton.

Star	Type	Dist. (pc)	m_V	$B-V$	P_* (d)	[Fe/H]	$a_{\rm pl}$ (AU)	$M_{\rm pl}$ ($M_{\rm J}$)	GTI (s)	Net countrate[a] (cts/ks)	$F_{\rm X}$ (erg s^{-1} cm^{-2})	$\log L_{\rm X}$ 0.2–2 keV	$\log \frac{L_{\rm X}}{L_{\rm bol}}$
ϵ Eri	K2.0 V	3.2	3.73	0.88	11.2	–0.10	3.39	1.55	10385	5611.5 ± 23.3[b]	1.38E-11	28.22 ± 0.12	–4.88
GJ 674	M2.5	4.5	9.38	1.53	35.0	–0.28	0.04	0.04	15183	1102.6 ± 8.6	2.16E-12	27.73 ± 0.12	–3.80
GL 876	M4.0 V	4.7	10.17	1.67	41.0	–0.12	0.02	0.02	23436	48.9 ± 1.5	1.13E-13	26.48 ± 0.13	–5.11
VB 10	M8.0 V	5.8	9.91	0.00	–	0.00	0.36	6.40	10810	23.2 ± 1.5	4.91E-14	26.30 ± 0.14	–1.79
GJ 317	M3.5	9.2	12.00	1.53	–	–0.23	0.95	1.20	11245	14.3 ± 1.5	3.30E-14	26.52 ± 0.14	–4.57
HD 62509	G5.0 IV-V	10.3	1.15	1.00	130.0	0.19	1.69	2.90	28759	31.2 ± 1.1	1.01E-13	27.11 ± 0.13	–6.63
GL 86	K1.0 V	11.0	7.40	0.77	31.0	–0.24	0.11	4.01	13071	116.8 ± 3.1	2.94E-13	27.63 ± 0.12	–5.04
55 Cnc	G8.0 V	13.0	5.95	0.87	42.7	0.29	0.04	0.03	8505	18.6 ± 1.6	5.77E-14	27.07 ± 0.14	–6.36
47 UMa	G0.0 V	14.0	5.10	0.56	74.0	0.00	2.11	2.60	6196	2.6 ± 0.7	1.07E-14	26.40 ± 0.21	–7.34
51 Peg	G5.0 V	14.7	5.49	0.67	37.0	0.20	0.05	0.47	25299	0.4 ± 0.2	1.70E-15	26.28 ± 0.18	–7.37
τ Boo	M8.0 V	15.0	4.50	0.48	3.3	0.28	0.05	3.90	38251	1252.1 ± 5.7	3.21E-12	28.94 ± 0.12	–6.14
HD 160691	G3.0 IV-V	15.3	5.15	0.70	–	0.28	0.09	0.04	7046	3.6 ± 1.2	1.06E-14	26.47 ± 0.16	–7.36
HD 190360	G6.0 IV	15.9	5.71	0.73	–	0.24	0.13	0.06	2888	2.2 ± 1.4	5.23E-15	26.20 ± 0.21	–7.45
HD 99492	F7.0 V	18.0	7.57	1.01	45.0	0.36	0.12	0.11	19928	7.1 ± 0.6	2.44E-14	26.98 ± 0.15	–5.97
14 Her	K0.0 V	18.1	6.67	0.90	–	0.43	2.77	4.64	5532	14.6 ± 2.9	3.25E-14	27.11 ± 0.14	–6.33
HD 154345	G8.0 V	18.1	6.74	0.76	–	–0.11	4.19	0.95	3845	18.6 ± 2.4	5.46E-14	27.33 ± 0.16	–6.03
HD 27442	K2.0 III	18.1	4.44	1.08	–	0.20	1.18	1.28	4636	3.7 ± 1.3	1.23E-14	26.68 ± 0.18	–7.72
β Pic	A6.0 V	19.3	3.86	0.17	0.7	0.00	8.00	8.00	54896	0.2 ± 0.1[c]	6.00E-16	25.40 ± 0.15	–9.09
HD 189733	K1.5	19.3	7.67	0.93	13.4	–0.03	0.03	1.13	36271	110.3 ± 1.8	4.11E-13	28.26 ± 0.12	–4.84
HD 217107	G8.0 IV	19.7	6.18	0.72	37.0	0.37	0.07	1.33	5576	<6.0	<1.55E-14	<26.86	<–6.79
HD 195019	G3.0 IV-V	20.0	6.91	0.64	22.0	0.08	0.14	3.70	8333	2.8 ± 0.8	6.44E-15	26.49 ± 0.17	–6.86
16 Cyg B	G2.5 V	21.4	6.20	0.66	31.0	0.08	1.68	1.68	10768	<1.6	<5.42E-15	<26.47	<–7.22
HD 164922	K0.0 V	21.9	7.01	0.80	–	0.17	2.11	0.36	6955	<3.5	<1.21E-14	<26.84	<–6.59
HD 4308	G0.0 V	21.9	6.54	0.65	–	–0.31	0.11	0.05	7837	2.1 ± 0.7	7.89E-15	26.66 ± 0.19	–6.02
HD 114783	K0.0	22.0	7.57	0.93	–	0.33	1.20	0.99	3583	2.1 ± 1.5	6.72E-15	26.59 ± 0.19	–6.66
HD 216437	G4.0 IV-V	26.5	6.06	0.63	–	0.00	2.70	2.10	3329	8.2 ± 1.9	1.89E-14	27.20 ± 0.18	–6.73
HD 20367	G0.0	27.0	6.41	0.52	–	0.10	1.25	1.07	8861	1404.8 ± 12.6	2.76E-12	29.38 ± 0.12	–4.40
HD 114386	K3.0 V	28.0	8.80	0.90	–	0.00	1.62	0.99	3601	2.7 ± 1.2	7.19E-15	26.83 ± 0.21	–6.13
HD 52265	K0.0 III	28.0	6.30	0.54	–	0.11	0.49	1.13	6954	5.6 ± 1.0	1.82E-14	27.23 ± 0.17	–6.92
HD 75289	K3.0 V	28.9	6.35	0.58	16.0	0.29	0.05	0.42	6681	3.0 ± 0.7	1.21E-14	27.09 ± 0.20	–6.75
HD 93083	K2.0 V	28.9	8.33	0.94	48.0	0.15	0.48	0.37	7789	7.4 ± 1.3	1.67E-14	27.22 ± 0.16	–6.79
HD 102195	K0.0 V	29.0	8.06	0.83	12.0	0.05	0.05	0.45	13043	145.9 ± 3.4	2.87E-13	28.46 ± 0.12	–4.81
HD 111232	G8.0 V	29.0	7.61	0.68	30.7	–0.36	1.97	6.80	6996	<3.2	<9.72E-15	<26.99	<–6.41
HD 70642	G0.0 V	29.0	7.18	0.71	–	0.16	3.30	2.00	10935	3.0 ± 0.7	6.68E-15	26.83 ± 0.17	–8.08
HD 130322	K0.0 V	30.0	8.05	0.78	8.7	–0.02	0.09	1.08	4194	16.7 ± 2.2	3.87E-14	27.62 ± 0.16	–5.66

Notes. Stellar and planetary parameters taken from `www.exoplanet.eu`, bolometric luminosities calculated from m_V with bolometric corrections from Flower (1996).
[a] PN, 0.2–2 keV. [b] MOS1 countrate given, since PN detector suffered from pile-up for this observation. [c] Data taken from Hempel et al. (2005), combined MOS countrate given, since PN detector was optically contaminated.

the planet, which might enhance the stellar dynamo if $P_{\rm orb} > P_*$. *Magnetic interaction* is thought to be able to enhance the stellar activity in several ways: if planets are close enough to their host stars to be located inside the star's Alfvén radius, a Jupiter-Io-like interaction can form where the planet is connected with the star via fluxtubes which heat the stellar atmosphere at their footpoints. Alternatively, magnetic reconnection events of the stellar and planetary magnetic field lines might supply additional energy to the stellar atmosphere. Also the mere presence of the planetary magnetic field itself might affect stellar wind formation and coronal densities, as a recent study (Cohen et al. 2009) suggests.

Indications for SPI signatures in stellar *chromospheres* were found by Shkolnik et al. (2005) for two out of 13 stars, namely *HD 179949* and *υ And*, both stars with Hot Jupiters. The spectra of those stars showed periodic peaks in the Ca II H and K line emissions, common chromospheric activity indicators. The amplitude of the variation was 2.5% for *HD 179949* and 0.7% for *υ And* in the K line flux compared to a mean spectrum of the respective star and appeared once per orbital period of the planet in several years. However, the peaks changed to a once-per-stellar-rotation cycle in other years, suggesting an "On/Off"-behavior of chromospheric SPI. The fact that those peaks appeared only once per orbital period points towards magnetic SPI, since in a tidal SPI scenario one would expect two peaks in that time, which is not backed up by the Shkolnik data.

A first statistical study on possible X-ray flux enhancements due to Hot Jupiters has been conducted by Kashyap et al. (2008). They claim to have found strong evidence that stars with Hot Jupiters are on average more X-ray active than stars with distant planets. Their study uses main-sequence planet-bearing stars which were known at the time of writing, but the X-ray detection rate among these stars was only approximately one third, so that the authors had to include a large number of upper limits in their analysis and used Monte Carlo simulations on the X-ray luminosities of their sample. Their analysis suggests that stars with planets closer than 0.15 AU have on average four times higher X-ray luminosity than stars with planets at distances larger than 1.5 AU. They try to account for selection effects by regarding the trend of $L_{\rm X}/L_{\rm bol}$ with $a_{\rm pl}$ as selection-induced and the remaining

A&A 515, A98 (2010)

Table 5. Stellar and planetary parameters of planet-bearing stars within 30 pc, as observed by ROSAT.

Star	Type	Dist. (pc)	m_V	$B-V$	P_* (d)	[Fe/H]	a_{pl} (AU)	M_{pl} (M_J)	$\log L_X$ 0.1–2.4 keV	$\log \frac{L_X}{L_{bol}}$
GJ 832	M1.5	4.9	8.67	1.46	–	–0.31	3.40	0.64	26.77 ± 0.21	–9.09
GL 581	M3.0	6.3	10.55	1.60	84.0	–0.33	0.04	0.05	<26.89	<–4.57
Fomalhaut	A3.0 V	7.7	1.16	0.09	–	0.00	115.00	3.00	<25.90	<–8.88
GJ 849	M3.5	8.8	10.42	1.52	–	0.00	2.35	0.82	27.25 ± 0.26	–6.73
HD 285968	M2.5 V	9.4	9.97	1.51	38.9	–0.10	0.07	0.03	27.48 ± 0.28	–6.13
GJ 436	M2.5	10.2	10.68	1.52	45.0	–0.32	0.03	0.07	27.16 ± 0.34	–6.36
HD 3651	K0.0 V	11.0	5.80	0.92	–	0.05	0.28	0.20	27.25 ± 0.23	–5.66
HD 69830	K0.0 V	12.6	5.95	0.79	–	–0.05	0.08	0.03	27.47 ± 0.30	–4.84
HD 40307	K2.5 V	12.8	7.17	0.93	–	–0.31	0.05	0.01	26.99 ± 0.28	–7.36
HD 147513	G3.0 V	12.9	5.37	0.60	–	–0.03	1.26	1.00	29.01 ± 0.16	–3.80
υ And	F8.0 V	13.5	4.09	0.54	12.0	0.09	0.06	0.69	28.11 ± 0.22	–6.86
γ Cep	K2.0 V	13.8	3.22	1.03	–	0.00	2.04	1.60	26.96 ± 0.20	–7.34
HR 810	G0.0 V	15.5	5.40	0.57	7.0	0.25	0.91	1.94	28.74 ± 0.21	–7.45
HD 128311	K0.0	16.6	7.51	0.99	11.5	0.08	1.10	2.18	28.52 ± 0.21	–4.57
HD 7924	K0.0 V	16.8	7.19	0.82	–	–0.15	0.06	0.03	27.45 ± 0.29	–6.75
HD 10647	F8.0 V	17.3	5.52	0.53	–	–0.03	2.10	0.91	28.21 ± 0.17	–4.88
ρ CrB	G0.0 V	17.4	5.40	0.61	19.0	–0.24	0.22	1.04	<27.69	<–6.13
GJ 3021	G6.0 V	17.6	6.59	0.75	–	0.20	0.49	3.32	29.02 ± 0.21	–7.00
HD 87833	K0.0 V	18.1	7.56	0.97	–	0.09	3.60	1.78	27.58 ± 0.20	–6.79
HD 192263	K2.0 V	19.9	7.79	0.94	27.0	–0.20	0.15	0.72	28.03 ± 0.35	–4.81
HD 39091	G1.0 IV	20.5	5.67	0.58	–	0.09	3.29	10.35	27.33 ± 0.20	–6.03
HD 142	G1.0 IV	20.6	5.70	0.52	–	0.04	0.98	1.00	<28.20	<–5.63
HD 33564	F6.0 V	21.0	5.08	0.45	–	–0.12	1.10	9.10	27.84 ± 0.30	–6.66
HD 210277	G0.0 V	21.3	6.63	0.71	–	0.19	1.10	1.23	<27.85	<–5.68
70 Vir	G4.0 V	22.0	5.00	0.69	31.0	–0.03	0.48	7.44	27.42 ± 0.28	–6.33
HD 19994	F8.0 V	22.4	5.07	0.57	–	0.23	1.30	2.00	28.16 ± 0.28	–6.41
HD 134987	G5.0 V	25.0	6.45	0.70	–	0.23	0.78	1.58	<27.99	<–5.75
HD 16417	G1.0 V	25.5	5.78	0.67	–	0.19	0.14	0.07	<28.28	<–5.73
HD 60532	F6.0 IV-V	25.7	4.45	0.48	–	–0.42	0.76	3.15	<26.98	<–7.53
HD 181433	K3.0 IV	26.1	8.38	1.04	–	0.33	0.08	0.02	<27.08	<–6.05
HD 30562	F8.0 V	26.5	5.77	0.63	–	0.24	2.30	1.29	<26.97	<–7.07
HD 179949	F8.0 V	27.0	6.25	0.50	9.0	0.22	0.05	0.95	28.61 ± 0.25	–4.40
HD 150706	G0.0	27.2	7.03	0.57	–	–0.13	0.82	1.00	28.88 ± 0.19	–5.04
HD 82943	G0.0 V	27.5	6.54	0.62	–	0.27	0.75	2.01	<28.01	<–5.75

Notes. Stellar and planetary parameters taken from `www.exoplanet.eu`, bolometric luminosities calculated from m_V with bolometric corrections from Flower (1996). X-ray luminosities taken from Kashyap et al. (2008), except for upper limits for *HD 16417*, *HD 30562*, *HD 181433* and *HD 60532*, which were calculated from original data.

trend in L_X with a_{pl} as planet-induced, which leads to remaining L_X-ratio of stars with close-in and far-out planets of ≈2, with an overlap of the (simulated) L_X-distributions at 1σ level.

We do not see a significant difference of L_X-distributions in dependence on a_{pl} in our sample as shown in Fig. 4. There is also no significant trend of L_X/L_{bol} with a_{pl} evident in our data. We do not try to correct artificially for selection effects, since these are various and interdependent: since stellar activity masks the planet-induced radial-velocity signal, small far-out planets are more easily detected around very inactive stars. Similarly, those planets are also easier to detect around low-mass and therefore late-type stars, but very late-type stars have again higher L_X/L_{bol} values than earlier-type and therefore heavier stars. A quantitative estimate of activity-related selection effects is therefore extremely difficult. But as shown in Sect. 6.1, there is no significant *additional* effect on activity visible in our data which can be attributed to the influence of massive close-in planets.

There has also been an effort to measure coronal SPI for an individual target: the star *HD 179949* by Saar et al. (2008), which showed the largest SPI signatures in chromospheric data so far. The star's X-ray flux was measured several times during May 2005; in September 2005, the star was in an "On"-state of SPI as seen in the chromosphere. The measured X-ray fluxes above 0.3 keV vary by ±15%, a typical level also for intrinsic stellar X-ray variability. When folded with the orbital period, the profile of X-ray variability does not match the one seen in chromospheric data very well; interpretations of variability with the stellar rotation period are also possible. To see how chromospheric and coronal variability compare with each other for this star, we can do a rough estimate: a variation of 2.5% in the Ca II K line compared to the mean stellar spectrum should translate into something of the same relative order of magnitude for the Mount Wilson S index. The S index variation should even be a bit smaller than 2.5%, since the S index averages over the H and K line, and the H line is less sensitive to activity effects. If we compare this to stars with known activity cycles such as *61 Cyg*, one finds there (Hempelmann et al. 2006) that the S index during one stellar activity cycle varies by ±15%, while the X-ray flux in the 0.2–2.0 keV band varies by ±40%. A similar ratio of X-ray to Ca II fluxes yields for *HD 179949* an expected X-ray variation of ≈7%, less than a typical intrinsic variability level for late-type main-sequence stars. However, this ratio between X-ray and Ca II fluxes should only apply if activity enhancement via SPI works via similar mechanisms as normal stellar activity does, which is not necessarily the case given the possibility of Jupiter-Io-like interaction scenarios.

A basic quantitative scenario for coronal magnetic SPI has been proposed by Cohen et al. (2009), suggesting that the presence of a close-in planetary magnetosphere hinders the expansion of the stellar magnetic field and the acceleration of the stellar wind, causing a higher plasma density in a coronal "hot spot". In their model, the hot spot leads to variations of the X-ray flux of ≈30% when rotating in and out of view, and compared to a setting without a planet, the overall X-ray flux is enhanced by a factor of ≈1.5 for a stellar dipole field and a factor of ≈15 for a stellar magnetic field like the Sun's in an activity maximum. If we compare this to our sample, we can conclude that an activity enhancement of more than one order of magnitude is not a common effect in stars with Hot Jupiters, since such an activity overshoot for stars with Hot Jupiters would yield significantly different results in our sample's trend of L_X with $\log(a_{pl}^{-1} \times M_{pl})$.

In summary, we can conclude from our analysis that there is no major average activity enhancement in the corona of stars which is induced by their planets. Any trends seen in our sample seem to be dominated by selection effects.

6.3. Promising individual targets

SPI has been claimed for a handful of targets in chromospheric emissions at selected times. Even if there has been no stringent detection of corresponding coronal SPI yet for these stars, simultaneous observations in the optical and X-ray regime yield precious insight into the interplay of stellar and planetary magnetic fields. The most promising candidates for such coordinated searches are stars with close-in and massive planets which are rather X-ray bright to allow feasible observation plans. This identifies the stars *HD 102195*, *HD 130322*, *HD 189733*, *τ Boo*, *υ And*, *HD 179949* as promising targets. Four of these, namely *HD 189733*, *τ Boo*, *υ And* and *HD 179949*, have been investigated for chromospheric SPI before (Shkolnik et al. 2005). Out of these, *υ And* and *HD 179949* did show chromospheric activity enhancement in phase with the planetary orbit; the other two stars showed indications for increased *variability* of chromospheric activity with P_{orb} (Walker et al. 2008; Shkolnik et al. 2005). The remaining two stars, *HD 102195* and *HD 130322*, have not been analyzed in detail for chromospheric SPI yet, but might as well be interesting targets for combined chromospheric and coronal SPI searches.

7. Conclusions

We analyzed a sample of all known planet-bearing stars in the solar neighborhood for X-ray activity and possible manifestations of coronal Star-Planet-Interactions (SPI) in dependence of the planetary parameters mass and semimajor axis. Our main results are summarized as follows:

1. In our sample of 72 stars, there are no significant correlations of the activity indicator L_X/L_{bol} with planetary mass or semimajor axis.
2. However, we do find a correlation of the X-ray luminosity with the product of planetary mass and reciprocal semimajor axis. Massive close-in planets are often found around X-ray brighter stars.
3. This dependence can be ascribed to selection effects: the radial velocity method for planet detections favors small and far-out planets to be detected around low-activity, X-ray dim stars. Additionally, if SPI induced an excess in L_X without changing the L_X/L_{bol} ratio, SPI would need to cause extremely high energy input in L_{bol}, leading to unrealistically short decay times for the planetary orbit.
4. There is no *additional* effect detectable in L_X which could be attributed to coronal manifestations of SPI.
5. Coronal SPI might still be observable for some individual promising targets, preferably in coordinated observations of the targets' coronae and chromospheres.

Acknowledgements. K.P. and J.R. acknowledge financial support from DLR grants 50OR0703 and 50QR0803. This work is based on observations obtained with *XMM-Newton* and makes use of the *ROSAT* Data Archive.

References

Ayres, T. R. 2004, ApJ, 608, 957
Cohen, O., Drake, J. J., Kashyap, V. L., et al. 2009, ApJ, 704, L85
Cuntz, M., Saar, S. H., & Musielak, Z. E. 2000, ApJ, 533, L151
Flower, P. J. 1996, ApJ, 469, 355
Grießmeier, J., Stadelmann, A., Penz, T., et al. 2004, A&A, 425, 753
Hempel, M., Robrade, J., Ness, J., & Schmitt, J. H. M. M. 2005, A&A, 440, 727
Hempelmann, A., Robrade, J., Schmitt, J. H. M. M., et al. 2006, A&A, 460, 261
Kashyap, V. L., Drake, J. J., & Saar, S. H. 2008, ApJ, 687, 1339
Lammer, H., Selsis, F., Ribas, I., et al. 2003, ApJ, 598, L121
Mayor, M., & Queloz, D. 1995, Nature, 378, 355
Poppenhäger, K., Robrade, J., Schmitt, J. H. M. M., & Hall, J. C. 2009, A&A, 508, 1417
Robrade, J., Poppenhaeger, K., & Schmitt, J. H. M. M. 2010, A&A, 513, A12
Saar, S. H., Cuntz, M., Kashyap, V. L., & Hall, J. C. 2008, in IAU Symp. 249, ed. Y.-S. Sun, S. Ferraz-Mello, & J.-L. Zhou, 79
Schmitt, J. H. M. M. 1997, A&A, 318, 215
Shkolnik, E., Bohlender, D. A., Walker, G. A. H., & Collier Cameron, A. 2008, ApJ, 676, 628
Shkolnik, E., Walker, G. A. H., Bohlender, D. A., Gu, P., & Kürster, M. 2005, ApJ, 622, 1075
Vidal-Madjar, A., Lecavelier des Etangs, A., Désert, J., et al. 2003, Nature, 422, 143
Walker, G. A. H., Croll, B., Matthews, J. M., et al. 2008, A&A, 482, 691

March 23, 2011

Corrigendum:
Coronal properties of planet-bearing stars

K. Poppenhaeger, J. Robrade, and J. H. M. M. Schmitt

Hamburger Sternwarte, University Hamburg, Gojenbergsweg 112, 21029 Hamburg, Germany
e-mail: katja.poppenhaeger@hs.uni-hamburg.de

A&A 515, A98 (2010), DOI: 10.1051/0004-6361/201014245

ABSTRACT

A correction for some wrongly sorted data entries in two tables is given.

Key words. Planet-star interactions – Stars: activity – Stars: coronae – Stars: statistics – X-rays: stars – errata, addenda

In Table 4 and 5 of our previous publication (Poppenhaeger et al. 2010), the columns containing the $\log L_X/L_{bol}$ values for our sample stars and the spectral types in Table 4 were sorted incorrectly.

For all figures and other analyses in the paper, the correct data was used. The corrected tables are given below.

References

Poppenhaeger, K., Robrade, J., & Schmitt, J. H. M. M. 2010, A&A, 515, A98+

Star	Type	Dist. (pc)	m_V	$B-V$	P_* (d)	[Fe/H]	a_{pl} (AU)	M_{pl} (M_{jup})	GTI (s)	net countrate[a] (cts/ks)	F_X (erg s^{-1} cm^{-2})	log L_X 0.2-2 keV	log $\frac{L_X}{L_{bol}}$
ϵ Eri	K2.0 V	3.2	3.73	0.88	11.2	-0.10	3.39	1.55	10385	5611.5± 23.3[b]	1.38E-11	28.22± 0.12	-4.88
GJ 674	M2.5	4.5	9.38	1.53	35.0	-0.28	0.04	0.04	15183	1102.6± 8.6	2.16E-12	27.73± 0.12	-3.80
GL 876	M4.0 V	4.7	10.17	1.67	41.0	-0.12	0.02	0.02	23436	48.9± 1.5	1.13E-13	26.48± 0.13	-5.11
VB 10	M8.0 V	5.8	9.91	0.00	-	0.00	0.36	6.40	10810	23.2± 1.5	4.91E-14	26.30± 0.14	-3.94
GJ 317	M3.5	9.2	12.00	1.53	-	-0.23	0.95	1.20	11245	14.3± 1.5	3.30E-14	26.52± 0.14	-4.57
HD 62509	K0.0 III	10.3	1.15	1.00	130.0	0.19	1.69	2.90	28759	31.2± 1.1	1.01E-13	27.11± 0.13	-8.08
GL 86	K1.0 V	11.0	7.40	0.77	31.0	-0.24	0.11	4.01	13071	116.8± 3.1	2.94E-13	27.63± 0.12	-5.04
55 Cnc	G8.0 V	13.0	5.95	0.87	42.7	0.29	0.04	0.03	8505	18.6± 1.6	5.77E-14	27.07± 0.14	-6.36
47 UMa	G0.0 V	14.0	5.10	0.56	74.0	0.00	2.11	2.60	6196	2.6± 0.7	1.07E-14	26.40± 0.21	-7.34
51 Peg	G5.0 V	14.7	5.49	0.67	37.0	0.20	0.05	0.47	25299	0.4± 0.2	1.70E-15	26.28± 0.18	-7.37
τ Boo	F7.0 V	15.0	4.50	0.48	3.3	0.28	0.05	3.90	38251	1252.1± 5.7	3.21E-12	28.94± 0.12	-5.09
HD 160691	G3.0 IV-V	15.3	5.15	0.70	-	0.28	0.09	0.04	7046	3.6± 1.2	1.06E-14	26.47± 0.16	-7.36
HD 190360	G6.0 IV	15.9	5.71	0.73	-	0.24	0.13	0.06	2888	2.2± 1.4	5.23E-15	26.20± 0.21	-7.45
HD 99492	K2.0 V	18.0	7.57	1.01	45.0	0.36	0.12	0.11	19928	7.1± 0.6	2.44E-14	26.98± 0.15	-6.14
14 Her	K0.0 V	18.1	6.67	0.90	-	0.43	2.77	4.64	5532	14.6± 2.9	3.25E-14	27.11± 0.14	-6.33
HD 154345	G8.0 V	18.1	6.74	0.76	-	-0.11	4.19	0.95	3845	18.6± 2.4	5.46E-14	27.33± 0.16	-6.03
HD 27442	K2.0 III	18.1	4.44	1.08	-	0.20	1.18	1.28	4636	3.7± 1.3	1.23E-14	26.68± 0.18	-7.72
β Pic	A6.0 V	19.3	3.86	0.17	0.7	0.00	8.00	8.00	54896	0.2± 0.1[c]	6.00E-16	25.40± 0.15	-9.09
HD 189733	K1.5	19.3	7.67	0.93	13.4	-0.03	0.03	1.13	36271	110.3± 1.8	4.11E-13	28.26± 0.12	-4.84
HD 217107	G8.0 IV	19.7	6.18	0.72	37.0	0.37	0.07	1.33	5576	< 6.0	< 1.55E-14	< 26.86	< -6.79
HD 195019	G3.0 IV-V	20.0	6.91	0.64	22.0	0.08	0.14	3.70	8333	2.8± 0.8	6.44E-15	26.49± 0.17	-6.86
16 Cyg B	G2.5 V	21.4	6.20	0.66	31.0	0.08	1.68	1.68	10768	< 1.6	< 5.42E-15	< 26.47	< -7.22
HD 164922	K0.0 V	21.9	7.01	0.80	-	0.17	2.11	0.36	6955	< 3.5	< 1.21E-14	< 26.84	< -6.59
HD 4308	G5.0 V	21.9	6.54	0.65	-	-0.31	0.11	0.05	7837	2.1± 0.7	7.89E-15	26.66± 0.19	-6.92
HD 114783	K0.0	22.0	7.57	0.93	-	0.33	1.20	0.99	3583	2.1± 1.5	6.72E-15	26.59± 0.19	-6.66
HD 216437	G4.0 IV-V	26.5	6.06	0.63	-	0.00	2.70	2.10	3329	8.2± 1.9	1.89E-14	27.20± 0.18	-6.73
HD 20367	G0.0	27.0	6.41	0.52	-	0.10	1.25	1.07	8861	1404.8± 12.6	2.76E-12	29.38± 0.12	-4.40
HD 114386	K3.0 V	28.0	8.80	0.90	-	0.00	1.62	0.99	3601	2.7± 1.2	7.19E-15	26.83± 0.21	-6.13
HD 52265	G0.0 V	28.0	6.30	0.54	-	0.11	0.49	1.13	6954	5.6± 1.0	1.82E-14	27.23± 0.17	-6.63
HD 75289	G0.0 V	28.9	6.35	0.58	16.0	0.29	0.05	0.42	6681	3.0± 0.7	1.21E-14	27.09± 0.20	-6.79
HD 93083	K3.0 V	28.9	8.33	0.94	48.0	0.15	0.48	0.37	7789	7.4± 1.3	1.67E-14	27.22± 0.16	-5.97
HD 102195	K0.0 V	29.0	8.06	0.83	12.0	0.05	0.05	0.45	13043	145.9± 3.4	2.87E-13	28.46± 0.12	-4.81
HD 111232	G8.0 V	29.0	7.61	0.68	30.7	-0.36	1.97	6.80	6996	< 3.2	< 9.72E-15	< 26.99	< -6.41
HD 70642	G5.0 IV-V	29.0	7.18	0.71	-	0.16	3.30	2.00	10935	3.0± 0.7	6.68E-15	26.83± 0.17	-6.75
HD 130322	K0.0 V	30.0	8.05	0.78	8.7	-0.02	0.09	1.08	4194	16.7± 2.2	3.87E-14	27.62± 0.16	-5.66

Table 1. Stellar and planetary parameters of planet-bearing stars within 30 pc, as observed by XMM-Newton.
[a] PN, 0.2-2 keV
[b] MOS1 countrate given, since PN detector suffered from pile-up for this observation
[c] combined MOS countrate given, since PN detector was optically contaminated

Star	Type	Dist. (pc)	m_V	$B-V$	P_* (d)	[Fe/H]	a_{pl} (AU)	M_{pl} (M_{jup})	$\log L_X$ 0.1-2.4 keV	$\log \frac{L_X}{L_{bol}}$
GJ 832	M1.5	4.9	8.67	1.46	-	-0.31	3.40	0.64	26.77± 0.21	-5.04
GL 581	M3.0	6.3	10.55	1.60	84.0	-0.33	0.04	0.05	< 26.89	< -4.57
Fomalhaut	A3.0 V	7.7	1.16	0.09	-	0.00	115.00	3.00	< 25.90	< -8.88
GJ 849	M3.5	8.8	10.42	1.52	-	0.00	2.35	0.82	27.25± 0.26	-4.43
HD 285968	M2.5 V	9.4	9.97	1.51	38.9	-0.10	0.07	0.03	27.48± 0.28	-4.42
GJ 436	M2.5	10.2	10.68	1.52	45.0	-0.32	0.03	0.07	27.16± 0.34	-4.54
HD 3651	K0.0 V	11.0	5.80	0.92	-	0.05	0.28	0.20	27.25± 0.23	-6.11
HD 69830	K0.0 V	12.6	5.95	0.79	-	-0.05	0.08	0.03	27.47± 0.30	-5.90
HD 40307	K2.5 V	12.8	7.17	0.93	-	-0.31	0.05	0.01	26.99± 0.28	-5.95
HD 147513	G3.0 V	12.9	5.37	0.60	-	-0.03	1.26	1.00	29.01± 0.16	-4.56
υ And	F8.0 V	13.5	4.09	0.54	12.0	0.09	0.06	0.69	28.11± 0.22	-6.00
γ Cep	K2.0 V	13.8	3.22	1.03	-	0.00	2.04	1.60	26.96± 0.20	-7.67
HR 810	G0.0 V	15.5	5.40	0.57	7.0	0.25	0.91	1.94	28.74± 0.21	-4.97
HD 128311	K0.0	16.6	7.51	0.99	11.5	0.08	1.10	2.18	28.52± 0.21	-4.54
HD 7924	K0.0 V	16.8	7.19	0.82	-	-0.15	0.06	0.03	27.45± 0.29	-5.69
HD 10647	F8.0 V	17.3	5.52	0.53	-	-0.03	2.10	0.91	28.21± 0.17	-5.54
ρ CrB	G0.0 V	17.4	5.40	0.61	19.0	-0.24	0.22	1.04	< 27.69	< -6.13
GJ 3021	G6.0 V	17.6	6.59	0.75	-	0.20	0.49	3.32	29.02± 0.21	-4.37
HD 87833	K0.0 V	18.1	7.56	0.97	-	0.09	3.60	1.78	27.58± 0.20	-5.52
HD 192263	K2.0 V	19.9	7.79	0.94	27.0	-0.20	0.15	0.72	28.03± 0.35	-5.05
HD 39091	G1.0 IV	20.5	5.67	0.58	-	0.09	3.29	10.35	27.33± 0.20	-6.52
HD 142	G1.0 IV	20.6	5.70	0.52	-	0.04	0.98	1.00	< 28.20	< -5.63
HD 33564	F6.0 V	21.0	5.08	0.45	-	-0.12	1.10	9.10	27.84± 0.30	-6.24
HD 210277	G0.0 V	21.3	6.63	0.71	-	0.19	1.10	1.23	< 27.85	< -5.68
70 Vir	G4.0 V	22.0	5.00	0.69	31.0	-0.03	0.48	7.44	27.42± 0.28	-6.79
HD 19994	F8.0 V	22.4	5.07	0.57	-	0.23	1.30	2.00	28.16± 0.28	-6.00
HD 134987	G5.0 V	25.0	6.45	0.70	-	0.23	0.78	1.58	< 27.99	< -5.75
HD 16417	G1.0 V	25.5	5.78	0.67	-	0.19	0.14	0.07	< 28.28	< -5.73
HD 60532	F6.0 IV-V	25.7	4.45	0.48	-	-0.42	0.76	3.15	< 26.98	< -7.53
HD 181433	K3.0 IV	26.1	8.38	1.04	-	0.33	0.08	0.02	< 27.08	< -6.05
HD 30562	F8.0 V	26.5	5.77	0.63	-	0.24	2.30	1.29	< 26.97	< -7.07
HD 179949	F8.0 V	27.0	6.25	0.50	9.0	0.22	0.05	0.95	28.61± 0.25	-5.23
HD 150706	G0.0	27.2	7.03	0.57	-	-0.13	0.82	1.00	28.88± 0.19	-4.67
HD 82943	G0.0 V	27.5	6.54	0.62	-	0.27	0.75	2.01	< 28.01	< -5.75

Table 2. Stellar and planetary parameters of planet-bearing stars within 30 pc, as observed by ROSAT.

Chapter 6

A search for Star-Planet-Interactions in the upsilon Andromedae system at X-ray and optical wavelengths

K. Poppenhaeger, L. F. Lenz, A. Reiners and J. H. M. M Schmitt
Astronomy & Astrophysics, Volume 528, id.A58 (2011)
The original publication is available at www.aanda.org

January 31, 2011

A search for star-planet interactions in the υ Andromedae system at X-ray and optical wavelengths

K. Poppenhaeger[1], L. F. Lenz[2], A. Reiners[2], J. H. M. M. Schmitt[1], and E. Shkolnik[3]

[1] Hamburger Sternwarte, Hamburg University, Gojenbergsweg 112, 21029 Hamburg, Germany
e-mail: katja.poppenhaeger@hs.uni-hamburg.de
[2] Universität Göttingen, Institut für Astrophysik, Friedrich-Hund-Platz 1, 37077 Göttingen, Germany
[3] Carnegie Institution of Washington, Department of Terrestrial Magnetism, 5241 Broad Branch Road N.W., Washington, DC 20015

Received 27 October 2010; accepted 08 January 2011

ABSTRACT

Context. Close-in, giant planets are expected to influence their host stars via tidal or magnetic interaction. But are these effects in X-rays strong enough in suitable targets known so far to be observed with today's instrumentation?
Aims. The υ And system, an F8V star with a Hot Jupiter, was observed to undergo cyclic changes in chromospheric activity indicators with its innermost planet's period. We aim to investigate the stellar chromospheric and coronal activity over several months.
Methods. We therefore monitored the star in X-rays as well as at optical wavelengths to test coronal and chromospheric activity indicators for planet-induced variability, making use of the *Chandra* X-ray Observatory as well as the echelle spectrographs *FOCES* and *HRS* at Calar Alto (Spain) and the Hobby-Eberly Telescope (Texas, US).
Results. The stellar activity level is low, as seen both in X-rays as in Ca II line fluxes; the chromospheric data show variability with the stellar rotation period. We do not find activity variations in X-rays or in the optical that can be traced back to the planet.
Conclusions. Gaining observational evidence of star-planet interactions in X-rays remains challenging.

Key words. Planet-star interactions – Stars: activity – Stars: coronae – Stars: chromospheres – X-rays: stars – Stars: individual: upsilon Andromedae – X-rays: individuals: upsilon Andromedae

1. Introduction

Interactions between stars and their giant planets have received considerable attention during the last years. Since the discovery of 51 Peg b, a Jupiter-like planet in a four-day orbit around a solar-like star, the influence of stellar irradiation on planetary atmospheres has been investigated by various authors (cf. Lammer et al. 2003; Lecavelier Des Etangs 2007; Erkaev et al. 2007), as have possible effects that giant planets may have on their host star's activity. These star-planet interactions (SPI) are thought to happen via one of two major scenarios (Cuntz et al. 2000), either tidal or magnetic interaction. In the tidal interaction process, the planet induces tidal bulges on the surface of the star, which can cause enhanced stellar activity through increased turbulence in the photosphere. Magnetic interactions can increase stellar activity via magnetic reconnection of planetary and stellar magnetic field lines (Lanza 2008), or via Jupiter-Io-like interaction, i.e. flux tubes that connect star and planet and heat the stellar atmosphere at their footpoints (Goldreich & Lynden-Bell 1969; Schmitt 2009).

There have been dedicated searches for observational signatures of SPI in stellar chromospheres. Shkolnik et al. (2005) investigated 13 stars and found for two stars variations in the Ca II K line core fluxes, a common chromospheric activity indicator, which were in phase with the planetary orbit. That flux excesses appeared once per orbit and not twice suggests that magnetic and not tidal interaction might have been at work. A follow-up study (Shkolnik et al. 2008) found variability with the planetary orbit only for one of the targets during 2005; for other observation times and other targets, only a variability with the stellar rotation period was found. This was interpreted as on/off behavior of SPI; theoretical considerations also show that possible SPI signatures can be variable in time given the changing magnetic configurations in stellar atmospheres (Cranmer & Saar 2007).

Other studies extended the search for SPI signatures into the X-ray regime to test for coronal activity changes in addition to the chromospheric hints found before. A statistical study by Kashyap et al. (2008) claimed that stars with close-in planets are over-active by a factor of four in X-rays, but these authors had to use a large number of upper limits. Poppenhaeger et al. (2010) investigated a complete sample of all planet-bearing stars within 30 pc distance and found no correlation between stellar activity and planetary distance or mass that could not be traced back to selection effects. Scharf (2010) investigated a smaller sample of planet-hosting stars at distances of up to 60 pc and found a correlation of stellar X-ray luminosity and planetary mass for very close planets; however, selection effects could not be ruled out for the low-mass planets ($M_p < 0.1 M_J$) in the sample.

We here investigate the υ And (HD 9826) system for SPI signatures in chromospheric as well as coronal data. The system is one of the star-planet systems with available observations of time-variable (in terms of on/off behavior) SPI signatures as published in Shkolnik et al. (2005, 2008). υ And is an F8V star, orbited by a massive planet ($0.69 M_J$) in a 4.6 d ($a = 0.059$ AU) orbit, as well as by two other planets at much larger distances. This makes υ And a very suitable candidate to search for SPI signatures.

To look for signatures of SPI, we observed the υ And system for the first time nearly simultaneously at optical and X-ray wavelengths, thus testing for chromospheric as well as coronal variability. Because stellar activity in general and expected SPI

Table 1. Optical and X-ray observations of υ And, sorted by observation date. Integrated Ca II K line residuals are given for optical data, but the absolute scales of FOCES and HRS data are not comparable (see text); extrapolated SPI state according to Shkolnik et al. (2005) given for X-ray data (see text).

Instrument	MJD	Ca II K residual	exp. SPI state
FOCES (15μ)	55014.12	-0.05 ± 0.14	-
FOCES (15μ)	55015.12	-0.03 ± 0.19	-
FOCES (15μ)	55016.12	-0.05 ± 0.11	-
FOCES (15μ)	55017.12	-0.01 ± 0.11	-
FOCES (15μ)	55018.12	0.10 ± 0.14	-
FOCES (15μ)	55020.13	0.36 ± 0.14	-
FOCES (15μ)	55021.13	0.07 ± 0.11	-
FOCES (15μ)	55022.13	-0.03 ± 0.13	-
FOCES (15μ)	55023.13	-0.39 ± 0.20	-
FOCES (15μ)	55024.14	-0.24 ± 0.14	-
FOCES (15μ)	55025.13	-0.13 ± 0.14	-
FOCES (15μ)	55027.13	0.36 ± 0.09	-
FOCES (15μ)	55028.13	0.37 ± 0.09	-
FOCES (15μ)	55029.12	0.27 ± 0.14	-
HET / HRS	55049.37	0.50 ± 0.54	-
HET / HRS	55083.27	-0.05 ± 0.49	-
HET / HRS	55090.25	-0.76 ± 0.53	-
FOCES (24μ)	55096.19	0.03 ± 0.17	-
FOCES (24μ)	55099.20	-0.08 ± 0.13	-
FOCES (24μ)	55100.20	-0.05 ± 0.17	-
FOCES (24μ)	55105.21	-0.02 ± 0.14	-
FOCES (24μ)	55107.20	-0.01 ± 0.18	-
FOCES (24μ)	55108.17	-0.01 ± 0.16	-
FOCES (24μ)	55109.17	-0.08 ± 0.16	-
FOCES (24μ)	55110.19	-0.17 ± 0.16	-
HET / HRS	55110.44	-1.10 ± 0.53	-
Chandra ACIS-S	55124.72	-	maximum
Chandra ACIS-S	55126.56	-	minimum
Chandra ACIS-S	55131.29	-	minimum
Chandra ACIS-S	55133.50	-	maximum
HET / HRS	55135.12	-0.22 ± 0.47	-
HET / HRS	55139.34	-0.43 ± 0.49	-
HET / HRS	55141.33	0.72 ± 0.47	-
HET / HRS	55142.35	1.00 ± 0.49	-
HET / HRS	55146.33	0.35 ± 0.48	-
FOCES (24μ)	55169.00	0.13 ± 0.20	-

signatures in particular do not have to be constant in time, it is important to observe the stellar chromosphere and corona at close time epochs.

2. Observations and data analysis

Our optical data were obtained with the FOCES echelle spectrograph (Pfeiffer et al. 1998) at Calar Alto, Spain, and with HRS (Tull 1998), the echelle spectrograph mounted at HET in Texas, US. The X-ray data were collected with the Chandra X-ray Observatory. A complete list of our observations is given in Table 1.

2.1. Optical data from FOCES

We obtained 23 spectra of υ And with the FOCES echelle spectrograph installed at the 2.2m telescope at Calar Alto from July to December 2009, when one spectrum per night was taken. The 14 spectra obtained during July were recorded with the LOR#11i detector with 15μm pixel size, the other 9 spectra were recorded with the Site#1d detector with 24μm pixel size, all with an exposure time of 900s. The covered wavelength range was 3900–9500 Å.

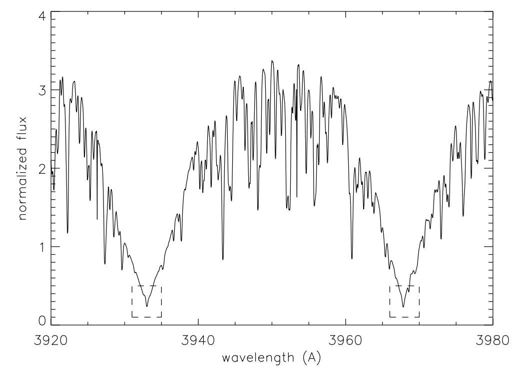

Fig. 1. Typical spectrum of υ And recorded with FOCES. The reversals in the Ca II H and K line cores (dashed boxes) are weak.

The data were reduced with Calar Alto's standard echelle extraction routine d2.pro written in IDL (available from the Calar Alto data server ftp.caha.es). Mean dark frames were subtracted from the nightly spectra, which were then normalized using mean flat fields taken prior to the observations. Wavelength calibration was done with Thorium-Argon frames taken during the same night. The spectral resolution as inferred from the FWHM of ThAr lines is $R \sim 30000$. Since not all of our spectra have ThAr frames taken directly before or after the observation, we cross-correlated the spectra around the Ca II H and K lines and shifted the wavelength axis correspondingly. This deprives us of the possibility to study RV shifts, but does not interfere with our analysis of flux excesses in the Ca II H and K line cores.

A typical spectrum of the Ca II H and K lines of υ And is shown in Fig. 1. The reversals in the two line cores are weak, but clearly visible. Because of the very small emission peaks and since activity affects the K line profile more strongly than the H line profile (see for example Hall et al. (2007)), we concentrate on the K line here. The signal-to-noise ratio (S/N) of the final spectra is at ≈ 150 pixel^{-1} (≈ 860 Å^{-1}) in the quasi-continuum between the H and K line and at ≈ 40 pixel^{-1} (≈ 230 Å^{-1}) in the line cores, summing up to $S/N \approx 150$ in the complete line cores, which stretch over ca. 33 pixels each.

The spectra were normalized by setting the flux of one template spectrum at 3929.5 Å to unity, giving a comparable normalization to the one used by Shkolnik et al. (2005). The remaining spectra were normalized by minimizing the scatter of the flux in two areas to the left and right of the Ca II K line reversal, specifically in the 3930-3932Å and 3934-3936Å range. Later on, a mean spectrum was subtracted from the individual spectra to determine the flux variations in the line cores (see section 3.1). We tested that shifting the normalization areas by 1-2Å outward from the line cores does not significantly change our results. To further test if our normalization method might introduce false variability signals, we also applied our procedure to the Al I line near 3944Å, a photospheric line that should show no activity-related variations. In that part of the spectra, the multitude of lines present makes the normalization less exact, causing a higher overall scatter between the normalized spectra, specifically a noise level of $1\sigma \approx 0.03$ in the chosen normalization.

However, the magnitude of the residuals of the individual spectra compared with the mean spectrum does not change near the Al I line, although it has a comparable depth to the Ca II lines, indicating that the method itself does not produce false variability signals between the two normalization areas.

For the subsequent analysis, the residuals at the Ca II K line core were integrated over a central range of 1Å. The corresponding error bars were calculated by estimating the statistical error in each bin to be the standard deviation of the residuals in the normalization ranges, and then calculating the 2σ error in the integrated area under the Ca II K line center by Monte-Carlo simulations.

2.2. Optical data from HRS

Nine spectra were taken with the HRS instrument at the HET with a resolution of $R \sim 60000$. The data reduction was similar to the FOCES data reduction except for the use of flatfields. The HRS flatfields are taken with a separate, wider calibration fiber to allow 2D-flatfielding. However, the orders of the calibration fiber overlap in the Ca II K region of the flatfields and thus could not be used. We tried to use standard star data as a surrogate for a flatfield, but this added a lot of noise because of their relatively low data quality. To preserve the signal-to-noise ratio of the spectra ($S/N \approx 90$ pixel^{-1} ≈ 520 Å^{-1} in the Ca II K core) we reduced the data without flatfielding.

A consequence of the lacking flatfields is that a direct comparison between the data from FOCES and HRS is not possible. We experimented with artificial, polynomial fits to the continua to obtain comparable line shapes in the Ca II K line, but did not achieve an acceptable solution. As a result the two data sets had to be analyzed individually.

The HRS spectra were normalized by first setting their flux at 3929.5 Å to unity. Then a reference spectrum was chosen and a polynomial was fitted to the quotient of each spectrum and the reference spectrum that represents the missing flatfield. The Ca II K line was omitted from the fitting to avoid removing any variability in the line core. Each spectrum was divided by its fit to receive the normalized spectra.

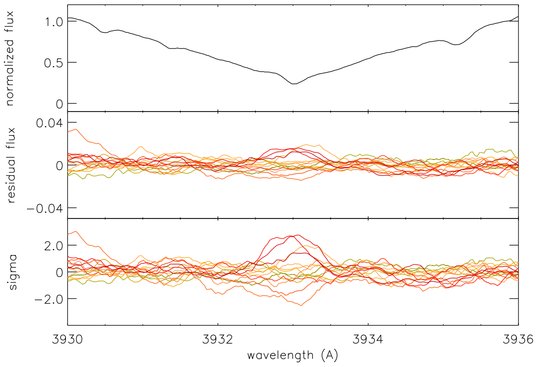

Fig. 2. Variability in Ca II K line cores of the FOCES 15μ data. *upper panel:* normalized mean spectrum; *middle panel:* residual flux with the same normalization; *lower panel:* flux variation in standard deviations.

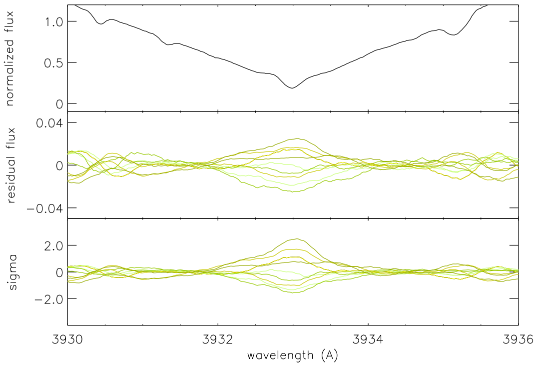

Fig. 3. Same as Fig. 2, but for HRS data.

2.3. X-ray data

We observed the υ And system with the *Chandra* X-ray telescope in four pointings of 15 ks ($\approx$ 4 h) each. These observations were scheduled in a way that two of them cover the projected maximum and two the projected minimum SPI-activity times, as inferred from optical observations done by Shkolnik et al. (2005) (see Table 1). Because SPI can depend on numerous factors such as the stellar magnetic field configuration, SPI signatures are expected to be time-variable (Cranmer & Saar 2007; Shkolnik et al. 2008). It is unlikely, consequently, that we will find SPI in exactly the same configuration as the system exhibited in the chromospheric data from 2005; however, our observational schedule of two observations each that are spaced apart one half of an orbital period is suited to uncover signatures of planet-induced coronal hot spots.

The data were reduced using standard procedures of the CIAO v.4.2 software package. υ And emits soft X-ray radiation with practically all photons having energies below 2 keV, its mean X-ray count rate is $\approx$ 0.025 cts/s in the 0.4-2 keV energy band. We produced light curves with 1 ks binning to obtain acceptable error bars as well as sufficient time resolution to identify possible flares. For the spectra we used energy bins with at least 15 counts per bin for decent statistics. The spectral fitting was performed with Xspec v12.5.

Because υ And is an optically rather bright star ($m_V = 4.09$), the data were collected with a reduced frame time of 0.74s. Additionally, we only use data at energies above 400 eV to exclude possible optical contaminations at the low-energy sensitivity end of the detector.

3. Results

3.1. Chromospheric activity

Following Shkolnik et al. (2005), we computed separate median spectra for the FOCES and the HRS data and computed the residual fluxes of each spectrum compared with the respective median spectrum by subtracting the median spectra binwise from the individual spectra. We also computed the variation measured in standard deviations by dividing the residuals by the poissonian flux error of each bin of the individual spectra, neglecting the error in the median spectra. The results for the 15μ data, smoothed by 15 bins ($\approx$ 0.45Å), are shown in Fig. 2. For the 15μ data, which were recorded in July 2009 under very favorable weather conditions, we find variations in the Ca II K line core at ≈ 2σ levels; the HRS data show similar variation (Fig. 3), while for the 24μ data, the overall noise level is so high that no additional variability in the line core can be identified by naked-eye inspection.

The HRS residuals show variations over a region broader than the Ca II K line core. To the sides of the cores, the residuals also exhibit some broad, wave-like structure. This pattern is probably caused by our normalization; we had to use a polynomial fit to substitute the missing flatfields that apparently does not entirely capture the region around the K line. Nevertheless, the residuals at the K line core exceed the variations outside the core, and therefore we believe that at least some of the core variation is real. Varying the footpoints chosen for the polynomial fit does not significantly change the residuals. Thus, the signal of the K residuals is stable against normalization, but the total uncertainty in the Ca II K line core residuals may contain quite large errors. To estimate the magnitude of these errors, we note that the variation outside the K line core is at a flux level of ±0.01; integrated over the 33 pixels line core, this yields an additional uncertainty of 0.33, which we add to our nominal errors of the integrated residuals.

The magnitude of the K line fluctuations, measured in relative flux deviations, is at a ±0.02 level in our chosen normalization, with an overall noise level of ±0.01. Shkolnik et al. (2005) found for υ And a variation at a ±0.01 level and an overall noise level of ±0.002. Our noise level is much higher with ±0.01, and so we interpret our ±0.02 variation in the core to be consistent with the previously found level of ±0.01; however, given the time-dependence of activity features in stellar chromospheres, one could also expect a differing level of variability.

The Ca II K line core fits into an interval of ≈ 1Å width, see for example Hall et al. (2007) and our data in Fig. 2. We therefore integrate the K line residuals from 3932.5-3933.5Å to obtain a measure for the total variation per spectrum. The crucial question now is whether there is a periodicity in this signal, and if there is, which period can be associated with it.

The timeseries of our integrated residuals is shown in Fig. 4. The FOCES 15μ data show already by naked-eye inspection a variability that tracks slightly more than one cycle of a presumably sinusoidal variation with a periodicity of about eight to nine days. As discussed in section 2.2, the spectra from FOCES and HET cannot be absolutely calibrated with respect to each other, and therefore the calculated residuals are not comparable on an absolute scale either. Thus we proceeded as follows: First, we calculated a Lomb-Scargle periodogram (Lomb 1976; Scargle 1982) of the collected optical data from FOCES, weighting the data points with their respective errors (see Gilliland & Baliunas 1987). This yields three significant peaks with false-alarm probabilities (FAP) below 5%, corresponding to periods of P = 9.3 d, 8.7 d, and 8.2 d, sorted by descending significance. Then, we calculated a weighted Lomb-Scargle periodogram for the HRS data alone. This yields no significant periods with FAP below 20%, which could be expected because there are only nine data points from HRS, distributed over more than three months. Finally, we tried to combine the HRS and FOCES residuals *ad hoc* by scaling down the HRS residuals by a factor of 0.4 so that the highest and lowest values approximately match in both datasets. This is a crude approximation at best; in the Lomb-Scargle periodogram, a possibly wrong scaling will lead to incorrect FAPs, but prominent peaks should still be reproduced reliably. We note here that this scaling also roughly fits with the additional variation level outside the line core that is present in the HRS data mentioned

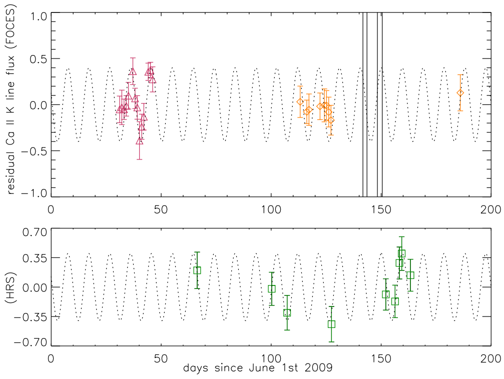

Fig. 4. Time series of Ca II residuals with the highest probability period (9.5 d) indicated by the dotted line; red triangles and orange diamonds are 15μ and 24μ data from FOCES, green boxes are scaled-down HRS data with the same periodicity indicated. *Chandra* observation dates are indicated by vertical solid lines.

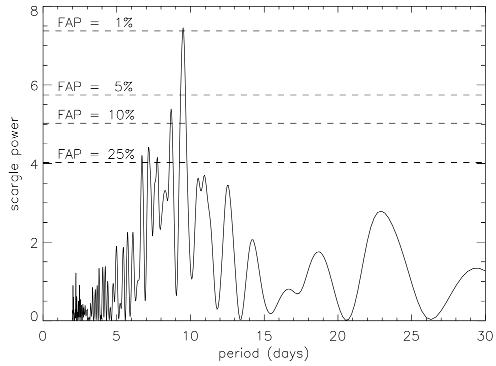

Fig. 5. Lomb-Scargle periodogram of Ca II K line residuals (weighted by their respective errors) with nominal false-alarm probabilities given by the horizontal lines (see text).

above. The result of our periodicity test is shown in Fig. 5. The periodogram of the combined data exhibits the strongest peak at P = 9.5 d with a nominal FAP of 0.9% (keeping in mind that the FAPs may be unreliable for the combined data set). The important point here is that we see a single, isolated main peak at a period that is also found in the FOCES data alone. In contrast to this, near the planetary orbital period of 4.6 d, or half its value, no significant peak appears in any of the periodograms. The periodicities are also clearly reflected in Fig. 6 and 7, where we show the variability of the residuals over the stellar rotation period and the planetary orbital period.

For testing purposes, we subtracted the 9.5 d periodicity from our data to see if the remaining residuals exhibit other periodicities (such as with the orbital period). However, a periodogram of these residuals does not yield other significant periods. Given the expected variability of SPI signatures with time (Shkolnik et al. 2008), we also tried searching for periodicities in subgroups of our data, but the number of data points is not high enough to allow for significant period detection then.

If one chooses to interpret these findings as signatures of periodic activity variations, they are probably associated with the stellar rotation period. The star's rotational velocity $v \sin i$ was measured to be 9.5 ± 0.4 km/s by Gonzalez et al. (2010), its radius is computed by Henry et al. (2000) from stellar parameters as $1.6R_{\odot}$, yielding a rotation period of ≈ 8.5 d, with rather large, but difficult to quantify errors, since the stellar radius was not determined observationally. Wright et al. (2004) give a rotational period of 12 d from spectroscopic monitoring; Henry et al. (2000) find only weak signatures of rotational modulation with periods of 11 d and 19 d respectively in two different data sets. They also state that the difference of the spectroscopically derived periods to the estimate derived from $v \sin i$ measurements might be caused by differential rotation. Still, this stellar rotation period fits the possible periodic signal in our data better than the orbital period of the Hot Jupiter of 4.6 d. Additionally, we have a subset of our data consisting of nightly measurements in July 2010, which closely tracks one complete sinusoidal variation of ≈ 9 d period, making it rather unlikely that we see an alias of the planetary period here, but not the period of 4.6 d itself. This suggests that we see typical low-level stellar activity variations with the stellar rotation period that are not induced by SPI.

3.2. Coronal activity

We extracted X-ray lightcurves of υ And with 1 ks binning in the 0.4-2.0 keV energy band. The lightcurves (see Fig. 8) show variability at 50% level, but no large flares. The mean count rate is constant in observations 1, 2, and 4; the third observation's mean count rate is somewhat lower by 25%. Applying the concept of mean average deviation (MAD) that was used in Shkolnik et al. (2008), we find that the MADs of all but the third observation are similar (0.0063, 0.0060 and 0.0070), whereas the third observation has a MAD that is also lower by ≈ 25% compared with the rest (0.0046).

A typical X-ray spectrum of υ And is shown in Fig. 9; these spectra have a total amount of ≈ 450 source counts, binned by 15 counts as a minimum to allow χ^2 statistics. The spectra of all four pointings cannot be satisfactorily fitted with thermal plasma models with solar abundances and one or two temperature components, while a one-temperature model with variable elemental abundances yields acceptable fits. The results of the spectral fitting performed in Xspec v.12.5 are given in Table 2; the abundances are given with regard to Grevesse & Sauval (1998). The modeled elemental abundances are interdependent with the derived emission measure, and different combinations of both parameters lead to very similar results. For example, the best fits of the first and last observation give lower abundances and higher emission measures than the fits of the other two pointings, but fixing the abundances to the values of the other observations yields comparable emission measures and almost the same fit quality.

Within errors, the spectral properties of all four observations are similar. The plasma temperature is fairly low with ≈ 3 MK. The elemental abundances show a FIP effect, because elements with high first ionization potentials such as oxygen and neon are underabundant compared with iron with a low FIP. This is typical for stars with low to moderate coronal activity, which is determined by the activity indicator $\log L_X/L_{bol} < -4$. υ And's mean X-ray luminosity in these observations is 27.6 erg s^{-1}, its bolometric luminosity is calculated according to Flower (1996) from $m_V = 4.09$ and $B - V = 0.54$ to be 3.3 $L_{bol\odot}$ and therefore its activity indicator is $L_X/L_{bol} = -6.5$, marking υ And as a fairly inactive star.

If the chromospheric data really track the stellar rotation, one might expect to see variability with that period in X-rays as well. This is different from the expected minima and maxima mentioned in Table 1, since we are now dealing with the chromospheric variability from our nearly-simultaneous optical data with a period of 9.5 d. We indicated the times of the *Chandra* pointings as solid vertical lines in Fig. 4; they correspond to rotational phases of 0.64, 0.83, 0.33, and 0.57 as given in Fig. 6. This means that the first, third, and last observation took place at times where the chromospheric activity was (by comparison) high, while the second observation was conducted at moderate chromospheric activity. The mean count rate and mean X-ray luminosity is lower in observation three, but observation two yields values comparable with the first and last observation. We conclude that the coronal activity seems to be dominated by short-term statistical variations and not by the periodicity seen in the chromospheric data.

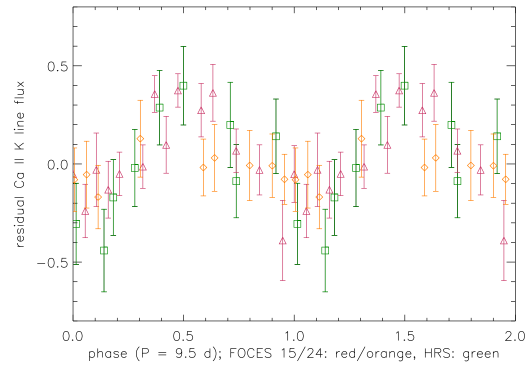

Fig. 6. Ca II K line residuals phase-folded with a period of 9.5 d, presumably the stellar rotation period. Red triangles and orange diamonds are FOCES 15μ/24μ data, green squares are HRS data.

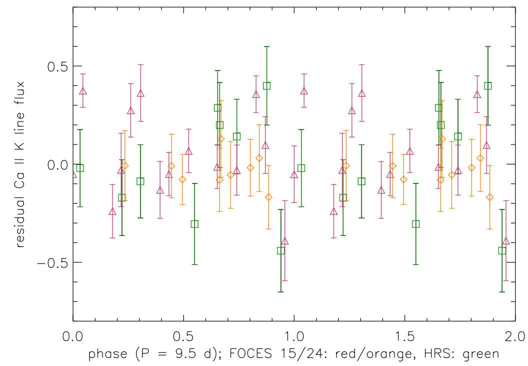

Fig. 7. Same as Fig. 6, but folded with the planetary orbital period of 4.6 d.

Table 2. Spectral modeling results with 1σ errors; emission measure given in units of 10^{50} cm^{-3}.

Parameter	obs. 1	obs. 2	obs. 3	obs.4	all
T_1 (MK)	2.7 ± 0.1	3.1 ± 0.1	3.0 ± 0.2	2.8 ± 0.1	2.9 ± 0.1
EM_1	8.1 ± 1.6	4.4 ± 0.7	4.1 ± 0.9	6.2 ± 1.0	5.2 ± 0.5
O	0.15 ± 0.06	0.34 ± 0.10	0.24 ± 0.09	0.16 ± 0.05	0.23 ± 0.04
Ne	0.22 ± 0.08	0.26 ± 0.10	0.25 ± 0.10	0.18 ± 0.09	0.23 ± 0.05
χ^2_{red} (d.o.f.)	0.81 (21)	0.79 (20)	0.78 (14)	1.47 (19)	1.19 (86)
expected SPI state	maximum	minimum	minimum	maximum	-
log L_X (0.25-2.0 keV)	27.80	27.62	27.56	27.69	27.65

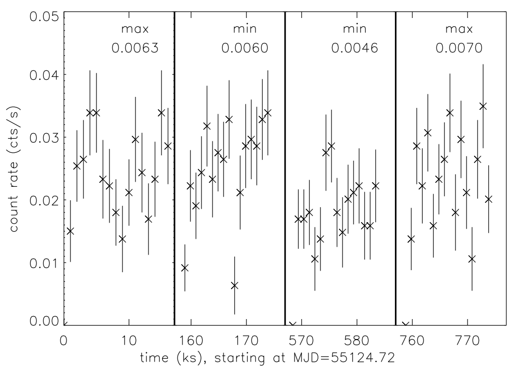

Fig. 8. Background-subtracted X-ray lightcurves of υ And, taken with *Chandra* ACIS-S in the 0.4-2.0 keV energy band, with expected SPI states according to Shkolnik et al. (2005) and MAD values indicated.

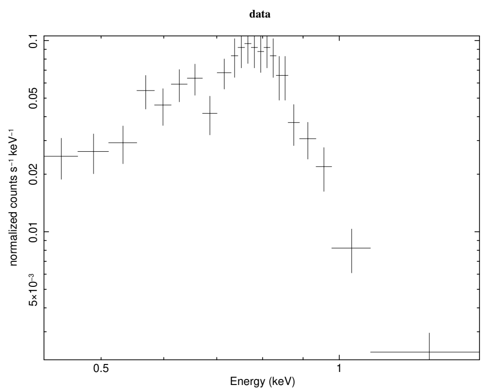

Fig. 9. *Chandra* ACIS-S spectrum of υ And extracted from a single 15 ks exposure. Strong emission in the iron line complexes around 800 eV is visible.

4. Discussion

Searching for signatures of SPI in stellar coronae has proven to be a subtle task. Initial chromospheric measurements indicated that HD 179949's and υ And's chromospheric Ca II fluxes varied with the respective planetary period, but follow-up observations detected dominant variability with the stellar rotation period for several observational epochs. Previous attempts to observe possible SPI signatures in X-rays yielded detections of some activity features such as flares or elevated mean countrates, but attributing these effects unambiguously to SPI is difficult (Pillitteri et al. 2010; Saar et al. 2008).

The υ And system was one of the prime suspects for observing SPI at work in individual star-planet systems based upon chromospheric observations (Shkolnik et al. 2005). However, our observations of the system do not show any significant variations that could be attributed to planetary effects. The variations in the chromospheric Ca II K line cores are small and are consistent with the stellar rotation period. The magnitude of the variations is $\approx 0.6\%$ of the flux in the pseudo-continuum between the Ca II H and K line. From optical and X-ray monitoring of stars such as 61 Cyg (Hempelmann et al. 2006) we know that changes in the S-index (counts in Ca II H and K lines normalized by counts in continuum stretches) of $\pm15\%$ translate to changes in the $0.2-2.0$ keV X-ray band of $\pm40\%$. Accordingly, the extremely small chromospheric variations of υ And should, if ruled by the same activity effects, cause coronal variations of less than two percent over one stellar rotation period. This is much lower than the typical intrinsic variation level of a late-type star. One would only expect strong SPI signatures in X-rays here if the SPI mechanism is fundamentally different from normal activity processes, for example, if SPI happened via Jupiter-Io-like interactions where the star and its close planet are connected by flux tubes (which cannot be the case for the υ And system since the stellar rotation period is longer than the planetary orbital period). If therefore SPI signatures are ruled by similar processes as general stellar activity, it is expected that for low-activity stars possible X-ray SPI effects can hide in the intrinsic stellar variability level. For the corona and the chromosphere of υ And we see that the star does not show any signs of planet-induced activity at the epoch of our observations; it is instead a low-activity star with some indication for rotational modulation in chromospheric emissions.

From this data and other searches for SPI signatures, it seems that stars with low to moderate activity do only exhibit very low levels of SPI effects. To unambiguously detect SPI signatures in the future, stars with extremely close-in planets (< 2 d) will be the most promising candidates. According to recent models (Lanza 2009), magnetic SPI can occur not only through reconnection between the stellar and planetary magnetic field lines, but also by the planetary field that disturbs stellar magnetic loops that have stored energy by normal stellar activity processes and triggers the release of energy. The analysis of observational data (Shkolnik et al. 2008) has also shown that signatures of SPI may be detectable only at certain time epochs, presumably depending on the changing configuration of stellar and planetary magnetic fields. Stars with higher activity levels and larger coronal loops could be rewarding targets for SPI searches if observed with good phase coverage and higher S/N to enable a differentiation between intrinsic stellar variability and SPI effects.

5. Conclusions

Our main results are summarized as follows:

1. υ And is a star of low chromospheric activity, with the coronal activity consistently being at a low level as well, indicated by the coronal activity indicator $\log L_X/L_{bol} = -6.5$.
2. Our data show variations of the Ca II K line core emission compared to the mean spectrum. These variations have a period of ≈ 9.5 d, close to the stellar rotation period of ≈ 8.5 d.
3. The X-ray data do not show significant changes between expected SPI maximum and minimum states, neither in the lightcurves nor in the spectra. The spectra show a FIP effect, with iron being overabundant by a factor of ≈ 4 compared to neon, typical for stars with low to moderate X-ray activity.
4. In our observations, the υ And system does not show signatures of star-planet interactions. The periodicity observed in chromospheric activity indicators is very close to the calculated stellar rotation period and is therefore probably induced by non-SPI-related active regions on the star. Gaining observational evidence for star-planet interactions in X-rays remains a challenge.

Acknowledgements. K. P. acknowledges financial support from DLR grant 50OR0703. A. R. acknowledges research funding from the DFG under RE 1664/4–1. This work is based on observations obtained with *Chandra* X-ray Observatory, *FOCES* at Calar Alto and *HRS* at the Hobby-Eberly Telescope, Texas. The Hobby-Eberly Telescope (HET) is a joint project of the University of Texas at Austin, the Pennsylvania State University, Stanford University, Ludwig-Maximilians-Universität München, and Georg-August-Universität Göttingen. The HET is named in honor of its principal benefactors, William P. Hobby and Robert E. Eberly.

References

Cranmer, S. R. & Saar, S. H. 2007, ArXiv Astrophysics e-prints
Cuntz, M., Saar, S. H., & Musielak, Z. E. 2000, ApJ, 533, L151
Erkaev, N. V., Kulikov, Y. N., Lammer, H., et al. 2007, A&A, 472, 329
Flower, P. J. 1996, ApJ, 469, 355
Gilliland, R. L. & Baliunas, S. L. 1987, ApJ, 314, 766
Goldreich, P. & Lynden-Bell, D. 1969, ApJ, 156, 59
Gonzalez, G., Carlson, M. K., & Tobin, R. W. 2010, MNRAS, 403, 1368
Grevesse, N. & Sauval, A. J. 1998, Space Science Reviews, 85, 161
Hall, J. C., Lockwood, G. W., & Skiff, B. A. 2007, AJ, 133, 862
Hempelmann, A., Robrade, J., Schmitt, J. H. M. M., et al. 2006, A&A, 460, 261
Henry, G. W., Baliunas, S. L., Donahue, R. A., Fekel, F. C., & Soon, W. 2000, ApJ, 531, 415
Kashyap, V. L., Drake, J. J., & Saar, S. H. 2008, ApJ, 687, 1339
Lammer, H., Selsis, F., Ribas, I., et al. 2003, ApJ, 598, L121
Lanza, A. F. 2008, A&A, 487, 1163
Lanza, A. F. 2009, A&A, 505, 339
Lecavelier Des Etangs, A. 2007, A&A, 461, 1185
Lomb, N. R. 1976, Ap&SS, 39, 447
Pfeiffer, M. J., Frank, C., Baumueller, D., Fuhrmann, K., & Gehren, T. 1998, A&AS, 130, 381
Pillitteri, I., Wolk, S. J., Cohen, O., et al. 2010, ApJ, 722, 1216
Poppenhaeger, K., Robrade, J., & Schmitt, J. H. M. M. 2010, A&A, 515, A98+
Saar, S. H., Cuntz, M., Kashyap, V. L., & Hall, J. C. 2008, in IAU Symposium, Vol. 249, IAU Symposium, ed. Y.-S. Sun, S. Ferraz-Mello, & J.-L. Zhou, 79–81
Scargle, J. D. 1982, ApJ, 263, 835
Scharf, C. A. 2010, ApJ, 722, 1547
Schmitt, J. H. M. M. 2009, in American Institute of Physics Conference Series, Vol. 1094, American Institute of Physics Conference Series, ed. E. Stempels, 473–476
Shkolnik, E., Bohlender, D. A., Walker, G. A. H., & Collier Cameron, A. 2008, ApJ, 676, 628
Shkolnik, E., Walker, G. A. H., Bohlender, D. A., Gu, P., & Kürster, M. 2005, ApJ, 622, 1075
Tull, R. G. 1998, in Society of Photo-Optical Instrumentation Engineers (SPIE) Conference Series, Vol. 3355, Society of Photo-Optical Instrumentation Engineers (SPIE) Conference Series, ed. S. D'Odorico, 387–398
Wright, J. T., Marcy, G. W., Butler, R. P., & Vogt, S. S. 2004, ApJS, 152, 261

Chapter 7

A correlation between host star activity and planet mass for close-in extrasolar planets?

K. Poppenhaeger and J.H.M.M. Schmitt
Submitted to The Astrophysical Journal

Draft version March 18, 2011
Preprint typeset using LaTeX style emulateapj v. 11/12/01

A CORRELATION BETWEEN HOST STAR ACTIVITY AND PLANET MASS FOR CLOSE-IN EXTRASOLAR PLANETS?

K. Poppenhaeger and J.H.M.M. Schmitt
katja.poppenhaeger@hs.uni-hamburg.de
Hamburger Sternwarte, Gojenbergsweg 112, 21029 Hamburg, Germany
Draft version March 18, 2011

ABSTRACT

The activity levels of stars are influenced by several stellar properties, such as stellar rotation, spectral type and the presence of stellar companions. In analogy to binaries, planetary companions are also thought to be able to cause higher activity levels in their host stars, although at lower levels. Especially in X-rays, such influences are hard to detect because coronae of cool stars exhibit a considerable amount of intrinsic variability. Recently, a correlation between the mass of close-in exoplanets and their host star's X-ray luminosity has been detected, based on archival X-ray data from the ROSAT All-Sky Survey. This finding has been interpreted as evidence for Star-Planet Interactions. We show in our analysis that this correlation is caused by selection effects due to the flux limit of the X-ray data used and due to the intrinsic planet detectability of the radial velocity method, and thus does not trace possible planet-induced effects. We also show that the correlation is not present in a corresponding complete sample derived from combined XMM-Newton and ROSAT data.

Subject headings: stars: planet-star interactions — stars: activity — stars: coronae — X-rays: stars

1. INTRODUCTION

The possibility of interactions between stars and their planets, causing an activity enhancement of the host star, is currently a debated issue. Possible mechanisms for such Star-Planet Interaction (SPI) are tidal and magnetic interaction scenarios (Cuntz et al. 2000); also, planets triggering the release of energy, which has been built up in tangled coronal loops by normal stellar activity processes, is possible (Lanza 2009). While chromospheric and photospheric observations have yielded some hints for such interactions (Shkolnik et al. 2005, 2008; Lanza et al. 2010), the analysis of possible coronal signatures of SPI has led to differing results (Kashyap et al. 2008; Poppenhaeger et al. 2010b; Scharf 2010; Poppenhaeger et al. 2010a).

In a recent study, Scharf (2010) analyzes a stellar sample derived from archival ROSAT X-ray data and derives a correlation of exoplanetary mass M_p with the host star's X-ray luminosity for planets closer to their host star than 0.15 AU, which is interpreted as a lower floor of possible stellar X-ray luminosity caused by the presence of massive, close planets. We replot the data from that sample in Fig. 1; it indeed shows an amazing correlation of planetary mass and stellar X-ray luminosity. This would be an extremely interesting finding if the correlation was really caused by SPI. We therefore conduct an in-depth analysis of possible factors able to cause such a correlation, using both the sample from Scharf (2010) as well as a complete sample of planet-hosting stars within 30 pc distance, which we presented in Poppenhaeger et al. (2010b). We specifically investigate possible sample selection effects, determine suitable variables which should be tested for correlations with each other, and compare the results derived for the two samples mentioned above.

2. SAMPLE PROPERTIES

Scharf (2010) selected a stellar sample consisting exclusively of X-ray detections (and upper limits) derived from ROSAT All-Sky Survey (RASS) data. This sample has two shortcomings when compared to the wealth of data available from today's X-ray missions XMM-Newton and Chandra: First, Scharf (2010) uses no pointed observations, arguing that in RASS a given star was scanned several times, yielding a time-averaged X-ray luminosity. However, this is only true for stars close to the ecliptic poles, as Scharf (2010) points out correctly. Stars near the ecliptic equator are nominally scanned several times only over a two-day period, and most of the given stars with close-in planets are located at latitudes of $\approx \pm 45°$ or lower. Additionally, the orbital periods of planets in the given close-in subsample range from $2.2 - 8.7$ d, yielding phase coverage of substantially less than one orbit for almost all cases. Thus there is no specific advantage of the RASS data compared to XMM-Newton or *Chandra* data, especially given the higher sensitivity and spatial accuracy of these two X-ray telescopes (Jansen et al. 2001; Weisskopf et al. 2000) and the short total observation time of RASS sources which is usually well below 1 ks, compared to typical exposure times in pointings which are in the $10 - 100$ ks domain, depending on the target.

Second, the two stars in the close-in sample with the highest X-ray luminosities, i.e., HD 41004B and HD 162020, are not comparable to the rest of the sample. HD 41004AB is a binary system consisting of a K star and an M star in a close orbit with a projected distance of $0.5''$, the M star being the component with the substellar companion which is at the boundary of planet and brown dwarf. The RASS data does not allow to determine the X-ray luminosity of each of the two stars individually because of ROSAT's rather broad FWHM; however, M stars usually have lower average X-ray luminosities than K stars (Schmitt & Liefke 2004), so that the complete X-ray luminosity of the system should not be attributed soleley to the M star with the planetary companion. Scharf (2010) notes that unresolved binarity contributes to the errors in his sample, however in this case the binary nature of HD 41004 is known and can be accounted for. The other

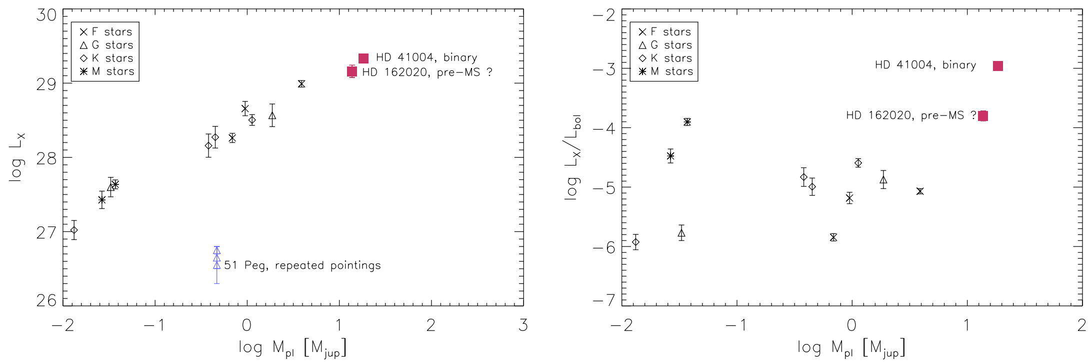

FIG. 1.— Left: L_X vs. planetary mass for stars with close-in planets, data from Scharf (2010). The two incomparable data points form the original sample are shown as red solid squares. For comparison, X-ray data for 51 Peg is inserted as blue open triangles. Right: Activity indicator L_X/L_{bol} vs. planetary mass for stars with close-in planets, data from Scharf (2010).

star, HD 162020, might be a young star as is discussed in Udry et al. (2002); however, the age determination for this star is not entirely clear. If it is a pre-main sequence star, it would not be comparable to the rest of the sample, since such stars are known to have much higher X-ray luminosities than their main-sequence counterparts (Feigelson & Montmerle 1999).

3. METHODOLOGICAL CAVEATS

When testing for correlations of stellar activity with other quantities, an appropriate proxy for stellar activity has to be chosen. Choosing X-ray luminosity as this proxy has two disadvantages: First, there is a correlation between stellar radii and stellar X-ray luminosities, at least for stars with outer convection zones (Schmitt 1997; Raassen & Kaastra 2006). This is why one usually normalizes the X-ray luminosity with the bolometric luminosity of the star to make the activity levels of stars with different spectral types comparable. As a rule of thumb, stars with $L_X/L_{bol} < -5$ are dubbed "inactive", while stars with $L_X/L_{bol} > -4$ are dubbed "active", regardless of spectral type. So, an analysis of X-ray activity for a sample with a variety of stellar masses should also test for correlations of planetary parameters with L_X/L_{bol} to check whether some stellar mass distribution causes a fake signal in correlations with L_X.

Second, in flux-limited survey data there is usually a correlation between detected luminosities (and upper limits) and the distance d of the targets. This is a consequence of the approximately constant exposure time in a survey and the strength of the source signal of targets which scales as $1/d^2$. So, when dealing with survey data, one should carefully check for dependencies on distance.

4. RESULTS

The considerations above lead to two complementary analyses of the results presented in Scharf (2010): reanalyzing the original ROSAT sample as given in Table 1 in Scharf (2010) for dependencies on distance d and L_X/L_{bol}, and testing for such dependencies in the much larger complete sample used in our previous SPI study (Poppenhaeger et al. 2010b).

4.1. *The RASS data revisited*

In Fig. 1, we show the X-ray luminosities of planet-hosting stars with $a_p < 0.15$ AU from the ROSAT sample as a function of the innermost planet's mass. The data points for HD 41004B and HD 162020 are plotted in red for comparison. We would like emphasize the special case of 51 Peg, a star not included in the original sample: this star has been observed in several pointed X-ray observations with ROSAT, XMM-Newton and Chandra, covering different phases of the planetary orbit; it remained undetected in the RASS data and was therefore included by Scharf (2010) only as an upper limit. A detailed analysis of these data has shown (Poppenhäger et al. 2009) the star's X-ray flux to be constant and at a very low level over 16 years, indicating that the star might be in a Maunder minimum state despite its close-in heavy planet. This system is a significant outlier of the L_X vs. M_{pl} relation presented in Scharf (2010) (see Fig. 1), although it fulfills the criterion of having a determined phase-averaged X-ray luminosity.

To test for dependencies on the distance d of the stars, we conduct a Principal Component Analysis (PCA) (Pearson 1901) on the three logarithmic variables $\log L_X$, $\log M_p$ and $\log d$ from the full Scharf (2010) sample. We use the two eigenvectors with the largest eigenvalues as the feature vectors; the third eigenvalue is very small by comparison (0.05 vs. 0.95 and 0.14), meaning that one looses only very little data variance in this analysis. After reprojecting the data, all three variables show a strong linear trend with respect to each other (see Fig. 2). This is a clear indication that the stellar distance is a crucial parameter in this sample which cannot be ignored. It is important to note that in an unbiased sample, L_X and M_p must not depend on stellar distance; if they do as in this sample, a selection effect is present. This provides an explanation for the apparent dependence of L_X on M_p: the detection limit of L_X increases with increasing distance. The detectability of planets is somewhat intricate, and we investiagte depen-

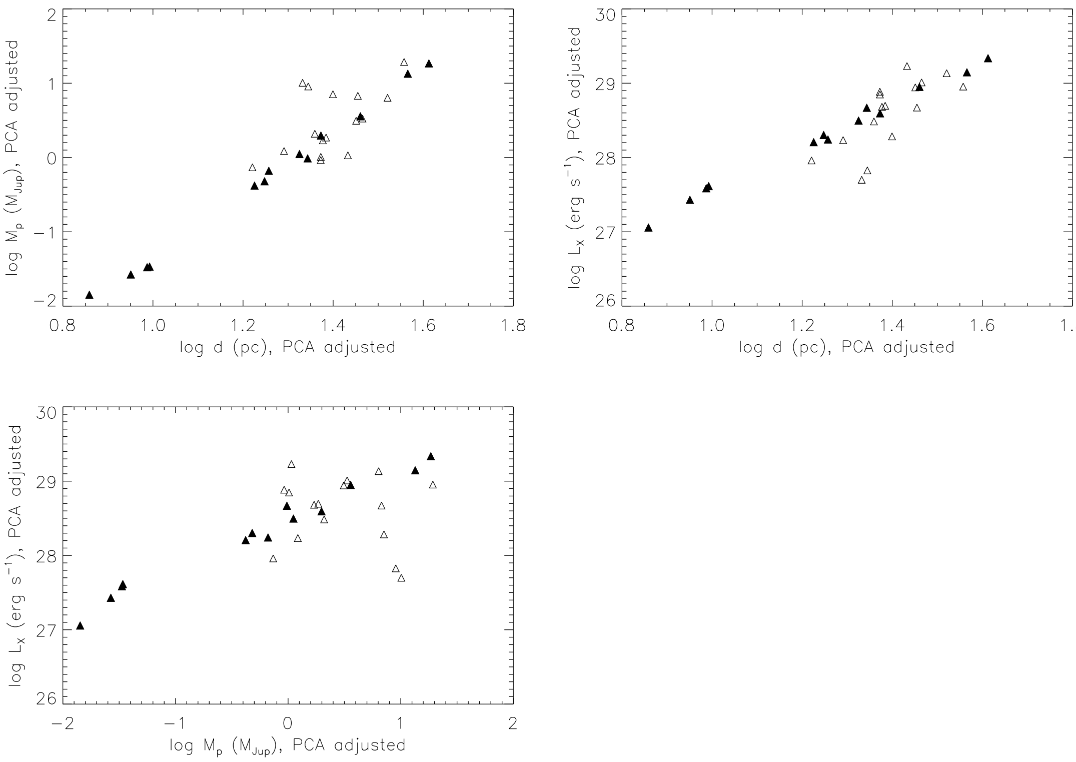

FIG. 2.— Principal Component Analysis results for the Scharf (2010) sample, stars with close-in planets given as filled symbols. All three parameters (d, M_P, L_X) show linear trends with respect to each other, indicating that the stellar distance has a crucial influence in this sample.

dencies in detail in section 4.3. In short, a dependency of planetary mass on stellar distance is present. So, at larger distances, the radial velocity method favours the detection of heavier planets, and low X-ray luminosities cannot be detected any more in the ROSAT All-Sky Survey, which yields the observed trend of L_X with M_p without having to invoke effects from supposed Star-Planet Interactions.

Also without performing a PCA on this sample, the dependencies of L_X and M_p on d are revealed by rank correlation tests. We calculate Spearman's ρ, a rank correlation coefficient which displays a perfect correlation by a value of 1, perfect anticorrelation by -1 and no correlation by 0. For the full Scharf (2010) sample, we find strong correlations of both L_X and M_p with d, indicated by ρ values of 0.49/0.54 respectively, translating to probabilities of 0.6/0.2% that such a correlation can be reached by pure chance. This correlation analysis yields the same result as the PCA; the stellar distance is the crucial parameter in this sample which causes the L_X/M_p correlation.

This is also reflected in the behavior of L_X/L_{bol}, where there is no significant correlation with planetary mass for stars with close-in planets, see Fig. 1. We also checked this visual result with a Spearman's ρ test while excluding the data from the two incomparable stars. This yields $\rho = 0.05$, i.e. a very weak positive correlation; the probability that such a ρ value is reached by chance is 87%. This is not surprising: if the trend in L_X is a distance selection effect and not related to the stellar activity level, then the quantity L_{bol}/L_{bol}, which measures the intrinsic stellar activity level, should be independent from the planetary mass.

4.2. *The correlation as seen with XMM-Newton*

In our further analysis, we use the data presented in Poppenhaeger et al. (2010b), which consists of all known planet-hosting stars within a distance of 30 pc from the Sun, with X-ray properties derived from XMM-Newton and ROSAT data. The errors given are Poissonian errors plus an additional uncertainty of 30% on the X-ray luminosity to account for short-time variations, since a large part of our sample consists of pointed XMM-Newton observations. We use the same sample selection criterion on these data as was used in Scharf (2010) (planets at $a < 0.15$ AU). We show the relation between L_X and M_{pl} in Fig. 3; data from stars which are also present in the sample from Scharf (2010) are plotted as green filled symbols. These stars lie close to a straight line, similar to Fig. 1,

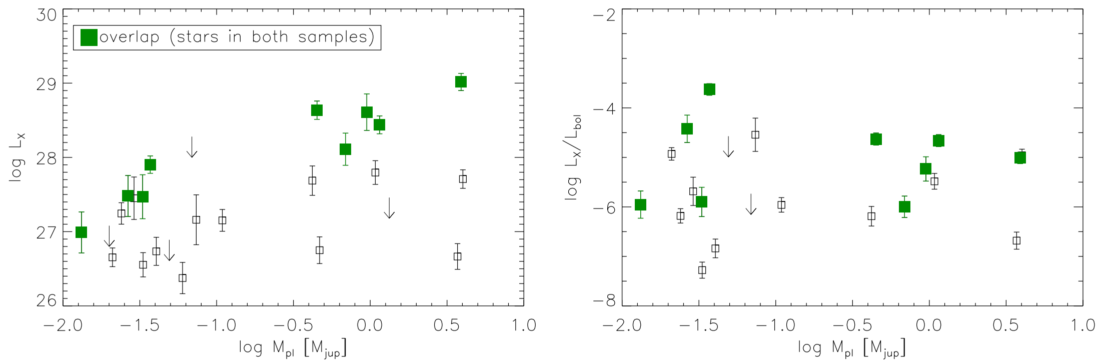

FIG. 3.— Left: L_X vs. planetary mass for stars with close-in planets, data from Poppenhaeger et al. (2010b). The higher sensitivity of XMM-Newton yields many additional X-ray detections in the lower right corner of the diagram, compared to Fig. 1. Stars which are also present in the sample from Scharf (2010) are plotted as green filled symbols. Right: Activity indicator L_X/L_{bol} vs. planetary mass for stars with close-in planets, data from Poppenhaeger et al. (2010b). No significant correlation is present.

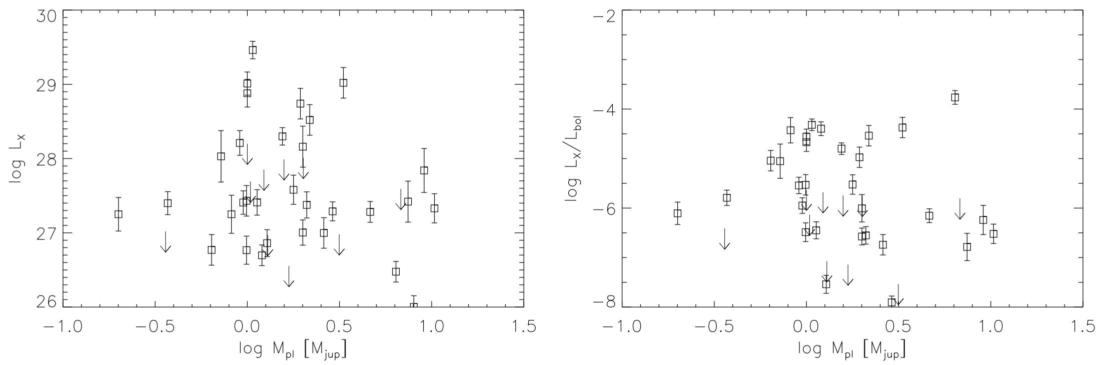

FIG. 4.— Same as Fig. 3, but for stars with planets at semimajor axes ≥ 0.15 AU.

although the data was collected in single pointings and not averaged over larger portions of the planetary orbit. This shows that the averaging process is not crucial for this kind of analysis; the L_X values derived from *XMM-Newton* pointings are very similar to the ones from the RASS data. The main difference to Fig. 1 is that there are many additional X-ray detections in the lower right corner of the diagram. This is contrary to the assumption that massive, close-in planets cause a lower floor for the X-ray luminosity of their host stars.

Additionally, in this sample there is no significant correlation in the relation between the X-ray activity indicator L_X/L_{bol} vs. planetary mass (see Fig. 3); testing for rank correlation yields $\rho = 0.003$, i.e. practically no correlation at all. This is also true for stars with far-out planets, for which no SPI-related effects are expected (Fig. 4). The only significant correlation present in the whole sample is one between X-ray luminosity and the product of planetary mass and inverse semimajor axis. For the intrinsic X-ray activity measured by L_X/L_{bol} no such correlation is present. As discussed in Poppenhaeger et al. (2010b), the L_X correlation is equally strong in a subsample of stars with small, far-out planets as well as in stars with heavy, close-in planets. Poppenhaeger et al. (2010b) conclude that the correlation is caused by selection effects from planet detection; if it was caused by SPI, it should be strong in the second subsample and weak in the first subsample.

For the sake of completeness, we also conducted a PCA for this sample. Here we find for the reprojected data that there is a strong linear trend of M_p with d, but no apparent trends of L_X with d or M_p. This is due to the fact that we also use data from pointed observations in our sample, where observations of more distant targets usually have longer exposure times. This prevents the correlation of L_X with d which is present in the sample of Scharf (2010), and therefore also no correlation between L_X and M_p is present here.

4.3. *The nature of the correlation between distance and planetary mass*

In the above section, we used a volume-limited sample of planet-hosting stars in which most of the stars have been detected in X-rays. In that sense, the sample is complete with regard to X-ray flux. However, the sample is most probably not complete regarding the detection of planets. The portion of planets which are detected by transits is quickly growing since the start of the *CoRoT* and *Kepler* observations, but for stars in the solar neighborhood, the dominant detection mechanism still is the radial velocity method. Selection effects in RV studies need to be identified carefully (O'Toole et al. 2009; Hartman 2010). We now provide an investigation of trends in the basic planetary and stellar parameters that are present the sample used here.

The RV-detectability of a planet depends on several properties: first, on the brightness of the star itself and therefore the quality of the signal in which one searches for RV variations; and second, on the stellar mass M_*, the planetary mass M_p, and the planetary period P. Other influences such as eccentricity of the planetary orbit are ignored here. Specifically, the RV semi-amplitude is proportional to $P^{-1/3} \times M_p \times M_*^{-2/3}$. Thus it should be easier to detect low-mass planets around low-mass stars for a given (fixed) sensitivity.

Our hypothesis is that the detectability decreases as the stellar distance d increases, since the apparent brightness of the star decreases. This means that at larger distances, planets should be found around intrinsically brighter stars. On the main sequence, this implies earlier and therefore more massive stars. To obtain a large enough RV variation for a detection, one would expect that the planets around these stars are more massive compared to the ones around low-mass stars. We test this with Spearman's ρ for the sample from Poppenhaeger et al. (2010b) and find that both stellar mass and distance as well as planetary mass and stellar mass are strongly positively correlated with $P_{false} < 0.5\%$ for both cases; the correlation between stellar mass and the quantity $P^{-1/3} \times M_p$ is even stronger with $P_{false} = 0.1\%$ ($\rho = 0.44$). This confirms our detectability considerations given above. The correlation between stellar distance and planetary mass which we have found in our PCA is therefore caused by the detectability of the radial velocity signal.

As a consequence, the correlation of L_X and M_p is then a combined selection effect of X-ray flux limits in the ROSAT All-Sky Survey and planet detectability. In the sample that is not X-ray flux limited, the correlation of planetary mass and X-ray activity is consequently not present, as demonstrated in Fig. 3.

5. CONCLUSIONS

We conclude that there is no detectable influence of planets on their host stars, causing a lower floor for X-ray activity of these stars. Rather, possible planet-star interactions seem to induce only small effects on the host stars, which will however provide valuable information on stellar and planetary magnetic fields if measured in X-rays.

K. P. acknowledges financial support from DLR grant 50OR0703.

Facilities: XMM, ROSAT.

REFERENCES

Cuntz, M., Saar, S. H., & Musielak, Z. E. 2000, ApJ, 533, L151

Feigelson, E. D. & Montmerle, T. 1999, ARA&A, 37, 363

Hartman, J. D. 2010, ApJ, 717, L138

Jansen, F., Lumb, D., Altieri, B., Clavel, J., Ehle, M., Erd, C., Gabriel, C., Guainazzi, M., Gondoin, P., Much, R., Munoz, R., Santos, M., Schartel, N., Texier, D., & Vacanti, G. 2001, A&A, 365, L1

Kashyap, V. L., Drake, J. J., & Saar, S. H. 2008, ApJ, 687, 1339

Lanza, A. F. 2009, A&A, 505, 339

Lanza, A. F., Bonomo, A. S., Moutou, C., Pagano, I., Messina, S., Leto, G., Cutispoto, G., Aigrain, S., Alonso, R., Barge, P., Deleuil, M., Auvergne, M., Baglin, A., & Collier Cameron, A. 2010, A&A, 520, A53+

O'Toole, S. J., Tinney, C. G., Jones, H. R. A., Butler, R. P., Marcy, G. W., Carter, B., & Bailey, J. 2009, MNRAS, 392, 641

Pearson, K. 1901, Philosophical Magazine, 2, 559

Poppenhaeger, K., Lenz, L. F., Reiners, A., & Schmitt, J. H. M. M. 2010a, ArXiv e-prints

Poppenhaeger, K., Robrade, J., & Schmitt, J. H. M. M. 2010b, A&A, 515, A98+

Poppenhäger, K., Robrade, J., Schmitt, J. H. M. M., & Hall, J. C. 2009, A&A, 508, 1417

Raassen, A. J. J. & Kaastra, J. S. 2006, in ESA Special Publication, Vol. 604, The X-ray Universe 2005, ed. A. Wilson, 103–+

Scharf, C. A. 2010, ApJ, 722, 1547

Schmitt, J. H. M. M. 1997, A&A, 318, 215

Schmitt, J. H. M. M. & Liefke, C. 2004, A&A, 417, 651

Shkolnik, E., Bohlender, D. A., Walker, G. A. H., & Collier Cameron, A. 2008, ApJ, 676, 628

Shkolnik, E., Walker, G. A. H., Bohlender, D. A., Gu, P., & Kürster, M. 2005, ApJ, 622, 1075

Udry, S., Mayor, M., Naef, D., Pepe, F., Queloz, D., Santos, N. C., & Burnet, M. 2002, A&A, 390, 267

Weisskopf, M. C., Tananbaum, H. D., Van Speybroeck, L. P., & O'Dell, S. L. 2000, in Society of Photo-Optical Instrumentation Engineers (SPIE) Conference Series, Vol. 4012, Society of Photo-Optical Instrumentation Engineers (SPIE) Conference Series, ed. J. E. Truemper & B. Aschenbach, 2–16

Chapter 8

A short activity cycle of τ Bootis?

8.1 Introduction

In this chapter, I present an analysis of recently recorded X-ray and optical data on τ Boo, a star which has been suspected to have a very short activity cycle of approximately one year duration. The observations of this star will continue throughout 2011 and 2012, and a paper will be prepared when these observations have been performed. However, as there is already a decent amount of data available which is sufficient for preliminary interpretation, I will present my analysis of the data on τ Boo already here in this thesis.

Table 8.1: *XMM-Newton* and optical observations of τ Boo with expected activity state as extrapolated from magnetic field reconstructions.

ObsID	Obs. date	GTI (ks)	state
0144570101	2003-06-24	70.5	min.
0651140201	2010-06-19	12.7	min.
(optical)	2010-06-19	2.2	min.
0651140301	2010-07-23	7.7	min.
(optical)	2010-07-24	1.7	min.
0651140401	2010-12-19	9.7	max.
0651140501	2011-01-22	13.3	max.

τ Boo is a planet-hosting main sequence star of spectral type F7 located at 15.6 pc distance from the Sun. Its age has been estimated by Saffe et al. (2005) to be roughly 3 Gyr, estimated from isochrones, lithium abundances and chromospheric Ca II activity. For this age, the star rotates rather fast with a mean rotation period of $P_* = 3.23$ d; it also displays quite strong differential rotation with $P_{eq} = 3$ d and $P_{pole} = 3.9$ d at the equator and the poles, respectively (Donati et al. 2008). It has been speculated if this fast rotation stems from a tidal spin-up induced by the giant planet that orbits the star with a period of 3.3 d (Barnes 2001).

Even if magnetic activity is not understood well enough to predict durations and strengths of activity cycles from fundamental stellar parameters, a short activity cycle might be expected for τ Boo as stellar rotation and magnetic activity are related in late-type stars. In the Mount Wilson program (Baliunas et al. 1995), the star did not exhibit any obvious periodic activity changes over several years. However, during the last years, the large-scale magnetic field of τ Boo was reconstructed from spectropolaric measurements using Zeeman Doppler Imaging (Catala et al. 2007; Donati et al. 2008; Fares et al. 2009). These reconstructions suggested that the polarity of the large-scale magnetic field switched twice during a period of two years, indicating an activity cycle of only one year duration.

If these reconstructions really characterize the actual magnetic field configuration of the star, it can be expected in analogy to the Sun that τ Boo is in a state of minimum activity during the phases of a stable, poloidal field configuration. During the polarity switches, when toroidal field configurations are dominant, the activity level should be at a maximum. The available ZDI data suggest that the polarity switches occur yearly in winter; this is why we observed the star twice in summer 2010 and winter 2010/11 in X-rays and additionally in

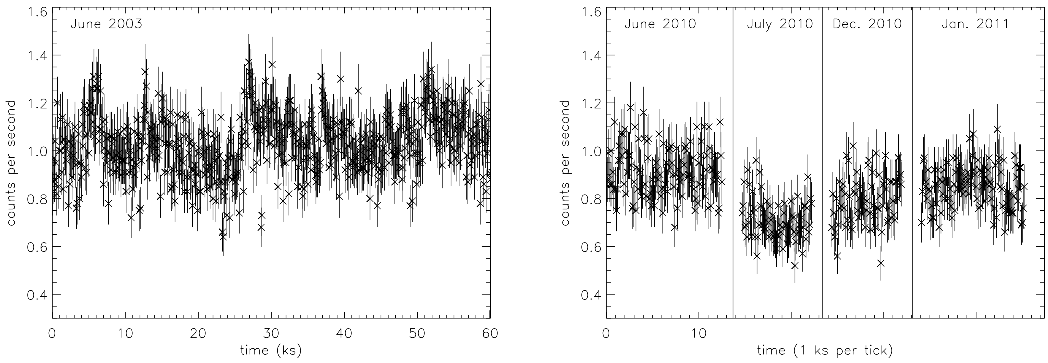

Figure 8.1: Background-subtracted X-ray lightcurves of τ Boo in 2003 and 2010/11 with 100 s time binning, observed with the *XMM-Newton* PN camera.

the optical in summer 2010.

8.2 Observations and data analysis

X-ray data

We monitored τ Boo's X-ray emission with the *XMM-Newton* telescope in four observations. The observation dates were scheduled so that two of them cover the expected activity maximum of the magnetic cycle and two the expected minimum, as extrapolated from the magneto-spectropolarimetric observations performed by Catala et al. (2007); Donati et al. (2008); Fares et al. (2009), see Table 8.1. Additionally, there is an archival *XMM-Newton* observation of the star from June 2003. The data from this observation has been analyzed in detail by Maggio et al. (2011); however, we will re-analyze the dataset along the same lines as we do for our new observations from 2010/11 for better comparability. All observations were performed with the thick filter, as τ Boo is an optically bright target with $m_V = 4.5$. This is also the reason why the optical monitor of *XMM-Newton* had to be blocked and could not be used for scientific analysis.

We reduced the data using standard procedures of the SAS10.0 software package. τ Boo has a mean X-ray countrate of $\approx$ 0.8 cts/s, practically all photons having energies below 5 keV, except for the observation in 2003 where also (few) X-ray source photons of higher energies were collected. We produced light curves with 100 s binning to obtain acceptable error bars as well as enough time resolution to identify possible flares. For the spectra, we used energy bins with at least 15 counts per bin for decent statistics. Significant background signal was present for the 2003 observation, so in analyzing this exposure we used good time intervals with low background signal to extract the source spectra. The spectral fitting was performed with Xspec v12.5.

τ Boo has a stellar companion at an angular distance of 2.8″ (Patience et al. 2002) which is unresolved in the XMM-Newton observations. This companion, GJ 527 B, is a low-mass main-sequence star of spectral type M2. The majority of early M dwarfs ($\approx$ 80%) have luminosities below $\log L_X = 27.5$ (Schmitt et al. 1995). This amounts to a fraction of only 5% of the detected X-ray flux of both τ Boo and GJ 527 B together, so that we can safely choose to neglect the contribution of the low-mass companion to the X-ray emission in our observations.

Optical data from FLWO

The Fred Lawrence Whipple Observatory in Arizona hosts the TRES spectrograph at its 1.5 m telescope. TRES is a cross-dispersed echelle spectrograph with a resolution of $\approx$ 20 000 − 40 000 (depending on the used fiber) in a bandpass covering 3900 − 9100Å. For our observations the medium fiber was used, yielding a spectral resolution of $\approx$ 30 000. The raw spectra were flatfielded and the wavelength calibration was conducted through ThAr reference frames, using the TRES reduction pipeline.

Optical data is available for June and July 2010; in June, a total exposure time of 37 min split into ten exposures was reached; in July, the total exposure time was 28 min split into seven individual exposures.

8.3 Preliminary results

8.3.1 X-ray lightcurves

The X-ray lightcurves of τ Boo, collected in summer 2003, summer 2010 and winter 2010/11, are shown in Fig. 8.1. The lightcurves were extracted from the PN detector in the $0.2 - 5$ keV energy band with a time binning of 100 s. The median countrate in the 2003 observation was higher than in any of the later observations with ca. 1.0 cps. The 2010/11 observations displayed median countrates of 0.90, 0.69, 0.79, and 0.85 cps, respectively. All lightcurves display some short-term variability of 10-30%. The 2003 observation exhibits several small flares, and also the 2010/11 observations show a few flare-like variations, however on a lower level. However, the flares are too small to allow a detailed loop analysis.

The lightcurve variability can be quantified by the MAD, which is the median of the deviation from the median in each lightcurve. The MAD values for the observations are, in chronological order, 0.090, 0.072, 0.050, 0.072, and 0.069.

8.3.2 Activity levels

A good indicator for coronal activity is the ratio of X-ray and bolometric luminosity. Inactive stars typically display values of $\log L_X/L_{bol} < -6$; the Sun's activity index varies between -6.8 and -5.8 during an activity cycle (Judge et al. 2003).

We compute the mean X-ray luminosity of τ Boo in each of the five observations by fitting MOS, PN and RGS spectra in Xspec 12.0 with a *VAPEC* model with four temperature components and variable abundances for the most prominent elements; the fitting process is described in detail in section 8.3.3. We calculate

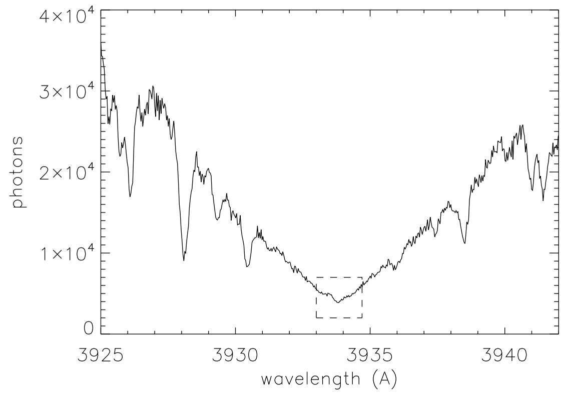

Figure 8.2: Ca II K line of τ Boo in June 2010. Weak emission in the line core (dashed box) is visible.

Table 8.2: X-ray luminosity (0.2-10 keV) and activity indicator L_X/L_{bol} during the five observations of τ Boo.

Date	L_X $(\mathrm{erg\,s^{-1}\,cm^{-2}})$	$\log \frac{L_X}{L_{bol}}$	state
June 2003	7.6×10^{28}	-5.22	min.
June 2010	6.5×10^{28}	-5.29	min.
July 2010	5.1×10^{28}	-5.39	min.
Dec. 2010	5.6×10^{28}	-5.35	max.
Jan. 2011	6.1×10^{28}	-5.32	max.

the X-ray luminosity in the $0.2 - 10$ keV energy band and the activity indicator from the spectral model, the results are given in Table 8.2. In cool stars, the activity indicator typically spans values of -7 to -3, placing τ Boo at a moderate level of activity which is higher than the solar activity level at the maximum of the solar cycle. The highest X-ray activity level was detected in summer 2003, where the X-ray luminosity was higher by 50% compared to the lowest activity level detected in July 2010.

The chromospheric activity level can be determined from the optical spectra we recorded in June and July 2010. More spectra will be taken during 2011, but as of now, these are the only optical spectra available which were recorded near-simultaneously to our X-ray observations. The core of the Ca II K line, located at wavelengths around 3933 Å, is depicted

Table 8.3: Spectral properties of τ Boo's corona during the five observations given with 1σ errors obtained from the fits. Emission measure given in units of $10^{-50}\,\mathrm{cm}^{-3}$.

observation	06/2003	06/2010	07/2010	12/2010	01/2011
EM_1 ($kT_1 = 0.2$ keV)	9.4 ± 0.9	7.9 ± 1.8	6.7 ± 1.2	6.0 ± 2.3	9.7 ± 1.4
EM_2 ($kT_2 = 0.35$ keV)	34.3 ± 1.8	38.7 ± 2.6	33.6 ± 6.0	36.0 ± 4.3	27.0 ± 2.9
EM_3 ($kT_3 = 0.6$ keV)	10.3 ± 0.7	4.9 ± 1.2	2.7 ± 1.5	4.0 ± 1.3	5.4 ± 0.9
EM_4 ($kT_4 = 2$ keV)	1.73 ± 0.17	0.13 ± 0.28	0.0 ± 0.07	0.0 ± 0.24	0.14 ± 0.28
O	0.37 ± 0.01	0.36 ± 0.02	0.36 ± 0.04	0.38 ± 0.03	0.47 ± 0.03
Ne	0.44 ± 0.04	0.31 ± 0.06	0.33 ± 0.08	0.35 ± 0.07	0.45 ± 0.08
Mg	0.66 ± 0.05	0.63 ± 0.09	0.48 ± 0.08	0.47 ± 0.10	0.63 ± 0.11
Si	0.99 ± 0.08	0.88 ± 0.16	0.66 ± 0.24	0.88 ± 0.24	1.33 ± 0.26
Fe	0.96 ± 0.03	0.89 ± 0.04	0.83 ± 0.10	0.81 ± 0.10	1.02 ± 0.07
χ^2 red. (d.o.f.)	1.48 (1025)	1.35 (449)	1.12 (329)	1.05 (351)	1.28 (426)
state	min.	min.	min.	max.	max.

in Fig. 8.2. There is a small amount of emission in the line core, typical for a low to moderate level of activity. To quantify this emission, we calculate the equivalence width of the Ca II K line core, contained in a 1 Å part of the spectrum centered around the minimum of the core, with respect to the pseudo-continuum present between 3945 and 3955 Å. The values are very similar for the optical observations in June and July 2010 with $EW_{June} = 0.938$ and $EW_{July} = 0.925$. Further observations to be obtained in 2011 will give more insight into the variability of τ Boo's chromospheric activity (see also section 8.5).

8.3.3 Spectral properties

We extracted X-ray spectra from each observation of τ Boo, yielding CCD spectra from MOS1, MOS2 and PN (see Fig. 8.3) as well as grating spectra from RGS1 and RGS2 (see Fig. 8.4). We fitted all five spectra from a single observation simultaneously in Xspec12.5, using a thermal plasma model with variable elemental abundances *(VAPEC)* and four temperature components. To make the different observations comparable, we defined a fixed grid of temperatures for all exposures with values of $kT = 0.2, 0.35, 0.6, 2.0$ keV, corresponding to $T = 2.3, 4.0, 6.9, 23$ MK. We then defined the abundances of iron, neon, oxygen, magnesium and silicon to be equal in each tempera-

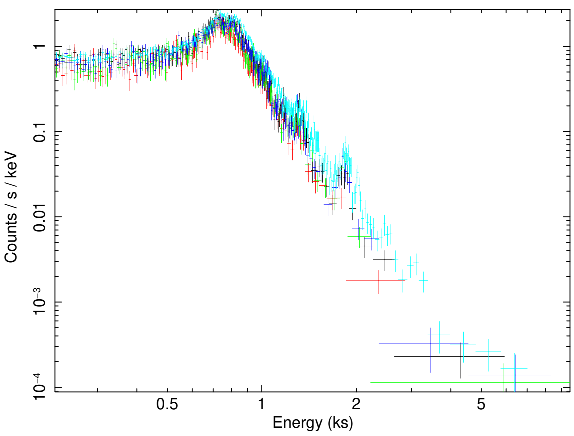

Figure 8.3: X-ray CCD (PN) spectra of τ Boo from 2010/11 and 2003 (black: June 2010, red: July 2010, blue: December 2010, green: January 2011, turquoise: June 2003). The spectra from 2010/11 are very similar to each other, the spectrum from 2003 displays higher mean temperature and emission measure.

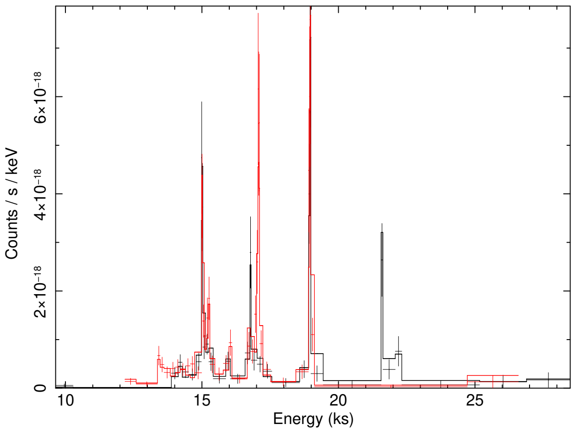

Figure 8.4: X-ray grating spectrum of τ Boo, obtained with RGS1 (black) and RGS2 (red) in January 2011. In this exposure of 13.3 ks duration, the strong emission line complexes of Fe XVII near 15 and 17 Å, the O VIII line near 19 Å and the O VII triplet near 22 Å (visible only in RGS1 because of a broken CCD in RGS2) produce the most remarkable features.

ture component, but allowed said abundances to vary for each observation. As other elements do not produce comparably prominent emission lines in the accessible X-ray spectra, all remaining abundances were fixed at solar photospheric values taken from Grevesse & Sauval (1998). For some of the elements which we allow to vary in the coronal fits, photospheric abundances of τ Boo are available, namely for iron, oxygen, and silicon. However, these abundances are all very similar to each other with $[X/H] \approx 0.3$ (Gonzalez & Laws 2007), so that an additional normalization of these elements with the photospheric abundance of τ Boo is not necessary given the magnitude of the errors in our spectral fits.

In fitting coronal spectra, especially ones of only moderate spectral resolution such as the MOS and PN spectra, there is an interdependence of elemental abundances and emission measure. Fits with high emission measure often produce lower elemental abundances and vice versa, while the fit quality essentially stays the same. When we compare the emission measures or abundances of the individual observations of τ Boo (for example in Fig. 8.5 and 8.6), we therefore normalize the abundances with the total emission measure of each fit, or, if dealing with emission measures, normalize them with the added abundance of iron, oxygen and neon as these are the most precisely determined abundances in our fits.

Coronal abundances

In the Sun, coronal elemental abundances differ systematically from the photospheric abundances (Feldman 1992). Elements with a low first ionization potential (FIP) are enhanced compared to such with a high FIP. In stars, it has been found that the nature of the FIP effect often depends on the activity level (Audard et al. 2003). For rather inactive stars with $\log L_X/L_{bol} < -5$, the FIP effect is solar-like, while very active stars with dominant coronal temperature components of > 10 MK show an inverse FIP effect with the high-FIP elements being overabundant.

As the activity levels of τ Boo are slightly different in the five observations, we analyze the coronal abundances of elements which are well-determined from the EPIC and RGS spectra for each observation. The silicon abundance derived form our spectral fits has larger error bars than the abundances of oxygen, neon, magnesium and iron, due to the fact that no prominent silicon lines are accessible in the energy band covered by RGS, while in EPIC, the generally soft spectra do not yield a large number of counts at energies around 2 keV where Si XIII-XV lines are located.

In the case of τ Boo, we find that all spectra of τ Boo show a FIP effect in the elemental abundances (see Fig. 8.5). Elements with a low FIP such as iron, silicon and, somewhat less pronounced, magnesium are overabundant compared to the high-FIP elements oxygen and neon, see Table 8.3. However, the magnesium abundance is systematically lower than the abundances of the other low-FIP elements, iron and silicon. As the photospheric abundance of magnesium has not been measured for τ Boo, it might be that the star is generally magnesium-poor; in any case, the magnesium abundance is still higher than the corresponding oxygen and neon abundances in each ob-

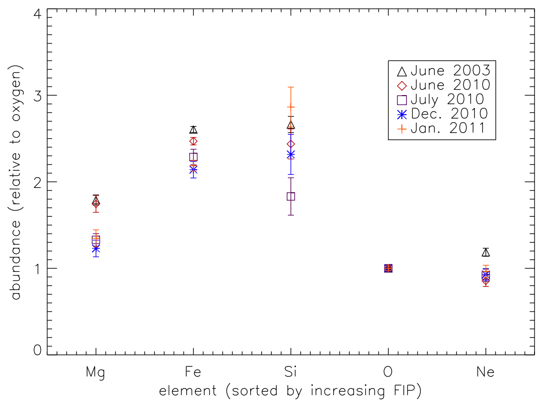

Figure 8.5: Coronal elemental abundances of τ Boo during the five observations, relative to solar photospheric abundances from Grevesse & Sauval (1998) and normalized to the coronal oxygen abundance.

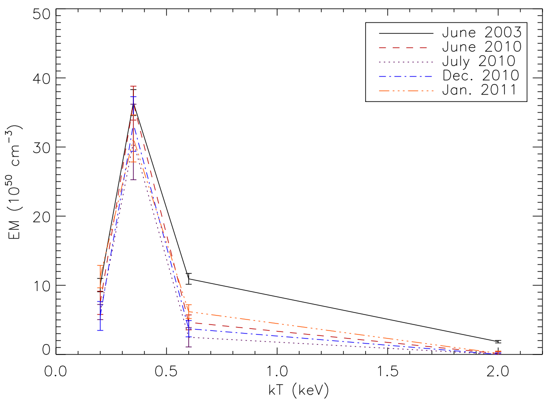

Figure 8.6: Emission measure distribution of the five observations of τ Boo, derived from the 4-T model. Emission measures are scaled by the summed abundances of oxygen, neon and iron for each observation.

servation, fitting the picture of the FIP effect. We also find that changes of the FIP pattern with respect to the activity state in the individual observations are not present on a significant level.

Emission measure and coronal temperature

The abundance-normalized emission measure distribution over the four different temperature bins is shown in Fig. 8.6. This distribution is typical for stars of moderate activity, as the peak of the distribution is located at a temperature of $\approx$ 4 MK. For the four observations with lower activity (2010/11), the emission measure becomes small already at a temperature of 7 MK, and it negligible at > 10 MK. Only the observation form 2003 displays significant emission measure at these higher temperatures, which fits with the overall higher activity state of τ Boo during that time.

Also the total emission measure summed over the temperature bins and normalized by the elemental abundances correlates with the stellar activity. It is largest for the 2003 observation with $5.9 \times 10^{51}\,\mathrm{cm}^{-3}$, and becomes smaller with decreasing activity, with the lowest activity observation in July 2010 having a total emission measure of $3.9 \times 10^{51}\,\mathrm{cm}^{-3}$.

As I have chosen to fit the X-ray data to a grid of fixed temperatures for better comparability, the dominant coronal temperatures in each observation are not obvious at first glance. However, the mean coronal temperatures can be calculated from the fits by weighting the grid temperatures with the emission measure of each temperature bin. The mean temperature in each fit is of the order $4-5\times10^6$ K. Similar to the emission measure, also the mean coronal temperature rises with increasing activity level.

As coronal emission is thought to stem from a superposition of flaring loops with different sizes, this is not surprising. In the standard flare picture, reconnection of magnetic field lines in a coronal loop accelerates electrons downwards into the chromosphere, where their energy dissipates and heats the chromospheric plasma. The chromospheric plasma evaporates and fills the coronal loop, increasing the plasma density and thus the emission measure in that loop, causing it to brighten up in soft X-rays. The activity state of τ Boo as determined by $\log L_X/L_{bol}$ correlating with the mean coronal temperature and emission measure confirms this picture completely.

8.4 Discussion of preliminary results

Our observations have shown that τ Boo is a moderately active star which displays some small-scale variability in X-rays. A FIP pattern in the coronal elemental abundances, typical for stars with low to moderate activity, is present as well. However, using the data available up to now, we do not find evidence for a short activity cycle of ≈ 1 yr duration. Especially an elevated activity state in winter 2010/11 as extrapolated from spectropolarimetric measurements is not present in the stellar coronal emission.

This is not a problem of identifying stellar activity cycles in X-ray emission. It has been shown for two stars other than the Sun, namely HD 81809 and 61 Cyg (Favata et al. 2008; Hempelmann et al. 2006), that the quasi-quiescent coronal emission in general follows the chromospheric activity behavior. For these stars, the activity cycles with ca. 8 and 10 yr are much longer than the one that was proposed for τ Boo.

This leaves two main reasons why the coronal emission does not show the expected long-term variability. On the one hand, the sampling of our data available so far is quite sparse with only four pointings distributed over one year. It might be that we incidentally caught τ Boo in short phases of low activity during winter 2010/11, while the general activity level during that period was significantly higher. For the observations from 2003, a low activity state was extrapolated from the spectropolarimetric data. If truly a 1-year cycle is present, then there are seven cycles between that dataset and the 2010/11 observations. We know from the Sun that different activity cycles can be more or less pronounced, so the higher activity level in 2003 does not necessarily contradict this first possibility of an interpretation.

On the other hand, the magnetic polarity switches recontructed from spectropolarimetric measurements might not be caused by a short magnetic cycle in the first place. In those observations, the Stokes I and V components were measured, which contain information on the *net* magnetic field of the stellar hemisphere that is visible during the individual observations. Areas on the stellar surface which have opposite polarity "cancel out" in the Stokes V signal and can therefore usually not be reconstructed by measuring only these two components. If these areas and their magnetic fields do not match in magnitude completely, the Stokes V signature appears as that of the net field strength of both areas, and thus does not allow a distinction between global net fields and a locally differing field strength of opposite polarity.

In the case of τ Boo, a net radial magnetic field with a strength of up to 10 G has been reconstructed (Fares et al. 2009). In the Sun, the magnetic field strength in sunspots is of the order of several kilogauss, while the global polar field of the Sun is much weaker with only a few Gauss. Even if sunspots usually are present in pairs, it is well possible that a snapshot of one stellar hemisphere of τ Boo contains local magnetic fields in such a way that their integral over the stellar disk yields a net field strength equals 10 G. Therefore, a global magnetic field switch is not necessarily the only possible explanation for the spectropolarimetric data.

8.5 Future observations

In any case, our future observations of τ Boo will allow more insight into the question of this star's activity cycle.

For 2011/12, several observations of τ Boo's coronal and chromospheric emission are scheduled. The coronal X-ray emission will be monitored almost every month from April 2011 to April 2012, using the X-ray observatories *XMM-Newton*, *Chandra*, and *Swift*.

In addition, we will also collect more optical data to determine τ Boo's chromospheric activity state near-simultaneously to the coronal activity. We will again use data from FLWO in Arizona; so far, observations are scheduled for spring and summer 2011, and additional observations covering the period to April 2012 are proposed for.

This closer data sampling will allow us to determine if the low coronal activity in winter 2010/11 is an outlier or just represents the overall activity state of τ Boo. This would strengthen our second interpretation of the data, indicating that no one-year activity cycle is present in this star.

Chapter 9

Summary and future work

Here I summarize the scientific results of my thesis and comment on future research possibilities.

9.1 Summary of scientific results

Most of the work discussed in this thesis has been published in refereed journals such as *Astronomy and Astronphysics* and *The Astrophysical Journal* and has been presented at international conferences. This was done to allow the international community to participate in my results as early as possible. All of these publications deal with the magnetic activity of planet-hosting stars, and several new and original results have been derived.

Maunder minimum states: The planet-hosting star 51 Peg is in a Maunder minimum state, characterized by low and constant X-ray and chromospheric activity profiles over more than 16 years. Its coronal temperature is very low with $T \lesssim 1$ MK, which is similar to the temperature of a solar coronal hole. As chromospheric activity indicators alone can only hint at Maunder minima, this is the first time that substancial observational evidence for a stellar Maunder minimum state has been presented, by using both chromospheric and coronal data.

τ Boo's activity cycle: τ Boo, a fast rotating star with a Hot Jupiter in a synchronous orbit, does not show modulations of its X-ray activity with a period of $\approx$ 1 yr, as had been anticipated from Zeeman Doppler Imaging. The star exhibits low to moderate activity during my observations in 2010/11; in X-ray data from 2003 the activity level was only slightly higher. The elemental abundances show a FIP effect in all X-ray observations, which is often seen in stars with low to moderate activity. These results are preliminary in the sense that more monitoring observations in the optical and in X-rays will be carried out in 2011/12, which will allow to search for activity modulations with longer periods.

Chromospheric SPI: The planet-hosting star υ And, which has been claimed to undergo chromospheric activity changes with the orbital period of its planet, does not exhibit such modulations during my observations in 2009. Instead, υ And showed periodic variability with the stellar rotation period, indicative of active regions being present on the star which were not associated with the planet. Near-simultaneous X-ray observations confirmed this behavior. SPI therefore induces only small effects in this star, if any.

Coronal SPI: In a complete sample of all known planet-hosting stars within 30 pc distance from the Sun, there are no detectable SPI-related effects present in the stellar X-ray emission. The only significant correlation which is present is between stellar X-ray luminosity and the product of planetary mass and reciprocal semimajor axis. This correlation can be traced back to a selection effect from planet detection, since it is present both for massive, close-in planets where one expects to see SPI signatures as well as for small, far-out planets for which SPI effects should be negligible.

Selection effects in planet-hosting stars: There are strong selection effects present in samples of planet-hosting stars which can mimick trends as expected from SPI manifestations. I investigated such selection effects in detail for the radial velocity detection method, which is the dominant method for discovering planets around nearby stars. The detectability of the RV signal depends on the apparent brightness of the star itself (brighter stars yield higher signal-to-noise ratio in optical spectra), as well as on the RV amplitude, which is a function of planetary mass and reciprocal stellar mass and planetary orbital period. This causes small planets to be mostly found around stars with low X-ray luminosity, which can be mistaken for massive planets *causing* higher X-ray luminosities.

9.2 Future work

The results of my work have shown that star-planet interactions do not produce a major contribution to stellar activity. Any hypothetically induced effects are small compared to intrinsic stellar variability, judging from the observational evidence which is available today.

For binary stars, activity features which have been interpreted as related to magnetic interactions have been observed (Salter et al. 2010; Siarkowski et al. 1996; Peterson et al. 2010); as they are apparently negligible for planet-hosting stars, the question arises at which mass range such interactions become significant. Suitable targets for further investigations are therefore M dwarf binaries, as they provide a link in the mass range between planet-hosting stars and binaries of the RS CVn or BY Dra type. I have submitted a proposal to observe the newly discovered close M dwarf binary GJ 3240 B which has a orbital period of only 0.4 d; the analysis of X-ray and optical data from this system will show if this binary displays, apart from high activity due to tidal locking and therefore fast rotation, additonal acitivity features in the form of "star-star interactions".

Also single stars are suited to gain more insight into magnetic activity processes. Two main-sequence stars of intermediate mass, namely τ Boo and ι Hor, recently showed indications of very short activity cycles (1 yr and 1.6 yr, respectively). In the case of τ Boo, I have already shown that its activity cycle as indicated in X-ray emission is most probably longer than the 1 yr duration derived from Zeeman Doppler Imaging. Additional observations in X-rays and in the optical regime will be performed in 2011/12 with closer time sampling to investigate the nature of τ Boo's activity in more detail. For the star ι Hor, the evidence for the short cycle is stronger than for τ Boo since chromospheric activity measurements are available from more than one cycle, thus one does not need to rely on spectropolarimetric reconstrcutions of magnetic fields. For ι Hor, several X-ray observations to be performed by *XMM-Newton* will become available in 2012, allowing to test the chromospheric activity cycle in the stellar coronal emission.

The influence of planets on their host stars' activity may be negligible, but the effect that stellar activity and thus high-energy irration has on close-by planets is certainly not. As planetary evaporation has been observed for HD 209458b, the question arises how such evaporation takes place. There are different models explaining much larger evaporation rates than those emerging from pure Jeans' escape, which make use of the high-energy irradiation of the planetary atmosphere. However, there are no observational constraints for the most crucial parameter in such models, the planetary radius in X-rays. For inflated massive planets, some models assume the X-ray radius to be larger than the optical radius by a factor of $2-4$. I will test the planetary X-ray radius in the system HD 189733, which is similar to HD 209458, but located at a closer distance; the *Chandra* X-ray observations of this system will be carried out in fall 2011. To derive the radius, I will use both folded X-ray lightcurves of the planetary transits as well as a hardness ratio analysis. Normal stellar variability produces a linear relationship between hardness ratio and countrate, since flares of all sizes produce hotter plasma which is both X-ray brighter and has a harder spectrum than cooler plasma. A planetary transit will cause outliers from this relationship, since the transit lowers the X-ray flux by occultation *without* lowering the detected effective plasma temperature. This may yield observation-based estimates of planetary X-ray radii for the first time.

A second important question arises from the HD 209458 system: although the star is apparently able to drive planetary evaporation, it is not detected in X-ray so far. As the system is located at 47 pc distance, this is not surprising for the *ROSAT* All-Sky Survey; however, even in more sensitive *XMM-Newton* observations, a significant X-ray detection could not be made. Together with HD 209458's low chromospheric activity derived from optical spectra, this hints towards a Maunder minimum state of this star. However, the far UV emission of HD 209458, measured in a band spanning $1350 - 1750$ Å by the GALEX space observatory, is stronger than the emission of the Maunder minimum star 51 Peg by a factor of three. Clearly, HD 209458 provides some puzzles concerning stellar activity and its influence on the planetary atmosphere. Therefore I have proposed a new X-ray observation of HD 209458 with *Chandra ACIS-S* to derive the stellar coronal temperature from only a few necessary source counts in a similar way as I have done for 51 Peg in this thesis. If HD 209458 really is in a Maunder minimum state, this can indicate that the planetary evaporation might be dominantly driven by stellar wind instead of irradiation for this system.

This shows that - even if star-planet interactions induce only minor effects - the magnetic activity of planet-hosting stars is a rich field of research awaiting deeper understanding in the future.

Chapter 10

Acknowledgment - Danksagung

Es gibt eine Reihe von Menschen, denen ich hier danken möchte, weil sie mir aus vielerlei Gründen wichtig gewesen sind in den vergangenen drei Jahren und darüber hinaus.

Zunächst ist das mein Doktorvater Jürgen Schmitt, der mir wissenschaftlich freie Hand gelassen hat, mir aber, wann immer ich das brauchte, auch eine Leitfigur war. Ich habe wissenschaftlich und taktisch viel von Dir gelernt, Jürgen. Ebenfalls bedanken möchte ich mich bei Ansgar Reiners, der für mich immer ein sehr offener Ansprechpartner war für meine Fragen zur magnetischen Aktivtät und zum Leben als Wissenschaftler allgemein. Ein Dankeschön geht auch an Jan Robrade, der meine ersten Schritte in der Röntgenastronomie begleitet hat.

Finanzielle Unterstützung wurde mir zuteil durch das Deutsche Zentrum für Luft- und Raumfahrt (DLR) unter der Projektnummer DLR 50OR0703.

Meine Kollegen an der Hamburger Sternwarte haben das Institut zu einem angenehmen und fröhlichen Arbeitsplatz für mich gemacht. Auch nach der Arbeit hatte ich viel Spaß mit euch bei gemeinsamen Kochabenden, Kinobesuchen und "Inspirational Sessions". René, Mariana, Moritz und auch Feo aus Göttingen, ihr seid mir besonders ans Herz gewachsen, und ich bin sehr froh, euch zu kennen.

Tobias, Du bist mir wichtiger als alles andere. Diese Arbeit ist Dir gewidmet.

Chapter 11

Bibliography

Bibliography

Audard, M., Güdel, M., Sres, A., Raassen, A. J. J., & Mewe, R. 2003, A&A, 398, 1137

Ayres, T. R. 2009, ApJ, 696, 1931

Babcock, H. D. 1959, ApJ, 130, 364

Babcock, H. W. 1961, ApJ, 133, 572

Baliunas, S. L., Donahue, R. A., Soon, W. H., et al. 1995, ApJ, 438, 269

Barnes, R., Meadows, V. S., Domagal-Goldman, S. D., et al. 2010, ArXiv e-prints

Barnes, S. A. 2001, ApJ, 561, 1095

Ben-Jaffel, L. 2007, ApJ, 671, L61

Browning, M. K., Miesch, M. S., Brun, A. S., & Toomre, J. 2006, ApJ, 648, L157

Carraro, G., Chiosi, C., Bressan, A., & Bertelli, G. 1994, A&AS, 103, 375

Catala, C., Donati, J., Shkolnik, E., Bohlender, D., & Alecian, E. 2007, MNRAS, 374, L42

Cohen, O., Drake, J. J., Kashyap, V. L., et al. 2009, ApJ, 704, L85

Cuntz, M., Saar, S. H., & Musielak, Z. E. 2000, ApJ, 533, L151

Dikpati, M. & Gilman, P. A. 2001, ApJ, 559, 428

Donati, J., Moutou, C., Farès, R., et al. 2008, MNRAS, 385, 1179

Donati, J., Semel, M., Carter, B. D., Rees, D. E., & Collier Cameron, A. 1997, MNRAS, 291, 658

Drake, F. D. 1961, in Discussion of Space Science Board, National Academy of Sciences, Conference on Extraterrestrial Intelligent Life, Green Bank, West Virginia

Durney, B. R. 1995, Sol. Phys., 160, 213

Eddy, J. A. 1976, Science, 192, 1189

Fares, R., Donati, J., Moutou, C., et al. 2009, MNRAS, 398, 1383

Favata, F., Micela, G., Orlando, S., et al. 2008, A&A, 490, 1121

Feldman, U. 1992, Phys. Scr, 46, 202

Getman, K. V., Broos, P. S., Salter, D. M., Garmire, G. P., & Hogerheijde, M. R. 2011, ArXiv e-prints

Goldreich, P. & Lynden-Bell, D. 1969, ApJ, 156, 59

Gonzalez, G. & Laws, C. 2007, MNRAS, 378, 1141

Grevesse, N. & Sauval, A. J. 1998, Space Science Reviews, 85, 161

Hale, G. E. 1908, ApJ, 28, 315

Hansen-Ruiz, C. S. & van Leeuwen, F. 1997, in ESA Special Publication, Vol. 402, Hipparcos - Venice '97, ed. R. M. Bonnet, E. Høg, P. L. Bernacca, L. Emiliani, A. Blaauw, C. Turon, J. Kovalevsky, L. Lindegren, H. Hassan, M. Bouffard, B. Strim, D. Heger, M. A. C. Perryman, & L. Woltjer, 295–298

Helmholtz, H. v. 1856, The London, Edinburgh and Dublin Philosophical Magazine and Journal of Science, 11, 489

Hempelmann, A., Robrade, J., Schmitt, J. H. M. M., et al. 2006, A&A, 460, 261

Jansen, F., Lumb, D., Altieri, B., et al. 2001, A&A, 365, L1

Jordan, C., Doschek, G. A., Drake, J. J., Galvin, A. B., & Raymond, J. C. 1998, in Astronomical Society of the Pacific Conference Series, Vol. 154, Cool Stars, Stellar Systems, and the Sun, ed. R. A. Donahue & J. A. Bookbinder, 91–+

Judge, P. G. & Saar, S. H. 2007, ApJ, 663, 643

Judge, P. G., Solomon, S. C., & Ayres, T. R. 2003, ApJ, 593, 534

Kashyap, V. L., Drake, J. J., & Saar, S. H. 2008, ApJ, 687, 1339

Komm, R. W., Howard, R. F., & Harvey, J. W. 1993, Sol. Phys., 143, 19

Kopp, R. A. & Poletto, G. 1993, ApJ, 418, 496

Krause, F. & Raedler, K. 1980, Mean-field magnetohydrodynamics and dynamo theory, ed. Williams, L. O.

Lammer, H., Bredehöft, J. H., Coustenis, A., et al. 2009, A&A Rev., 17, 181

Lanza, A. F. 2008, A&A, 487, 1163

Lanza, A. F. 2009, A&A, 505, 339

Leighton, R. B. 1969, ApJ, 156, 1

Lenz, L. F., Reiners, A., & Kürster, M. 2010, ArXiv e-prints

Love, J. 1999, Astronomy and Geophysics, 40, 14

Maggio, A., Sanz-Forcada, J., & Scelsi, L. 2011, A&A, 527, A144+

Massi, M., Menten, K., & Neidhöfer, J. 2002, A&A, 382, 152

Mayor, M. & Queloz, D. 1995, Nature, 378, 355

Neupert, W. M. 1968, ApJ, 153, L59+

Parker, E. N. 1955, ApJ, 122, 293

Patience, J., White, R. J., Ghez, A. M., et al. 2002, ApJ, 581, 654

Peterson, W. M., Mutel, R. L., Güdel, M., & Goss, W. M. 2010, Nature, 463, 207

Pierce, A. K. & Lopresto, J. C. 1984, Sol. Phys., 93, 155

Pillitteri, I., Wolk, S. J., Cohen, O., et al. 2010, ApJ, 722, 1216

Piskunov, N. & Kochukhov, O. 2002, A&A, 381, 736

Pont, F., Gilliland, R. L., Moutou, C., et al. 2007, A&A, 476, 1347

Poppenhaeger, K., Robrade, J., & Schmitt, J. H. M. M. 2010, A&A, 515, A98+

Porquet, D., Mewe, R., Dubau, J., Raassen, A. J. J., & Kaastra, J. S. 2001, A&A, 376, 1113

Preibisch, T., Neuhaeuser, R., & Alcala, J. M. 1995, A&A, 304, L13+

Preusse, S., Kopp, A., Büchner, J., & Motschmann, U. 2006, A&A, 460, 317

Priest, E. R. 1982, Solar magnetohydrodynamics, 74P–+

Reale, F., Betta, R., Peres, G., Serio, S., & McTiernan, J. 1997, A&A, 325, 782

Saar, S. H. & Baliunas, S. L. 1992, in Astronomical Society of the Pacific Conference Series, Vol. 27, The Solar Cycle, ed. K. L. Harvey, 150–167

Saar, S. H., Cuntz, M., Kashyap, V. L., & Hall, J. C. 2008, in IAU Symposium, Vol. 249, IAU Symposium, ed. Y.-S. Sun, S. Ferraz-Mello, & J.-L. Zhou, 79–81

Saffe, C., Gómez, M., & Chavero, C. 2005, A&A, 443, 609

Salter, D. M., Kóspál, Á., Getman, K. V., et al. 2010, A&A, 521, A32+

Scharf, C. A. 2010, ApJ, 722, 1547

Schmitt, J. H. M. M. 1997, A&A, 318, 215

Schmitt, J. H. M. M. 2009, in American Institute of Physics Conference Series, Vol. 1094, American Institute of Physics Conference Series, ed. E. Stempels, 473–476

Schmitt, J. H. M. M., Fleming, T. A., & Giampapa, M. S. 1995, ApJ, 450, 392

Schmitt, J. H. M. M., Ness, J., & Franco, G. 2003, A&A, 412, 849

Schwabe, M. 1844, Astronomische Nachrichten, 21, 233

Serio, S., Reale, F., Jakimiec, J., Sylwester, B., & Sylwester, J. 1991, A&A, 241, 197

Shkolnik, E., Bohlender, D. A., Walker, G. A. H., & Collier Cameron, A. 2008, ApJ, 676, 628

Shkolnik, E., Walker, G. A. H., Bohlender, D. A., Gu, P., & Kürster, M. 2005, ApJ, 622, 1075

Siarkowski, M., Pres, P., Drake, S. A., White, N. E., & Singh, K. P. 1996, ApJ, 473, 470

Snodgrass, H. B. 1984, Sol. Phys., 94, 13

Spörer, F. W. G. 1865, Astronomische Nachrichten, 63, 71

Strassmeier, K. G. 2002, Astronomische Nachrichten, 323, 309

Temple, R. K. G. 1988, The UNESCO Courier: a window open on the world, 41, 9

Thomas, R. N. 1957, ApJ, 125, 260

Thomson 'Lord Kelvin', W. 1862, Macmillan's Magazine, 5, 388

Tsuboi, Y., Koyama, K., Murakami, H., et al. 1998, ApJ, 503, 894

van den Oord, G. H. J. & Mewe, R. 1989, A&A, 213, 245

Vidal-Madjar, A., Lecavelier des Etangs, A., Désert, J., et al. 2003, Nature, 422, 143

Vogt, S. S., Penrod, G. D., & Hatzes, A. P. 1987, ApJ, 321, 496

Weisskopf, M. C., Tananbaum, H. D., Van Speybroeck, L. P., & O'Dell, S. L. 2000, in Society of Photo-Optical Instrumentation Engineers (SPIE) Conference Series, Vol. 4012, Society of Photo-Optical Instrumentation Engineers (SPIE) Conference Series, ed. J. E. Truemper & B. Aschenbach, 2–16

Wild, W. J. 1989, PASP, 101, 844

Wild, W. J. 1991, ApJ, 368, 622

Wolf, R. 1856, Astronomische Nachrichten, 44, 173

Wolter, U., Schmitt, J. H. M. M., Huber, K. F., et al. 2009, A&A, 504, 561

Wright, J. T. 2004, AJ, 128, 1273